

HZDR-055

**DEVELOPMENT AND CHARACTERIZATION
OF A TUNABLE ULTRAFAST X-RAY SOURCE
VIA INVERSE-COMPTON-SCATTERING**

Axel Jochmann

Wissenschaftlich-Technische Berichte
HZDR-055 · ISSN 2191-8708

**WISSENSCHAFTLICH-
TECHNISCHE BERICHTE**

hZDR



**HELMHOLTZ
ZENTRUM DRESDEN
ROSSENDORF**

Wissenschaftlich-Technische Berichte
HZDR-055

Axel Jochmann

**DEVELOPMENT AND CHARACTERIZATION OF A
TUNABLE ULTRAFAST X-RAY SOURCE
VIA INVERSE-COMPTON-SCATTERING**

hzdr

 **HELMHOLTZ
ZENTRUM DRESDEN
ROSSENDORF**

Druckausgabe: ISSN 2191-8708

Elektronische Ausgabe: ISSN 2191-8716

Die elektronische Ausgabe erscheint unter Creative Commons License (CC BY-NC-ND):

Qucosa: <http://fzd.gucosa.de/startseite/>

Die vorliegende Arbeit wurde sowohl als Dissertation an der Fakultät Mathematik und Naturwissenschaften der Technischen Universität Dresden, sowie als Wissenschaftlich-Technischer Bericht des Helmholtz-Zentrum Dresden – Rossendorf mit der Berichtsnummer **HZDR-055** veröffentlicht.

2014

Herausgegeben vom

Helmholtz-Zentrum Dresden - Rossendorf

Bautzner Landstr. 400

01328 Dresden

Germany



DEVELOPMENT AND CHARACTERIZATION OF A TUNABLE ULTRAFAST X-RAY SOURCE VIA INVERSE-COMPTON-SCATTERING

Axel Jochmann

Born on: 11th August 1981 in Reichenbach/Vogtland

DISSERTATION

to achieve the academic degree

DOCTOR RERUM NATURALIUM (DR. RER. NAT.)

First referee

Prof. Dr. Dr. h.c. Roland Sauerbrey

Second referee

Prof. Dr. Todd Ditmire

Supervising professor

Prof. Dr. Ulrich Schramm

Submitted on: 24th June 2014

Defended on: 24th September 2014



*This work is dedicated to my son Julian, his wonderful mother
and my entire family.*

*"It doesn't matter how beautiful your theory is,
it doesn't matter how smart you are. If it doesn't
agree with experiment, it's wrong."*

Richard P. Feynman

ABSTRACT

Ultrashort, nearly monochromatic hard X-ray pulses enrich the understanding of the dynamics and function of matter, e.g., the motion of atomic structures associated with ultrafast phase transitions, structural dynamics and (bio)chemical reactions. Inverse Compton backscattering of intense laser pulses from relativistic electrons not only allows for the generation of bright X-ray pulses which can be used in a pump-probe experiment, but also for the investigation of the electron beam dynamics at the interaction point.

The focus of this PhD work lies on the detailed understanding of the kinematics during the interaction of the relativistic electron bunch and the laser pulse in order to quantify the influence of various experiment parameters on the emitted X-ray radiation.

The experiment was conducted at the ELBE center for high power radiation sources using the ELBE superconducting linear accelerator and the DRACO Ti:sapphire laser system. The combination of both these state-of-the-art apparatuses guaranteed the control and stability of the interacting beam parameters throughout the measurement. The emitted X-ray spectra were detected with a pixelated detector of 1024 by 256 elements (each $26\mu\text{m}$ by $26\mu\text{m}$) to achieve an unprecedented spatial and energy resolution for a full characterization of the emitted spectrum to reveal parameter influences and correlations of both interacting beams. In this work the influence of the electron beam energy, electron beam emittance, the laser bandwidth and the energy-angle-correlation on the spectra of the backscattered X-rays is quantified.

A rigorous statistical analysis comparing experimental data to ab-initio 3D simulations enabled, e.g., the extraction of the angular distribution of electrons with 1.5% accuracy and, in total, provides predictive capability for the future high brightness hard X-ray source PHOENIX (Photon electron collider for Narrow bandwidth Intense X-rays) and potential all optical gamma-ray sources.

The results will serve as a milestone and starting point for the scaling of the X-ray flux based on available interaction parameters of an ultrashort bright X-ray source at the ELBE center for high power radiation sources. The knowledge of the spatial and spectral distribution of photons from an inverse Compton scattering source is essential in designing future experiments as well as for tailoring the X-ray spectral properties to an experimental need.

ZUSAMMENFASSUNG

Ultrakurze, quasi-monochromatische harte Röntgenpulse erweitern das Verständnis für die dynamischen Prozesse und funktionalen Zusammenhänge in Materie, beispielsweise die Dynamik in atomaren Strukturen bei ultraschnellen Phasenübergängen, Gitterbewegungen und (bio)chemischen Reaktionen. Compton-Rückstreuung erlaubt die Erzeugung der für ein pump-probe-Experiment benötigten intensiven Röntgenpulse und ermöglicht gleichzeitig einen Einblick in die komplexen kinematischen Prozesse während der Wechselwirkung von Elektronen und Photonen.

Ziel dieser Arbeit ist, ein quantitatives Verständnis der verschiedenen experimentellen Einflüsse auf die emittierte Röntgenstrahlung bei der Streuung von Laserphotonen an relativistischen Elektronen zu entwickeln.

Die Experimente wurden am ELBE - Zentrum für Hochleistungs-Strahlenquellen des Helmholtz-Zentrums Dresden - Rossendorf durchgeführt. Der verwendete supraleitende Linearbeschleuniger ELBE und der auf Titan-Saphir basierende Hochleistungslaser DRACO garantieren ein Höchstmaß an Kontrolle und Stabilität der experimentellen Bedingungen. Zur Messung der emittierten Röntgenstrahlung wurde ein Siliziumdetektor mit 1024x256 Pixeln (Pixelgröße $26\mu\text{m} \times 26\mu\text{m}$) verwendet, welcher für eine bisher nicht erreichte spektrale und räumliche Auflösung sorgt. Die so erfolgte vollständige Charakterisierung der Energie-Winkel-Beziehung erlaubt Rückschlüsse auf Parametereinflüsse und Korrelationen von Elektronen- und Laserstrahl.

Eine umfassende statistische Analyse, bei der ab-initio 3D Simulationen mit den experimentellen Daten verglichen und ausgewertet wurden, ermöglichte u.a. die Bestimmung der Elektronenstrahldivergenz mit einer Genauigkeit von 1.5% und erlaubt Vorhersagen zur zu erwartenden Strahlung der zukünftigen brillianten Röntgenquelle PHOENIX (Photon electron collider for Narrow bandwidth Intense X-rays) und potentiellen lasergetriebenen Gammastrahlungsquellen.

Die Ergebnisse dienen als Fixpunkt für die Skalierung des erwarteten Photonenflusses der Röntgenquelle für die verfügbaren Ausgangsgrößen am Helmholtz-Zentrum Dresden - Rossendorf. Das Wissen um die räumliche und spektrale Verteilung der Röntgenstrahlung ist entscheidend für die Planung zukünftiger Experimente sowie zur Anpassung der Quelle an experimentelle Bedürfnisse.

CONTENTS

Abstract	ix
1 Motivation	1
2 Basic theory and simulations of Inverse Compton Scattering (ICS)	7
2.1 Kinematics of ICS	8
2.1.1 The correlation between observation angle and photon energy	8
2.1.2 Temporal-spatial emission characteristics	10
2.1.3 Flux and bandwidth of ICS X-ray sources	12
2.2 CLARA - a numerical tool to model the ICS interaction	15
3 PHOENIX - experimental setup	19
3.1 The ELBE linear accelerator	20
3.1.1 General facility overview	20
3.1.2 Electron injectors	21
3.1.3 Electron beam diagnostics and parameters	23
3.2 The DRACO 150 TW Ti:Sapphire laser system	28
3.2.1 System parameters and overview	28
3.2.2 Transfer beamline and vacuum system	30
3.3 PHOENIX target area	31
3.3.1 Target chamber	31
3.3.2 Electron beam focusing setup	34
3.3.3 Laser beam focusing setup	37
4 PHOENIX commissioning experiments	43
4.1 Characterization of the timing and synchronization setup	44
4.2 Characterization of the X-ray diagnostic setup	48
4.3 Characterization and suppression of the X-ray background signal	52
4.4 First light and γ -dependence of the X-ray spectrum	54
5 High resolution X-ray spectroscopy on an ICS source	59
5.1 Photon flux distribution	61
5.2 Measurement of the Angle-Energy Correlation (AEC)	63
5.3 Dependence of the AEC on the Electron Beam Energy	66
5.4 Dependence of the AEC on the Laser Spectrum	68
5.5 Dependence of the AEC on the Electron Beam Angular Spread	71

6 Conclusion and Outlook	77
Appendix	83
A.1 Analytic scaling of the photon mean energy deviation on axis	83
A.2 Derivation of the Poisson Likelihood χ^2	85
Bibliography	87
Publications by the Author	99
Acknowledgments	101

1 MOTIVATION

Present availability of ultrashort ($\lesssim 1$ ps) hard (> 1 keV) X-ray pulses [1, 2] from X-ray free electron lasers (XFELs) has opened a new frontier in understanding the dynamics and function of matter. Examples include the motion of atomic structures associated with ultrafast phase transitions [3], structural dynamics [4] and (bio)chemical reactions [5, 6]. In addition there are sets of experiments that require single-shot capabilities associated with the necessary drivers to create matter at extreme states such as destructive processes in high energy density physics (HEDP) [7, 8], high pressure physics [9] and ultra high intensity laser matter interactions [10]. The high-power ultra-intense lasers driving these processes either deliver pulses below 1 ps with powers above 100 TW or longer pulses (< 10 ns) with highly energetic pulses containing more than 100 J depending on the specific experiment. Each of these lasers is a large machine with its own separate research field [11–14].

For some of the above mentioned experiments the full spectroscopic or structural data-set has to be obtained in a single exposure. The required combination of an X-ray FEL and a high power ultra-intense laser will be limited to a few sites worldwide, e.g. MEC@LCLS (USA), HERMES@SACLA (JAP) and the future HiBEF@XFEL (GER) because they require a gigaelectronvolt-accelerator and a several hundred meter long undulator structure.

A long term vision is to replace the conventional magnetic undulator device by an electro-magnetic wave in the optical spectral range. This will reduce the required electron energy necessary for a given X-ray photon energy and will lead to more compact X-ray sources with smaller accelerators, e.g. ELBE at the Helmholtz-Center Dresden - Rossendorf.

A first step in that direction is an inverse Compton scattering (ICS) source which was developed within the scope of this PhD work using the DRACO laser at ELBE. In inverse Compton scattering [15] the pulsed laser field can be interpreted as an optical undulator with spatially and temporally varying field strength. The undulating electrons emit Doppler-upshifted radiation into a relativistically contracted solid angle cone in the laboratory frame. A scheme of the interaction process is illustrated in Fig. 1.1. Since the undulator period is the laser wavelength, this method benefits from much lower required electron energies to produce a given X-ray energy, as compared to conventional magnetic undulator devices. If the energy of the emitted photon $\hbar\omega \ll m_e c_0^2$, such that no electron recoil is relevant, as is the case in this work, then the mechanism is also referred to as Thomson backscattering. An ultimate optical undulator, which has not yet been realized, requires a more complicated description including coherence effects and multi-photon interactions, which is beyond the scope of this work.

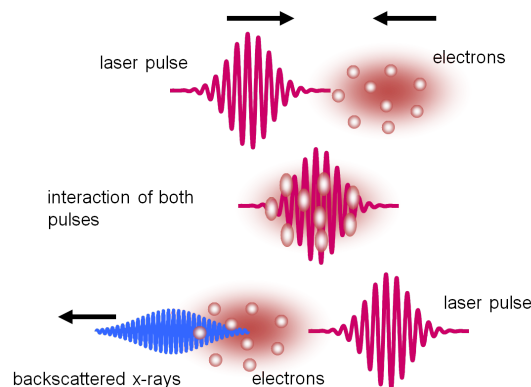


Figure 1.1: Schematic illustration of the interaction of an electron bunch with a laser pulse to produce ultra-bright X-ray radiation.

As a historical note, inverse Compton scattering was postulated as an energy degradation mechanism of interstellar high-energy electrons by Feenberg et al. (1948) [16]. In 1963 R. Milburn proposed an X-ray light source based on the scattering of an intense laser off a GeV electron beam [17]. Since then the mechanism has been extensively studied theoretically [18–24] and several backscattering sources have been built or are under development around the world. They can be distinguished according to their purpose as a probing light source [25–31] or as a diagnostic tool for the electron beam [32–34].

An ICS source will not have the extreme brightness of an X-ray free electron laser, however the parameters of an ICS source can be tuned to be suitable for certain types of experiments. With even modest electron beam energies these sources can be scaled to very high photon energies which exceed the operation range of synchrotron and XFEL light sources. In combination with their ultra-short nature ICS sources are the brightest light sources in that spectral region as illustrated in Fig. 1.2.

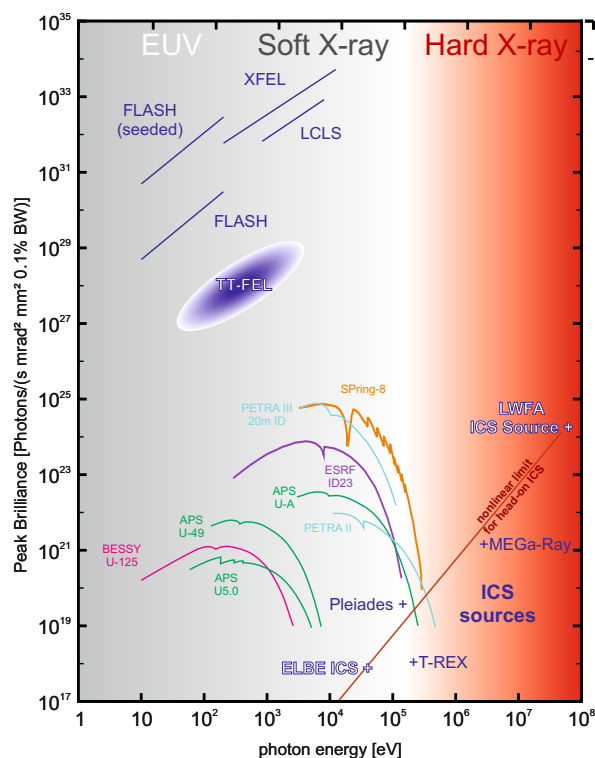


Figure 1.2: Comparison of the peak brilliance of various X-ray sources as a function of X-ray photon energy.

With photon energies of several kiloelectronvolts, a few percent relative bandwidth ($\Delta\omega/\omega$) and a photon flux above 10^6 photons per second delivered by an ICS source, one can overcome the detection threshold in HEDP experiments, set by the plasma self emission. Potential experiments are, for instance, X-ray absorption spectroscopy (XAS) which includes both Extended X-Ray Absorption Fine Structure (EXAFS) and X-ray Absorption Near Edge Structure (XANES) to measure the X-ray absorption coefficient of a material as a function of energy, or X-ray diffraction experiments such as Laue diffraction and Bragg diffraction. With the ELBE linear accelerator as the driver, X-ray pulses with a few picosecond duration can be produced defining the temporal resolution in these pump-probe experiments.

Furthermore there is a growing interest in strong field physics to study the fundamental process of the interaction between strong laser fields and relativistic elec-

trons. In this highly nonlinear regime various fundamental processes are predicted; e.g., multi-photon absorption [35], pair creations [36] and vacuum birefringence [37].

The DRACO 150 TW Ti:Sapphire Laser at the ELBE Center for High Power Radiation Sources can create relativistic laser intensities above 10^{20} W/cm² and therefore is ideally suited to explore the strong field regime as well as to drive samples to extreme conditions in HEDP pump-probe experiments. In addition, it can deliver femtosecond relativistic electrons via a process called laser wakefield acceleration in order to create an all-optical laser-driven ICS X-ray source.

Within this framework the ICS X-ray source PHOENIX is developed at the Helmholtz-Center Dresden - Rossendorf utilizing the unique combination of multiple petawatt class laser beams and a high brightness electron beam. PHOENIX is an acronym for "Photon electron collider for narrow bandwidth intense X-rays". It uses the DRACO laser together with the ELBE linear accelerator. This superconducting machine offers great stability and precise control of the electron bunch parameters which is of great importance to study the fundamental kinematics during the interaction of the electron bunch with the laser pulse.

The focus of this PhD work lies on the detailed understanding of the interaction in the linear regime. Nevertheless the PHOENIX design parameters allow for experiments with laser intensities well above the threshold for nonlinear scattering. In previous experiments the spectral characteristics of inverse Compton scattering were deduced from indirect filter-pack measurements [26, 30, 38, 39] or with single element semiconductor detection systems [25, 32, 33, 40]. Both methods suffer from limited detector resolution and low signal-to-noise ratio. In this work the influence of the electron beam energy, electron beam emittance, the laser bandwidth and the energy-angle-correlation on the spectra of the backscattered X-rays is quantified. The spectra were collected by a pixelated detector (CCD camera) at various observation angles and analyzed by a single photon counting technique [41, 42]. A full characterization of the emitted spectrum was performed to reveal correlations of both interacting beams. Hence, the measured data was compared to ab-initio calculations from the 3D radiation code CLARA. To our knowledge this is the first complete spectral characterization of an inverse Compton scattering source with high angular and high energy resolution. The knowledge of the spatial and spectral distribution of photons from an inverse Compton scattering source is essential in designing future experiments as well as for tailoring the X-ray spectral properties to an experimental need.

Furthermore PHOENIX will serve as a testbed for future pump-probe experiments on X-ray free electron lasers which are housed in large scale user facilities with limited access and beam time. The source will enable pilot experiments and will help to mature new time-resolved detection techniques and the general technology necessary for the interaction of a particle accelerator with a petawatt laser. For an experiment as sketched in Fig. 1.3, this technology involves the control of spatial overlap, temporal synchronization, suppression of radiation background, radiation hard detectors and many other aspects. PHOENIX will help to prepare for future XFEL experiments and will also be important in educating and training students and scientists in the field of laser-matter-interaction.

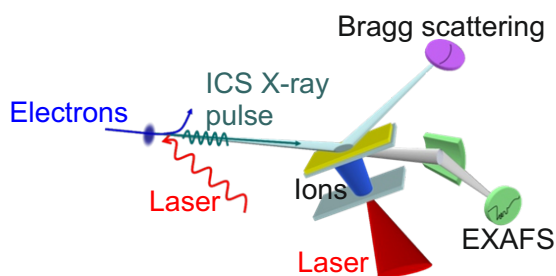


Figure 1.3: Schematic setup for a pilot pump-probe experiment where a proton beam heats a sample which is probed by a broadband X-ray pulse from an ICS source.

THESIS OUTLINE

This work which involved the design, construction, commission and characterization of the PHOENIX X-ray source is arranged as follows:

In Chapter 2 analytic expressions are derived to describe the basic kinematics of the electron–photon interaction. This includes the spatial emission characteristics, the resulting X-ray pulse duration as well as the angle dependent spectral flux. The chapter ends with a short description of the numerical framework used in the further analysis of the measured data.

The experimental setup of PHOENIX is described in Chapter 3. At first a brief overview of the linear accelerator ELBE and the terawatt laser DRACO is given. This includes the electron sources, the electron bunch and the laser pulse parameters and the transfer beamline to connect both facilities. Subsequently the interaction target area is described.

The first experiments during the commissioning of the source as well as the characterization of the required diagnostic tools is explained in Chapter 4.

Chapter 5 contains the description of the complete spectral characterization of a Thomson source with unprecedented angular and energy resolution. A rigorous statistical analysis comparing experimental data to 3D simulations enabled, e.g., the extraction of the angular distribution of electrons and, in total, provides predictive capability for future high brightness hard X-ray and gamma-ray sources.

The thesis closes with an outlook for the near and intermediate future with the emphasis on how the built source can be scaled up to higher photon fluxes and how it can be used in an X-ray absorption pump-probe experiment. Furthermore the next steps towards the nonlinear ICS interaction are pointed out and preliminary data is shown. Finally first wakefield acceleration results are presented which is a small step in order to build an all-optical ICS X-ray.

2 BASIC THEORY AND SIMULATIONS OF INVERSE COMPTON SCATTERING (ICS)

In this chapter a brief description of the interaction of a relativistic electron beam with a high intensity laser pulse is given. In the scenario of linear Inverse Compton scattering all electrons in the bunch act as single emitters with random phase. The bunch length of the electrons is much longer than the X-ray wavelength. For this reason the total emitted radiation is temporally incoherent and is the result of the summation of all single emitters. The interaction can be described as a scattering process using the particle picture for the laser photons, or by using a classical electro-magnetic description, where the laser electric field is treated as an optical undulator. Both pictures have been extensively used in the literature [15, 17, 19, 20, 43–52] and either yields a complete description of the interaction in the linear, incoherent regime of Thomson scattering. The particle picture is very convenient to derive the backscattered photon energy, the source directivity and the pulse duration using the four-vector framework. This picture is used in Subsection 2.1.1 and 2.1.2. The broadening effects on the X-ray bandwidth are more intuitive using the classical wave picture as seen in Subsection 2.1.3. The chapter is closed by the description of CLARA, a numerical code which was used as a versatile tool to model the interaction for a predictive analysis of the experimental data.

2.1 KINEMATICS OF ICS

2.1.1 THE CORRELATION BETWEEN OBSERVATION ANGLE AND PHOTON ENERGY

The collision of a laser photon, represented by the wave-vector \mathbf{k} and an electron with momentum \mathbf{p} is illustrated in Fig. 2.1. The interaction is described in the laboratory rest frame. The angles α and φ , respectively, define the collision angle between photon and electron. A detector, positioned at angle θ , would register the backscattered photon with the wave-vector \mathbf{k}_γ . After the interaction, the momentum of the incoming electron has changed to \mathbf{p}_s .

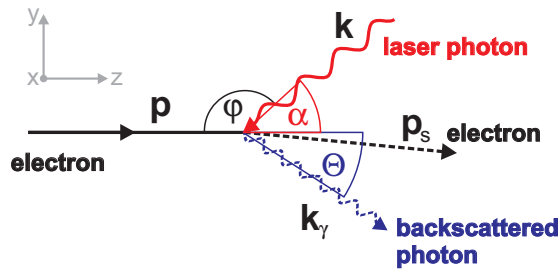


Figure 2.1: Schematic illustration of the interaction geometry of a laser photon with a relativistic electron in the laboratory frame.

The related four-vector for the electron is $p^\nu = (E/c, \mathbf{p})$ and for the laser photon k^ν .

$$\begin{aligned} p^\nu &= (\gamma mc, \gamma\beta_x mc, \gamma\beta_y mc, \gamma\beta_z mc) \\ k^\nu &= E/c (1, \mathbf{k}/|k|) \end{aligned} \quad (2.1)$$

In both cases E is the total energy of the particle/photon, m the electron rest mass and c is the vacuum speed of light. The Lorentz factor γ and the velocity β in units of c are related by $\gamma = 1/\sqrt{1 - \beta^2}$.

Conservation of the total four vector is assured by conservation of energy and mo-

momentum before and after scattering.

$$\begin{aligned} p + k &= p_s + k_\gamma \\ |p_s|^2 &= |p + k - k_\gamma|^2 \\ p_s^2 &= p^2 + k^2 + k_\gamma^2 + 2p \cdot (k - k_\gamma) - 2k \cdot k_\gamma \end{aligned} \quad (2.2)$$

Using the energy-momentum relation $|p|^2 = \frac{E^2}{c^2} - p^2 = m^2 c^2$ with the invariant electron mass and identifying the photons as a massless particle ($k^2 = k_\gamma^2 = 0$) Eq. 2.2 becomes:

$$0 = 2p \cdot (k - k_\gamma) - 2kk_\gamma \quad (2.3)$$

With the angles defined in Fig. 2.1 the vector components in Eq. 2.3 are

$$0 = \begin{pmatrix} \gamma mc \\ 0 \\ 0 \\ \gamma \beta mc \end{pmatrix} \cdot \frac{1}{c} \begin{pmatrix} E_0 - E_\gamma \\ 0 \\ -(E_0 \sin \alpha - E_\gamma \sin \theta) \\ -(E_0 \cos \alpha + E_\gamma \cos \theta) \end{pmatrix} - \begin{pmatrix} E_0/c \\ 0 \\ -\frac{E_0}{c} \sin \alpha \\ -\frac{E_0}{c} \cos \alpha \end{pmatrix} \cdot \begin{pmatrix} E_\gamma/c \\ 0 \\ \frac{E_\gamma}{c} \sin \theta \\ -\frac{E_\gamma}{c} \cos \theta \end{pmatrix}$$

and from there follows directly

$$E_\gamma = \frac{\gamma mc^2 E_0 (1 + \beta \cos \alpha)}{\gamma mc^2 - \gamma \beta mc^2 \cos \theta + E_0 (1 + \cos(\alpha + \theta))}. \quad (2.4)$$

Here E_0 is the laser photon energy and E_γ the energy of the scattered photon. Following the commonly used convention for the interaction angle, $\alpha = 180 - \varphi$, within the approximation of the Thomson-limit, where the electron experiences no recoil, $E_0/(mc^2) \ll 1$, Eq. 2.4 simplifies to:

$$E_\gamma = \frac{(1 - \beta \cos \varphi)}{(1 - \beta \cos \theta)} E_0. \quad (2.5)$$

The Lorentz boost from the electron rest frame to the laboratory frame bundles the emission to a near axis cone. If only small observation angles θ are considered and using $1 - \beta \approx 1/2\gamma^2$ (2.5) can be written as

$$E_\gamma = \frac{2\gamma^2 (1 - \beta \cos \varphi)}{1 + \beta(\gamma\theta)^2} E_0. \quad (2.6)$$

Taking a total beam energy $pc = 23$ MeV and a laser wavelength of $\lambda_0 = 800$ nm for head-on collision $\varphi = 180^\circ$, the maximum photon energy is 12.5 keV and rapidly decreasing with θ . A plot of Eq. 2.6 for these conditions is shown in Fig. 2.2.

The periodic electro-magnetic field of the laser causes a transverse motion of the electron. For high fields, the average axial velocity β_z will be effectively reduced because of the non-negligible trajectories away from the propagation axis, resulting in a lower Lorentz boost of the counter-propagating laser wavelength. The strength of this effect and the consequent red-shift of the scattered radiation can be accounted for by introducing the laser strength parameter a_0 .

$$a_0 = \frac{eE\lambda_{\text{laser}}}{2\pi mc^2} \quad (2.7)$$

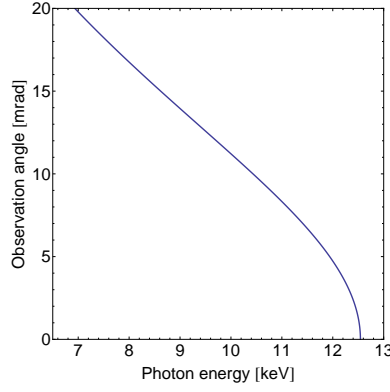


Figure 2.2: Angular dependence of scattered photon energy for the interaction of a single electron (kinetic energy 22.5 MeV) with a laser ($\lambda = 800$ nm) in head-on geometry.

This is analogous to the undulator parameter K for periodic magnetic structures.

$$K = \frac{eB\lambda_{\text{undulator}}}{2\pi mc} \quad (2.8)$$

E is the magnitude of the laser's electric field, B the undulator's magnetic field magnitude and e and m the charge, respectively mass of the electron. In practical units a_0 can also be expressed as

$$a_0 = 0.85 \frac{\lambda_{\text{laser}}}{[\mu\text{m}]} \sqrt{\frac{I_L}{[10^{18} \text{ W/cm}^2]}} \quad (2.9)$$

where I_L is the laser intensity.

Using the similarities between the periodic external fields for the motion of the electron in a classical undulator setup, and a laser field and following the derivations in [53] and [54], one can find an expression for the average longitudinal momentum.

$$\gamma^* = \frac{\gamma}{\sqrt{1 + \frac{a_0^2}{2}}} \quad (2.10)$$

Replacing γ in (2.6) with γ^* from (2.10) directly leads to

$$E_\gamma = \frac{2\gamma^2(1 - \beta \cos \varphi)}{1 + \frac{a_0^2}{2} + \beta(\gamma\theta)^2} E_0. \quad (2.11)$$

If the values of a_0 approach unity or greater, the trajectory of the electron is not sinusoidal anymore. This gives rise to higher harmonics in the backscattered radiation which can be taken account by introducing a factor n , representing the corresponding harmonic.

$$E_\gamma = n \cdot \frac{2\gamma^2(1 - \beta \cos \varphi)}{1 + \frac{a_0^2}{2} + \beta(\gamma\theta)^2} E_0. \quad (2.12)$$

2.1.2 TEMPORAL-SPATIAL EMISSION CHARACTERISTICS

The emission cone angle is calculated by a transformation from the electron rest frame to the laboratory frame. Primed quantities represent the electron rest frame,

unprimed quantities are related to the laboratory frame. The coordinate system is identical with the one from Fig. 2.1. The interaction angle is $\varphi = 180^\circ$.

For the extreme case of a photon emitted parallel to the y-axis of the rest frame coordinate system (minima of the dipole emission), the photon has a momentum four vector

$$p_Y^\mu = \left(\frac{E'}{c}, 0, \frac{E'}{c}, 0 \right). \quad (2.13)$$

Applying the boost matrix for a Lorentz transformation from the electron rest frame to the laboratory frame [47] in the direction of the rest frame z-axis leads to

$$p_{\text{lab}} = \begin{pmatrix} \gamma & 0 & 0 & \beta\gamma \\ 0 & 1 & 0 & 0 \\ 0 & 0 & 1 & 0 \\ \beta\gamma & 0 & 0 & \gamma \end{pmatrix} \begin{pmatrix} E'/c \\ 0 \\ E'/c \\ 0 \end{pmatrix} = \begin{pmatrix} \gamma E'/c \\ 0 \\ E'/c \\ \gamma\beta E'/c \end{pmatrix}. \quad (2.14)$$

The emission angle for light emitted from highly relativistic electrons follows directly

$$\tan \theta = \frac{p_y}{p_z} = \frac{E'/c}{\gamma\beta E'/c} \approx \frac{1}{\gamma} \quad (2.15)$$

An inverse Compton scattering source is directed with an opening angle of $\pm 1/\gamma$.

The X-ray pulse duration is determined by the time during which the relativistic electron bunch interacts with the electric field of the laser pulse. The interaction is described for a head-on interaction using a Minkowski diagram. The electron bunch moves in the positive z-direction, the laser pulse is counter propagates. The interaction starts at $(z, ct) = (0, 0)$. The interaction stops at a time t_1 . An observer at position $z = 0$ measures an X-ray duration τ_x . This time τ_x is the sum of the interaction time, t_1 , and the time, t_2 , that an X-ray photon needs to travel from the point of last overlap to the observer. The interaction time t_1 is defined by the penetration of both pulses with lengths L_{bunch} and L_{laser} at the closing speed $v + c$ (seen by an observer in the laboratory frame).

$$\begin{aligned} c \cdot t_1 &= c \cdot \frac{L_{\text{bunch}} + L_{\text{laser}}}{v_{\text{relative}}} \\ c \cdot t_1 &= c \cdot \frac{\beta c \tau_b + c \tau_{\text{laser}}}{c(1 + \beta)} \end{aligned} \quad (2.16)$$

The length ct_2 corresponds to the distance from the tail of the electron bunch to the observer at $x = 0$ after the time t_1 .

$$c \cdot t_2 = L_b - v_b t_1 = \beta c \tau_b - \beta c \left(\frac{\beta \tau_b + \tau_{\text{laser}}}{1 + \beta} \right) \quad (2.17)$$

$$\begin{aligned} c \cdot \tau_x &= c \cdot t_1 + c \cdot t_2 \\ \tau_x &= \left(\frac{\beta \tau_b + \tau_{\text{laser}}}{1 + \beta} \right) (1 - \beta) + \beta \tau_b \\ \tau_x &= \underbrace{\beta \tau_b \left(\frac{1 - \beta}{1 + \beta} + 1 \right)}_{\approx \tau_b} + \underbrace{\tau_{\text{laser}} \frac{1 - \beta^2}{(1 + \beta)^2}}_{\approx \tau_{\text{laser}}/4\gamma^2} \end{aligned} \quad (2.18)$$

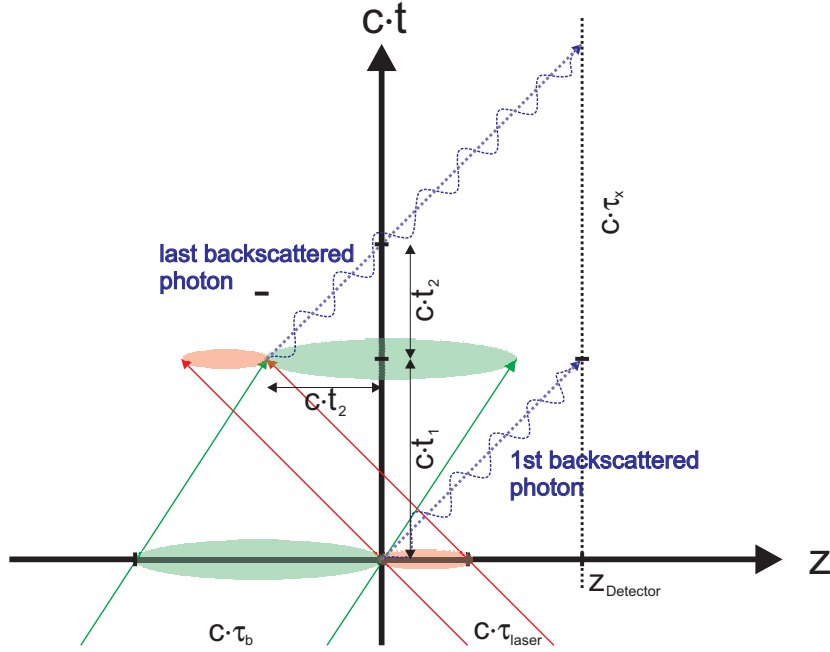


Figure 2.3: Minkowski diagram of the laboratory frame illustrating the interaction of a relativistic electron beam with a counter-propagating laser pulse to determine the pulse duration of the produced X-ray pulse.

For relativistic electron bunches, the laser pulse is Lorentz contracted and therefore the X-ray pulse duration approximately equals the electron bunch duration.

2.1.3 FLUX AND BANDWIDTH OF ICS X-RAY SOURCES

Subsection 2.1.1 described the dependence of the scattered photon energy as a function of the interaction geometry, mainly the collision and observation angle. This treatment excluded effects such as finite interaction length or averaging effects. Originating from the finite bunch nature of the two interaction partners, these influences and their consequences must be considered in order to estimate photon numbers, as well as, the bandwidth of the radiation that could be detected.

The spectrum emitted from a single electron undergoing an undulating motion can be derived from the Liénard-Wiechert potentials. The far field solution for spectral intensity per solid angle $d\Omega$ is

$$\frac{d^2 I_{e^-}}{d\omega d\Omega} = \frac{e^2}{4\pi^2 c} \left| \int_{-\infty}^{+\infty} \frac{\mathbf{n} \times [(\mathbf{n} - \boldsymbol{\beta}) \times \dot{\boldsymbol{\beta}}]}{(1 - \boldsymbol{\beta} \cdot \mathbf{n})^2} e^{i\omega(t - \mathbf{n} \cdot \mathbf{r}(t)/c)} dt \right|^2 \quad (2.19)$$

which is valid as long as the detector distance is much greater than the source size, effectively reducing it to a point source [47]. The trajectory of the electron is $\mathbf{r}(t)$ from which the velocity $\boldsymbol{\beta}$ and acceleration $\dot{\boldsymbol{\beta}}$ can be calculated. The vector \mathbf{n} points towards the detector. The geometry is illustrated in Fig. 2.4.

The solution of Eq. 2.19 for an undulator, resulting in a sinusoidal motion $\mathbf{r}(t)$ with

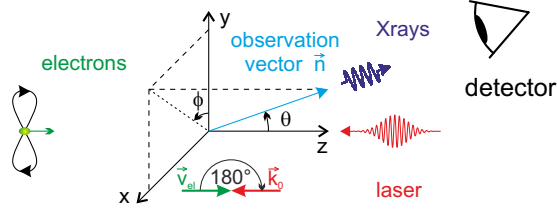


Figure 2.4: Thomson scattering geometry (Figure from [24]).

wavelength λ_0 and N_0 oscillations, is [19, 22]

$$\frac{d^2 I_{e^-}}{d\omega d\Omega} = \frac{e^2 \omega^2}{8\pi c^2} N_0 \lambda_0 a_0^2 \mathbb{G}(\omega), \quad (2.20)$$

$$\mathbb{G}(\omega) = \frac{N_0}{\bar{\omega}} \left[\frac{\sin(\pi(\omega - \bar{\omega})N_0/\bar{\omega})}{\pi(\omega - \bar{\omega})N_0/\bar{\omega}} \right]^2. \quad (2.21)$$

for a detector placed on the beam axis ($\theta = 0$, therefore: $\omega \simeq \bar{\omega} = 4\gamma^2\omega_0$). $\mathbb{G}(\omega)$ is the resonance function peaked at $4\gamma^2\omega_0$. $N_0\lambda_0$ represents the interaction length. The width of $\mathbb{G}(\omega)$ scales inversely with the number of oscillations N_0 and defines the natural linewidth $(\Delta\omega/\omega)_{N_0}$.

The total scattered X-ray spectrum can be calculated by convolving the single-electron spectrum with the distribution functions describing the laser and electron bunch parameters

$$\frac{d^2 I_{\text{total}}}{d\omega d\Omega} \propto \iiint \frac{d^2 I_{e^-}}{d\omega d\Omega} \cdot f(\gamma - \gamma^*) \cdot g(\varphi - \varphi^*) \cdot h(\omega_0 - \omega_0^*) \dots d\gamma^* d\varphi^* d\omega_0^* \quad (2.22)$$

where f , g and h are exemplary distribution functions for the electron beam energy spread, the beam divergence and the laser bandwidth. For example, a Gaussian distribution of the beam energy $\Delta\gamma$ results in:

$$f = \exp \left[-\frac{1}{2} \left(\frac{\gamma - \gamma^*}{\Delta\gamma} \right)^2 \right]. \quad (2.23)$$

The width of the distribution increases from the intrinsic natural linewidth, which was determined by the interaction length (undulator periods). Using error propagation methods, assuming Gaussian distributions and head-on collision, the total bandwidth at an observation angle $\theta = 0$ can be estimated from Eq. 2.22 [19, 26, 51, 55]

$$\frac{\Delta\omega}{\omega} \approx \sqrt{\left(\frac{\Delta\omega}{\omega}\right)_{N_0}^2 + \left(\frac{\Delta\omega}{\omega}\right)_{\gamma}^2 + \left(\frac{\Delta\omega}{\omega}\right)_{\lambda}^2 + \left(\frac{\Delta\omega}{\omega}\right)_{\epsilon}^2 + \left(\frac{\Delta\omega}{\omega}\right)_{\text{Det}}^2} \quad (2.24)$$

$$\frac{\Delta\omega}{\omega} \approx \sqrt{\left(\frac{1}{N}\right)^2 + \left(\frac{2\Delta\gamma}{\gamma}\right)^2 + \left(\frac{\Delta\omega_0}{\omega_0}\right)^2 + \left(\frac{\epsilon_N^2}{\sigma_r^2}\right)^2 + (\gamma^2 \Delta\Omega_{\text{Det}}^2)^2} \quad (2.25)$$

by taking into account the contributions of the intrinsic width, the beam energy spread, the laser bandwidth as well as the beam emittance and the broadening due to the finite detector size ($\sim \gamma^2 \Delta\Omega_{\text{Det}}^2$). The last four terms can be found by dividing Eq. 2.11 by \hbar and subsequently building the derivatives $d\omega/d\gamma$, $d\omega/d\omega_0$, $d^2\omega/d\varphi^2$ and $d^2\omega/d\theta^2$.

Using a superconducting linac ($\Delta\gamma/\gamma = 0.001$) and a 500 fs laser pulse (corresponding to $N_0 \sim 180$) together with the intended spatial resolution, the contributions $(\frac{\Delta\omega}{\omega})_{N_0}$, $(\frac{\Delta\omega}{\omega})_{\gamma}$ and $(\frac{\Delta\omega}{\omega})_{\text{Det}}$ in Eq. 2.24 are negligible.

For all cases $\theta \neq 0$ or $\varphi \neq 180^\circ$ the integral in Eq. 2.22 has to be solved to analyze the resulting spectral distribution. For a narrow-bandwidth laser and a perfect detection system ($QE = 1$) the integral for the X-ray photon density can be written as [33, 56]

$$\begin{aligned} \frac{dN_\gamma}{d\kappa d\theta_x d\theta_y} \propto & \int_0^\infty \int_0^{2\pi} d\gamma^* d\phi \left[1 - 4\kappa(1 - \kappa) \cos^2 \phi \right] \\ & \times \exp \left[\underbrace{-\frac{1}{2} \left(\frac{\gamma - \gamma^*}{\Delta\gamma} \right)^2}_f \right] \\ & \times \exp \left[\underbrace{-\frac{\left(\theta_x - \frac{1}{\gamma} \sqrt{\frac{1}{\kappa} - 1} \sin \phi \right)^2}{2\sigma_{\theta_x}^2}}_g \right] \times \exp \left[\underbrace{-\frac{\left(\theta_y - \frac{1}{\gamma} \sqrt{\frac{1}{\kappa} - 1} \cos \phi \right)^2}{2\sigma_{\theta_y}^2}}_g \right] \end{aligned} \quad (2.26)$$

with the azimuthal angle ϕ (see Fig. 2.4), the electron beam energy spread $\Delta\gamma$, the widths of the angular distribution for the vertical (horizontal) direction σ_{θ_x} (σ_{θ_y}) and the normalized X-ray photon energy $\kappa = (\hbar\omega)/(4\gamma^2 \hbar\omega_0) = 1/(1 + \gamma^2\theta^2)$. Equation 2.26 assumes a single laser frequency of a linearly y-polarized laser with a Gaussian angular distribution of the electron beam.

With $\Delta\gamma \rightarrow 0$ and $\sigma_{\theta_x} = \sigma_{\theta_y} = \sigma_\theta$, Eq. 2.26 can be integrated, with the result [57]:

$$\frac{dN_\gamma}{d\kappa d\theta_x d\theta_y} = \frac{N_b N_{\text{phot}} \sigma_T}{2\pi\epsilon^2} \exp \left[-\frac{(1/\kappa - 1)}{2\gamma^2 \sigma_\theta^2} - \frac{\theta_x^2 + \theta_y^2}{2\sigma_\theta^2} \right] \left[1 - 4\kappa(1 - \kappa) \left(\frac{3}{2} I_0[y] + I_2[y] \right) \right] \quad (2.27)$$

where

$$y = \frac{\sqrt{(\theta_x^2 + \theta_y^2)(1/\kappa - 1)}}{\gamma\sigma_\theta^2} \quad (2.28)$$

with the electron beam emittance ϵ , the classical Thomson cross-section σ_T and the number of photons and electrons N_{phot} respectively N_b . I_0 and I_2 are modified Bessel functions of the first kind.

An illustration of a solution from Eq. 2.27 for the interaction of an electron beam at $\gamma = 45$ and emittance $\epsilon = 1\pi$ mm mrad with a Ti:Sapphire laser in head-on geometry is shown in Fig. 2.5. In addition to the angle-energy-curve in Fig. 2.2, the plot shows the increasing bandwidth of the emitted radiation for increasing observation angles, as well as the concentration of the photon flux within a cone ($1/\gamma \approx 22$ mrad) around the electron beam propagation direction.

If a detector position and size is defined, the number of photons can be obtained by integrating over the spectral density. The total photon yield into the full solid angle can be written in practical units following further simplifications by Esarey et al. [19, 24] for a given bandwidth $\frac{\Delta\omega}{\omega}$:

$$N_{\text{phot}} = 8.4 \times 10^{19} \cdot \frac{N_0 \lambda_0^2}{2\pi d^2} \cdot Q[C] \cdot P_{\text{Laser}}[\text{TW}] \cdot \left(\frac{\Delta\omega}{\omega} \right) \quad (2.29)$$

In Eq. 2.29 Q is the electron bunch charge, N_0 represents the number of oscillation

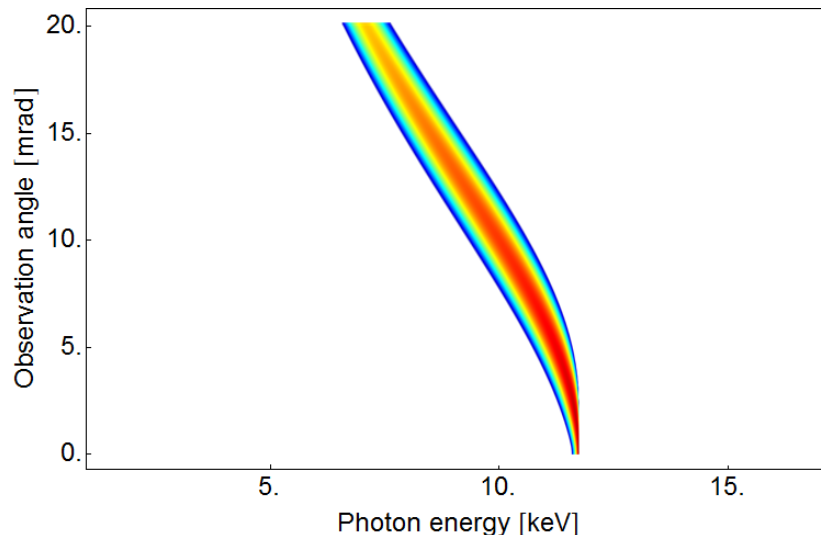


Figure 2.5: Normalized logarithmic colormap of the spectral intensity for an electron beam at $\gamma = 45$ and emittance $\varepsilon = 1\pi$ mm mrad with a Ti:Sapphire laser in head-on geometry.

periods during the interaction and d is the beam diameter for both beams.

Despite the good predictions that have been made using Eq. 2.27 [33, 56], it is important to mention the limitations. Most importantly, this approach only considers incoherent scattering in the linear regime. For our current setup this is sufficient, but with advanced techniques [58, 59] the interaction lengths can be dramatically increased, which ultimately might lead to feedback on the electron bunch and laser-like emission. Although the laser bandwidth can be included e.g. by a Gaussian distribution function, the model cannot represent laser pulses with a time-varying instantaneous frequency or time-varying intensity. Previous publications describe the possibility of chirping a laser pulse to influence the bandwidth of the emitted radiation [60, 61]. In the conducted experiment, it has to be considered that the laser pulse was chirped to control the laser intensity during the interaction. Furthermore, space-charge effects and ponderomotive forces are not included but can influence the X-ray bandwidth due to an increased transverse momentum of the electrons. Finally, the entire focusing geometry of both beams is not taken into account and requires a more rigorous method to reveal the full nature of the interaction in an inverse Compton scattering source.

2.2 CLARA - A NUMERICAL TOOL TO MODEL THE ICS INTERACTION

Analytical equations for the key parameters of a light source are important as a starting point when designing pump-probe experiments. For demanding scenarios at the edge of feasibility, more sophisticated tools are necessary. Numerical codes that are able to include all the relevant physical effects in 3D are the most favorable method. For an inverse Compton scattering source it is naturally important that the model describing the laser pulse is very accurate. This includes the spatio-temporal photon distribution as well as total flux and also the laser beam propagation and focusing geometry. All of these together define the intensity of the laser during the interaction, ultimately distinguishing between the linear or nonlinear regime. Additionally, the

electron beam transverse and longitudinal emittance, the electron energy spread and the laser spectral shape have to be fully included.

Monte-Carlo algorithms are often employed to model the interaction [46, 50–52]. The electron bunch and the laser pulse are sampled one electron and one photon at a time. Each electron is described by its momentum, position and direction, while each photon is described by its position, direction and wavelength. Based on Eq. 2.11, every collision is treated in the framework of the interaction of a single electron with a single photon. The incoherent summation of all individual events yields the total X-ray spectrum. Even more accurate results can be obtained by taking into account space charge effects or the ponderomotive force of the laser and X-ray emission into higher orders. Especially in the transition range of $a_0 \rightarrow 1$, the approach of calculating the angular spectral flux density based on solving the Liénard-Wiechert potentials is the method of choice. In contrast to summing scattering probabilities over the electron and photon phase-space using standard Monte-Carlo techniques, this approach takes into account the phase of the emitted radiation to include coherence effects. This technique can also be extended into the free electron laser regime and shall be briefly described here.

The “**CL**assical **RA**diation Calculator” (CLARA) code was developed by A. Debus et al [24, 62] to quantitatively predict and analyze the scattering process. In the Thomson-limit, $\hbar\omega \ll \gamma m_e c^2$, without any recoil effects, classical electrodynamics are valid. Hence, one can calculate the radiation spectra from an electron trajectory by solving the Liénard-Wiechert potentials in the far field.

For the consideration of more than one electron, one has to perform a summation inside the norm in Eq. 2.19 for all electrons. This way the phase between the radiated waves from different electrons is taken into account. Introducing the polarization filter vector \mathbf{P} , Eq. 2.19 becomes

$$\frac{d^2 I}{d\omega d\Omega} = \frac{e^2}{4\pi^2 c} \left| \mathbf{P} \cdot \sum_j \int_{-\infty}^{+\infty} \frac{\mathbf{n} \times [(\mathbf{n} - \boldsymbol{\beta}_j) \times \dot{\boldsymbol{\beta}}_j]}{(1 - \boldsymbol{\beta}_j \cdot \mathbf{n})^2} e^{i\omega(t - \mathbf{n} \cdot \mathbf{r}_j(t)/c)} dt \right|^2 \quad (2.30)$$

$\mathbf{P} = (0, 1, 0)$ corresponds to a polarizer in the y -direction.

The interaction of an electron bunch with the laser is modeled by the commercial particle tracking code *GPT* (General Particle Tracer) [63]. In this case, the laser field is treated as a time-dependent external field by specifying analytic expressions in paraxial approximation. The *GPT* output trajectories serve as input for CLARA.

Figure 2.6(a)-(e) show numerical results of angular resolved spectral distributions for various scenarios. The “ideal” scenario consists of a laser pulse which has a rectangular temporal profile with a flat intensity distribution and wavefront interacting with a laminar electron beam ($\epsilon_N = 0$). The “Gauss” model is identical except the laser temporal shape is Gaussian, leading to a time-dependent intensity. The “real” model uses parameters available at the ELBE/DRACO facility including the full propagation model for both beams, defining spatio-temporal overlap as well as ponderomotive or space-charge effects. In more detail this model assumes a 250 fs electron bunch with $\gamma = 25$ and electron beam emittances of $\epsilon_{n,\text{trans}} = 2.5\pi$ mm mrad and $\epsilon_{n,\text{long}} = 40\pi$ keV ps. The laser strength parameter was varied from $a_0 = 0.1$ to $a_0 = 1.5$ to distinguish between the linear and nonlinear inverse Compton scattering regimes.

In the linear regime, the differences among the three models are very subtle. The substructures from the ideal case are washed out in the real scenario. The flux is more concentrated on the electron beam propagation axis in the latter case, as seen in Fig. 2.6(a) and (b).

Figure 2.6(c)-(e) illustrate the results in the nonlinear regime. The high-intensity

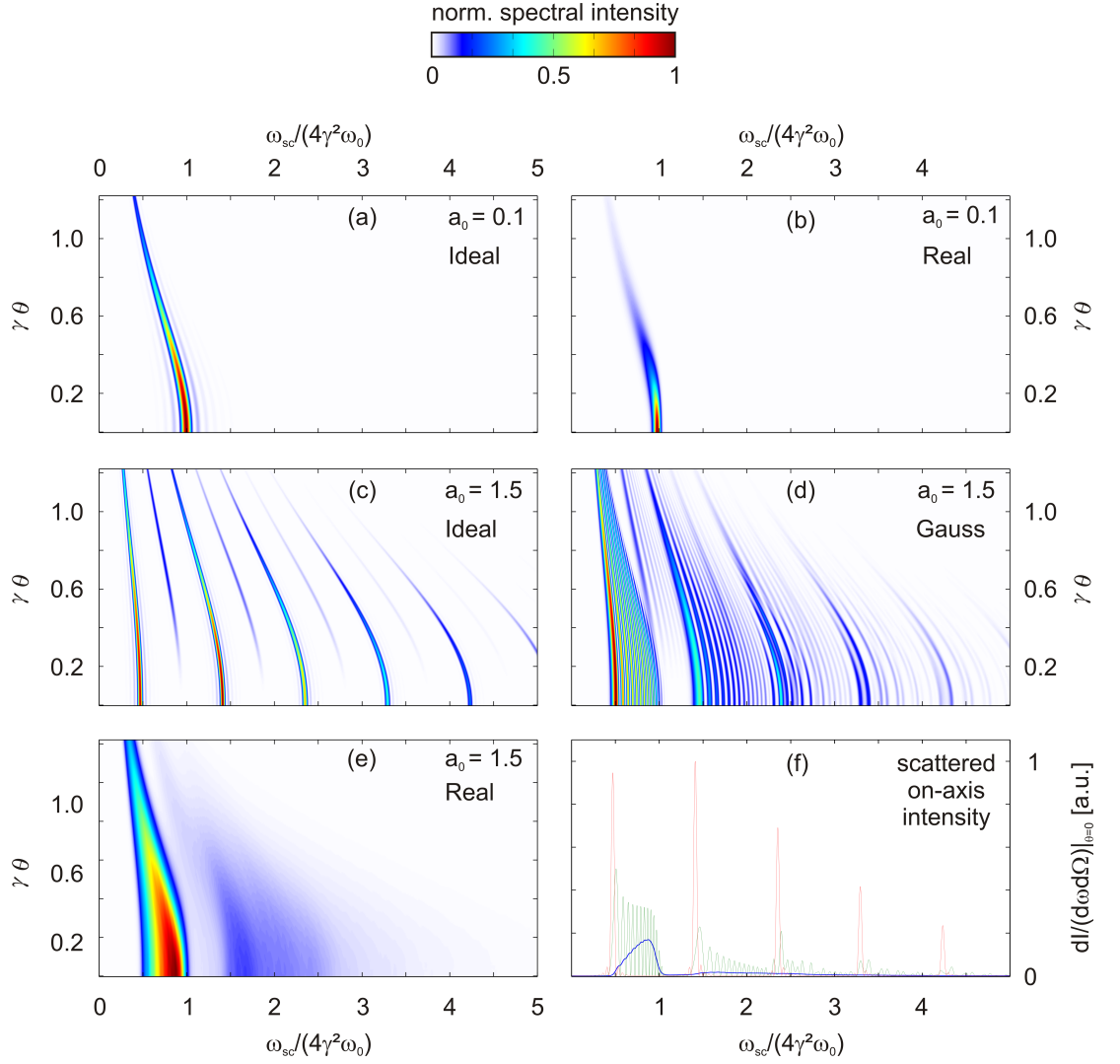


Figure 2.6: (a)-(e) show numerical results of angular resolved spectral distributions for various scenarios. The “ideal” scenario consists of a laser pulse which has a rectangular temporal profile with a flat intensity distribution and wavefront interacting with a laminar electron beam ($\epsilon_N = 0$). The “Gauss” model is identical except the laser temporal shape is Gaussian, leading to a time-dependent intensity. The “real” model uses parameters available at the ELBE/Draco facility including the full propagation model for both beams, defining spatio-temporal overlap as well as ponderomotive or space-charge effects. In more detail this model assumes a 250 fs electron bunch with $\gamma = 25$ and electron beam emittances of $\epsilon_{n,trans} = 2.5\pi$ mm mrad and $\epsilon_{n,long} = 40\pi$ keV ps at a laser strength of $a_0 = 1.5$ or $a_0 = 0.1$. (f) shows intensity profiles at $\theta = 0$ for all models (Figure from [24]).

temporal flat-top laser pulse creates a number of harmonics with the odd ones also radiating on axis. The fundamental peak is red-shifted to about $\omega_{\text{sc}}/(4\gamma_0^2 \cdot \omega_0) = 0.5$. The spectrum change in the Gaussian case is a consequence of the time-dependent laser strength a_0 . At the temporal peak of the Gaussian pulse, the redshift is similar to the ideal case, prior to this peak and afterwards the redshift is reduced and changes in every oscillation of the laser field. This creates substructures reaching from $\omega_{\text{sc}}/(4\gamma_0^2 \cdot \omega_0) = 0.5$ to $\omega_{\text{sc}}/(4\gamma_0^2 \cdot \omega_0) = 1$, corresponding to a_0 from maximum to zero. Owing to the extended substructures, the harmonics overlap. In a realistic simulation the substructures are almost completely washed out by non-ideal effects, such as transverse Gaussian intensity distribution of the focus. The overall spectrum is the superposition of the radiation from electrons interacting at various laser intensities because of their collision point in space and time. Hence, the spectral oscillations from the laser are averaged out, resulting in a broadened spectrum. Other, less pronounced non-ideal effects arise from the divergence and the ponderomotive potential. The experimental setup conditions to study the kinematics in the linear regime with a laser strength parameter $a_0 = 0.05$ are similar to the case illustrated in Fig. 2.6(b).

3 PHOENIX - EXPERIMENTAL SETUP

The laser-electron backscattering experiment was conducted in a dedicated target area that was designed and commissioned as a part of the PhD work. To guide both beams to the experimental cave, two beamlines were built. The laser beamline was actively stabilized to compensate thermal drifts and vibrations which would affect the pointing stability. The repetition rate of the laser required the installation of single-shot pulse-picking controls and diagnostics for the linear accelerator. In the following, the sources for both interacting beams will be briefly described. Thereafter a description of the PHOENIX target area will be given.

3.1 THE ELBE LINEAR ACCELERATOR

3.1.1 GENERAL FACILITY OVERVIEW

The ELBE accelerator (Electron Linac with high Brilliance and low Emittance) is a quasi-cw superconducting electron linear accelerator. It utilizes the technology of superconducting accelerator cavities for high repetition rates up to $f_{\text{rep}} = 13$ MHz and serves as a driver for the generation of secondary radiation via various schemes. Figure 3.1 shows a footprint of the ELBE-facility including the experimental caves for the free electron laser FELBE, bremsstrahlung generation γ ELBE, neutrons nELBE and (single-)electron beams. In the center of the picture is the Inverse Compton scattering cave that is shared with the positron source pELBE.

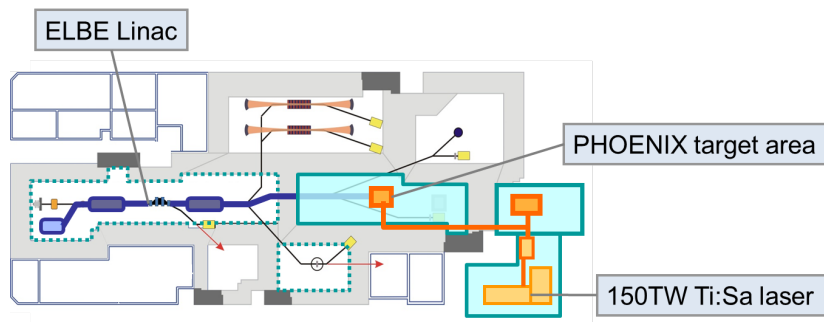


Figure 3.1: Footprint of the ELBE - Center for High-Power Radiation Sources during the campaign in 2011 highlighting the linear accelerator, the laser laboratories and the PHOENIX experimental cave.

Essentially the linac can be divided into two parts, the electron injector and a two-stage superconducting radio-frequency (RF) accelerator section. The accelerator part at ELBE consists of two modules with two superconducting cavities in each module. The 9-cell cavities (originally developed for the TESLA accelerator [64] at DESY, Hamburg) are built from niobium and are operated at a temperature of 1.8 K. An image of the first accelerator module at ELBE is shown in Fig. 3.2.



Figure 3.2: Photo of the first accelerator module at ELBE (Jürgen Lösel)

At the exit of the fourth cavity the electrons can reach energies up to 40 MeV. The RF amplifiers are operated in the linear regime which allows for tunability of the beam

energy. This tunability is directly translated into the energy range of the PHOENIX X-ray source.

A schematic illustration of the bunch propagation through the injector, the superconducting (sc) accelerator modules to the target area is given in Fig. 3.3. It includes the bunch parameters energy, energy spread and bunch duration for each section. Also shown is a simplified longitudinal phase-space plot which shows the growth in beam energy and the final pulse duration on target.

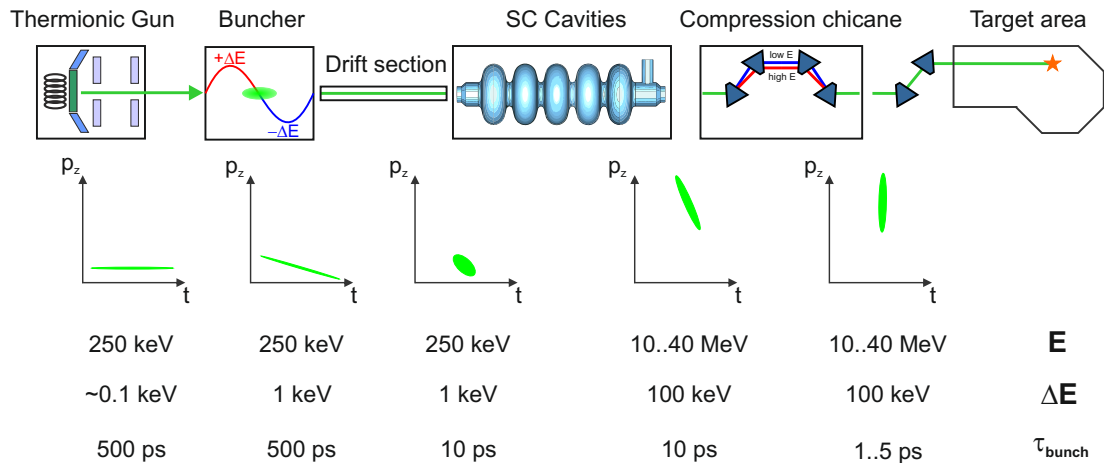


Figure 3.3: Schematic illustration of the bunch propagation through the injector, the superconducting (sc) accelerator modules to the target area.

The beam starts from the thermionic gun. It passes a buncher unit which modulates the beam energy. The propagation through a subsequent drift section leads to a compressed electron bunch at the entrance of the first accelerator module. The subsequent acceleration to highly relativistic energies increases the beam energy spread. This spread can be controlled by adjusting the phase of the accelerating field in the accelerator cavities. The energy spread is necessary to further compress the electron bunch. A magnetic chicane increases the electron path length for electrons with lower kinetic energy in comparison with higher energy electrons, which leads to electron bunches with a few picoseconds duration. A beamline connects the target area with the accelerator and compressor section. To suppress X-ray bremsstrahlung radiation at the detectors, this beamline features an achromatic double bend (dogleg).

3.1.2 ELECTRON INJECTORS

There are two independent injector setups at ELBE - a thermionic dc gun and a superconducting RF photo-gun. These guns are the source of the electrons and define the initial beam parameters.

At present the thermionic injector acts as the main driver for the accelerator. It was used throughout the first scattering experiments. The thermionic gun is a well-established and characterized source that is required for the operation of ELBE as a user facility.

Parallel to the operation of this gun, HZDR pursues the research and development of a superconducting radio-frequency gun. This type of injector has the potential to fulfill the needs of future light sources by producing high peak current, high average current and low emittance electron beams.

In this section a short overview of the used gun parameters shall be given, together with the parameters available in the near future.

Thermionic injector This injector consists of a thermionic triode and a buncher to compress the electron pulses before injecting them into the accelerator modules. Based on thermionic emission, electrons are emitted from a metal plate that is heated to about 1100 °C. A pulsed grid creates an electron pulse train that is accelerated to 250 keV with a static electric field before reaching the buncher. Because of the grid's duty cycle, the pulse length is about 500 picoseconds. The bunch charge depends on the grid voltage (see Fig. 3.4b) and can reach 77 pC before the space charge driven emittance growth cannot be tolerated anymore.

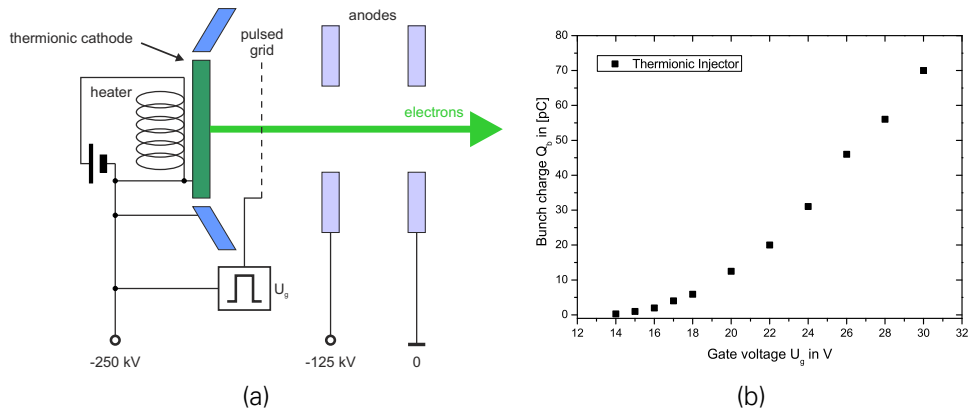


Figure 3.4: (a) Schematic illustration of the thermionic triode working principle. (b) Tuning curve of the micro-pulse bunch charge versus the gate voltage.

Before the final acceleration, the bunch needs to be compressed (see Fig. 3.3). The compression to sub-20 ps is necessary so that the entire bunch experiences nearly the same field amplitude in the main accelerator section. The compression is done with a high-frequency electro-magnetic standing wave inside two pillbox cavities, one operated at 260 MHz, another at 1.3 GHz. This results in electron pulses of about 10 picoseconds at the entrance of the first accelerator cavity. Both bunching units add an absolute energy spread of about 1 keV. The entire injector section from the cathode to the cavity entrance of the accelerator includes additional beamline elements to collimate and steer the beam.

SRF-Photogun The superconducting radio-frequency photo-gun is an electron source based on the photoelectric effect of a semi-conductor photo-cathode in a cryogenic environment. Laser pulses with 15 ps pulse duration and a pulse energy of 0.5 microjoules at $\lambda = 263$ nm from a frequency quadrupled Nd:YLF are directed onto the cathode which is sufficient for bunch charges up to $Q = 1$ nC. Currently, the available charge is limited to 200 pC because of beamline constraints of the test environment. The photon energy $h\nu$ is slightly bigger than the work function of the photo cathode, leading to the emission of electrons with a narrow initial kinetic energy distribution.

Beam properties like spot size and duration are transferred from the laser pulse to the electron bunch. Without prior compression, the bunch is accelerated in the superconducting $3\frac{1}{2}$ -cell cavity of the gun. Presently, the electric field gradients in the cavity are limited to about 5 MeV/m because of the onset of field emission [66]. The fast rise of the dark current signal, shown in Fig. 3.6, reduces the signal-to-noise ratio and limits the usability of this injector for low background experiments. The dark current onset is independent of the cathode bias voltage, which indicates little contribution of field emitted electrons from the cathode itself.

A fresh cavity is currently being tested that allows for gradients up to 35 MeV/m. This would increase the electron energy from 2.1 MeV to ultimately 10 MeV at the

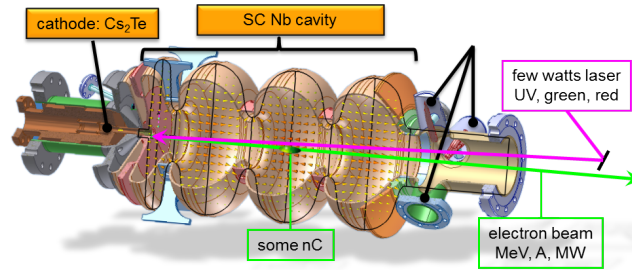


Figure 3.5: 3D technical drawing of the HZDR SRF-Gun with overlaying field distribution inside the cavity (courtesy by A. Arnold [65])

SRF-gun exit. The operation of the cavity at gradients well below the maximum values offers the possibility to significantly reduce the amount of unwanted dark current.

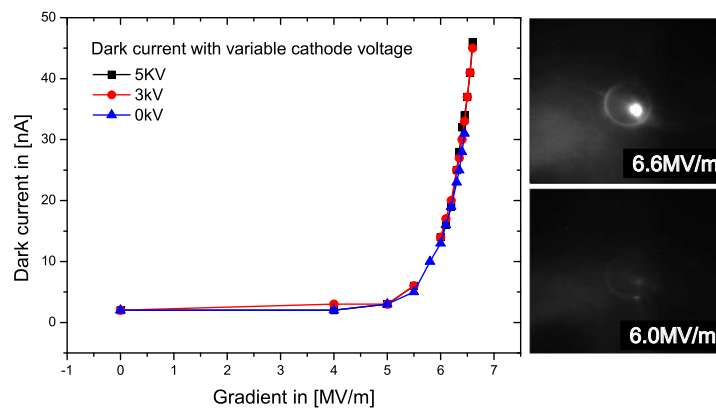


Figure 3.6: left: Dark current signal as a function of the field gradient in the cavity in the absence of a laser pulse. The dark current onset is independent of the cathode bias voltage (5 kV, 3 kV or 0 kV), Right: YAG Screen images for gradients of 6 MeV/m and 6.6 MeV/m. (Image from [66])

3.1.3 ELECTRON BEAM DIAGNOSTICS AND PARAMETERS

The output parameters of an inverse Compton scattering source are strongly coupled to the electron bunch parameters. Therefore, diagnostics are necessary to determine the bunch properties before the analysis of the interaction kinematics can occur. The main focus lies on the electron bunch duration, the transverse normalized emittance, the bunch charge and the beam energy.

Electron bunch duration From Eq. 2.18 it follows that for ultra-short laser pulses ($< \text{ps}$) the X-ray pulse length is about equal to the electron bunch duration. At ELBE it was measured by electro-optic sampling (EOS) [67, 68]. EOS is an indirect measurement of the electron bunch's electric field, from which the longitudinal charge distribution can be deduced.

The electric field of the electron bunch causes a birefringence in a special crystal (i.e. ZnTe) that can be probed with a femtosecond laser (Fig. 3.7). By varying the delay between laser and electron bunch, one can measure the charge distribution.

Using the scanning technique, electron pulse durations from the thermionic injector have been measured by C. Kaya et al [69, 70] as a function of the bunch charge. The pulse length was measured after the second accelerator cavity at an energy of

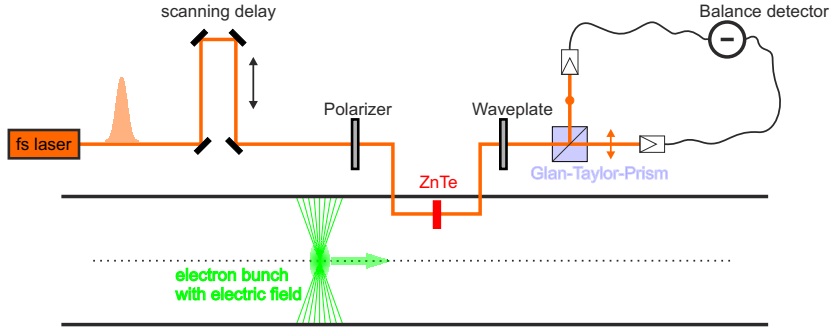


Figure 3.7: Principle of the electro-optic sampling method with temporal scanning technique including polarizer P and analyzer A. For higher sensitivity a Glan-Taylor prism in combination with a balance detector setup is used.

$p c = 23 \text{ MeV}$. The result is shown in Fig. 3.8. For the maximum bunch charge of

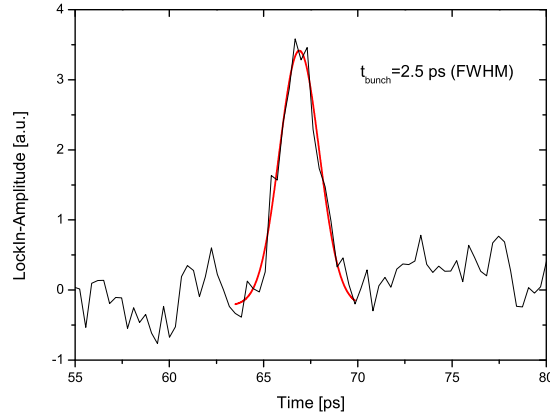


Figure 3.8: Exemplary measurement of the electron beam bunch duration [69, 70].

77 pC the FWHM bunch duration, measured with this technique, is 2.5 ps.

Electron beam normalized transverse emittance The emittance is defined as the area of the phase-space ellipse that contains a certain fraction of all electrons (e.g. 95%) divided by a factor π . It can be expressed by the Twiss parameters α, β, γ . An exemplary illustration of the phase-space ellipse for the $x - x'$ coordinates is shown in Fig. 3.9. Also shown are the relations of the Twiss parameters to the beam width and beam divergence.

For instance, the beam envelope function $\sigma_r(z)$ is related to β by

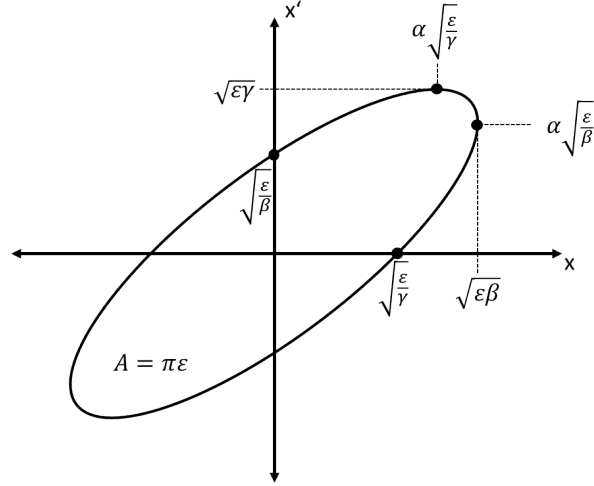
$$\sigma_r(z) = \sqrt{\beta(z)\epsilon} \quad (3.1)$$

with the geometric emittance $\epsilon = \sigma_r \sigma_\varphi$.

At the focus of the electron beam the beam width and divergence are related to each other via the beam normalized transverse emittance ϵ_N (for electron beams with $\Delta\gamma/\gamma < 0.005$)

$$\epsilon_N(\text{RMS}) = \beta\gamma\sigma_r\sigma_\varphi \quad (3.2)$$

where σ_r is the rms beam width and σ_φ stands for the rms beam angular spread. The normalized transverse emittance is independent of the beam energy, and the γ -dependence of the divergence is compensated compared to the geometric emittance.

Figure 3.9: Phase-space ellipse in the x - x' plane.

With Eq. 3.2, a value of the transverse emittance and a measured spot size, one can deduce the divergence of the electron beam. This divergence translates into various electron-photon collision angles during the scattering process, as shown later in Fig. 5.5 in Section 5.2. For this reason the emittance is the most sensitive parameter for the shape of the X-ray spectral distribution.

The value of the normalized transverse emittance was recently measured at the exit of the injector with 13π mm mrad. Transverse field gradients in the first accelerator cavity and chromatic aberrations in an energy dispersive beam transport section can increase the transverse emittance. To determine the emittance growth, an additional emittance monitor had been installed at the entry of the target chamber. The monitor consists of a set of quadrupole lenses at z_1 with tunable focal length f , a drift section of length $L = z_2 - z_1$ and a screen to determine the beam width σ_r .

Using the propagation matrix formalism of the Twiss parameters for the quadrupole lens - drift section combination, the beam width at position z_2 (screen) can be expressed by

$$\sigma_{r,2}^2 = \beta_2 \epsilon = \epsilon \left[\left(1 + \frac{L}{f}\right) \beta_1 - 2L \left(1 + \frac{L}{f}\right) \alpha_1 + L^2 \gamma_1 \right] \quad (3.3)$$

where the indices 1, 2 refers to the position z_1 or z_2 along the beam propagation axis.

Fitting Eq. 3.3 to the experimental data, a transverse normalized emittance of $\epsilon_N = (16 \pm 2)\pi$ mm mrad was deduced.

Electron beam energy and energy spread The X-ray photon energy scales quadratically with the Lorentz factor γ of the electrons. We therefore require precise knowledge of the electron energy to predict the backscattered photon energy. Measurement of the bending radii or deflection on a screen can be used to determine beam energy and energy spread. The beam position on the detector screen depends on the beam input angle and input position at the dipole entrance. For real beams with a finite size and divergence, the correlation between energy and screen position is not biunique. This problem can be overcome by using an imaging spectrometer in the Browne-Buechner geometry [71]. In this setup an entrance slit is imaged to an angled screen to maintain the energy-deflection-dependence.

Because of the remanence of the spectrometer magnets, which would influence

the beam, the Browne-Buechner-spectrometer cannot be used in transmission during the experimental campaign. Therefore one of the beamline dipoles had been calibrated to measure the beam energy depending on the beam deflection for a known B-field. The field was measured by a «Metrolab» PT2025 NMR-probe within the return yoke of the magnet. An experiment for the photodisintegration of deuterons [72], conducted in the γ ELBE-cave, indicated a systematic error in this procedure as shown in Fig. 3.10. The value of this energy offset for the PHOENIX cave is not known but is estimated to be within the same order of magnitude.

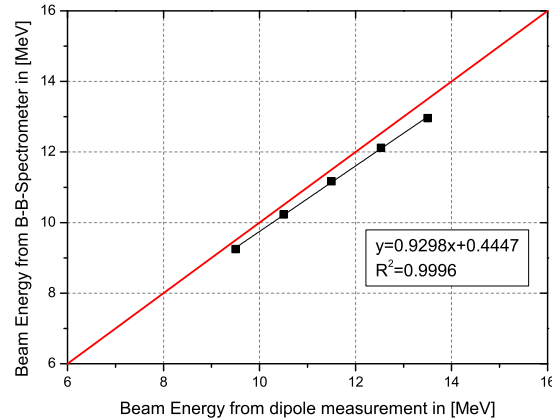


Figure 3.10: Calibrated dipole measurement in comparison to the results from the Browne-Buechner spectrometer.

The electron beam energy spread was determined from a spot size measurement in a dispersive beamline section after a dipole. Using the previously determined calibrations, an energy spread of $\Delta\gamma/\gamma = 0.1\%$ was measured (see Fig. 3.11).

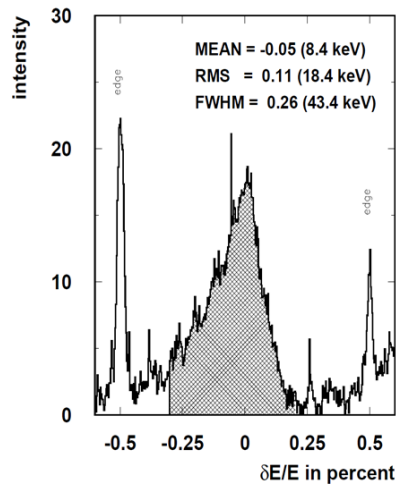


Figure 3.11: Viewscreen-lineout behind a dipole in the nuclear physics experimental cave to measure the electron beam energy spread.

Electron bunch charge The X-ray flux scales linearly with the electron bunch charge Q (see Eq. 2.29). Accurate knowledge of the interacting charge is important to enable scaling of current results for future facility parameters. At ELBE, the bunch charge was typically measured by dividing the beam-dump current signal by the pulse repetition rate. In a 10 Hz/single-shot regime, single-shot diagnostics had to be implemented since the charge of the leading pulse in a bunch train can differ significantly

from the average bunch charge. To monitor the bunch charge, resolving every bunch, an integrating current transformer (ICT) [73] was installed at the target chamber entrance. The ICT output signal width is constant 20ns , based on the internal RC circuit time constant. Using the calibrations for the signal amplifiers, together with cross-

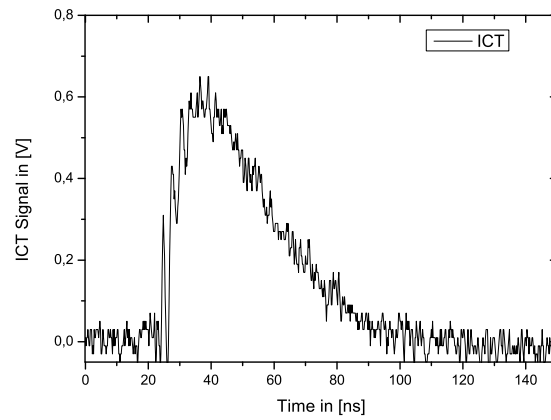


Figure 3.12: Exemplary ICT scope signal from Tektronix DPO4040

calibrations against a Faraday cup in the cw-operation [74], the bunch charge can be deduced from the current signal in Fig. 3.12. The maximum bunch charge from the thermionic injector was measured to be $Q = 77\text{ pC}$.

3.2 THE DRACO 150 TW TI:SAPPHIRE LASER SYSTEM

The DRACO high intensity laser is a CPA (chirped pulse amplification [75, 76]) laser system based on the commercially available *Pulsar* series by «Amplitude Technologies». It uses titanium sapphire as gain material, which ensures a broad gain bandwidth in the near infrared spectral region, supporting pulse durations of 30 fs and less.

3.2.1 SYSTEM PARAMETERS AND OVERVIEW

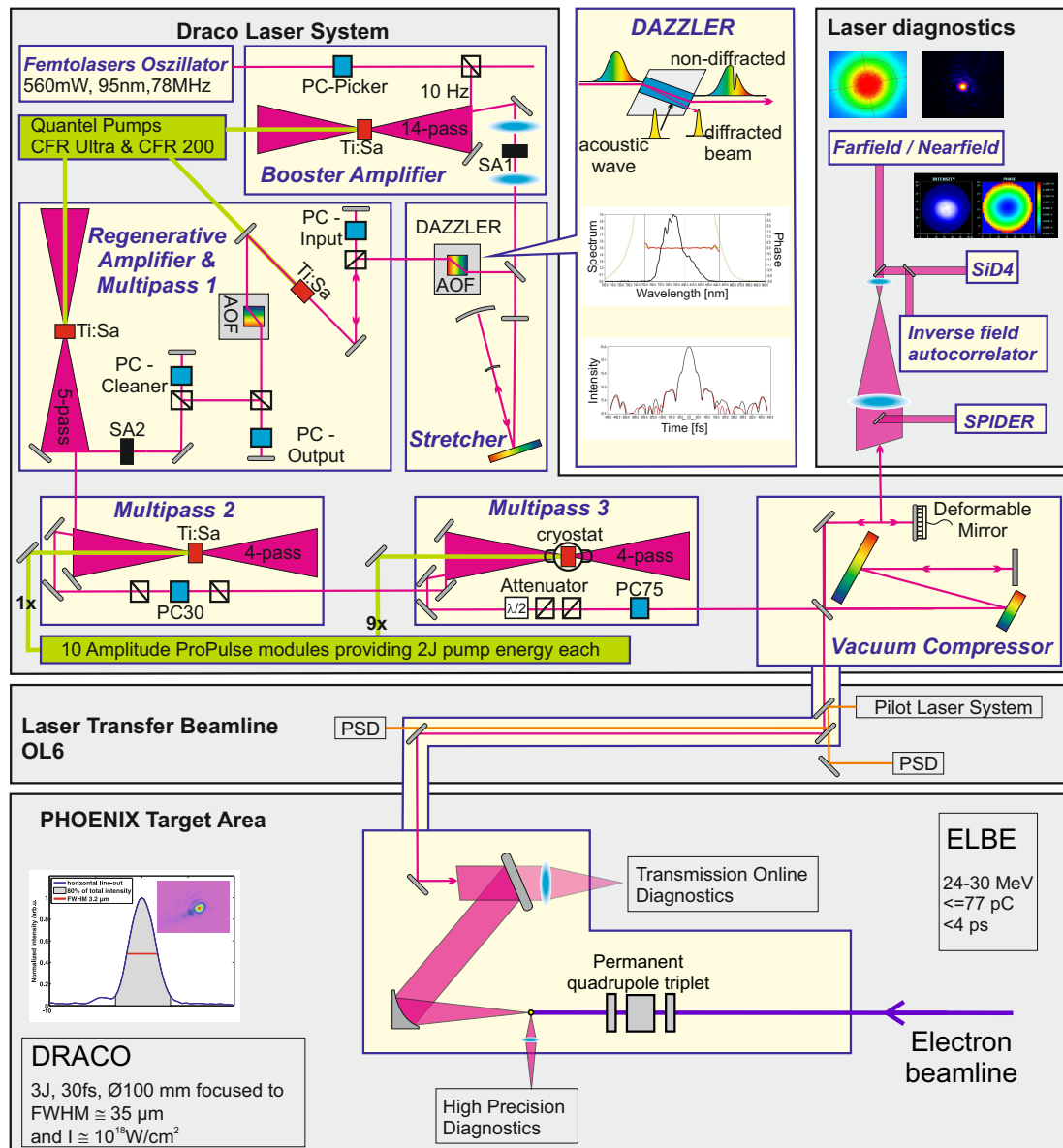


Figure 3.13: Pictogram of the DRACO laser system, the transfer beamline and the PHOENIX target area.

A schematic illustration of the total system is shown in Fig. 3.13. Employing the principle of chirped pulse amplification, a short laser pulse is temporally stretched, subsequently amplified and finally recompressed, with the aim of avoiding damage to the optical components employed during amplification. At HZDR, the laser chain starts with a «Femtolasers» oscillator which delivers 15 fs-pulses [77] centered at

800 nm wavelength at a repetition rate of 78 MHz, followed by a pulse picker, to reduce this repetition rate to 10 Hz. Before entering the stretcher, a booster amplifier increases the pulse energy from a few nanojoules to several microjoules for an increased signal-to-noise ratio after stretching. The all-reflective Öffner-stretcher [78] increases the pulse duration to about 500 ps. The pulse stretching unit also incorporates a «Fastlite» Dazzler to alter and fine-tune the spectral phase and amplitude in order to achieve optimal compression. The dazzler is a programmable device based on the longitudinal interaction of an acoustic wave with an optical pulse inside a birefringent crystal [79]. The device was also used during the measurement campaign to shape the pulse duration from the minimum duration of about 30 fs to 500 fs and back in order to vary the laser strength a_0 without manipulating the stretcher/compressor configuration. Following the stretching unit, the pulse is amplified by three orders of magnitude in a regenerative amplifier. A «Fastlite» Mazzler acousto-optic gain filter (AOF) inside the amplifier controls the laser pulse spectrum by reducing the transmission in the spectral region with the highest gain. This increases the wings in the laser spectrum relative to the center [80]. The bandwidth of the laser spectrum after the amplifier can be up to 80 nm.

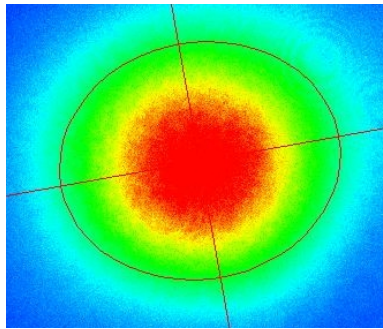


Figure 3.14: Nearfield image after the regenerative amplifier.

Additionally, the regenerative amplifier acts as a spatial filter producing a TEM_{00} mode (Fig. 3.14) that is subsequently amplified in three consecutive multipass amplifiers to a pulse energy of 5 – 7 Joules before entering the compressor unit. Between the amplifiers, polarizers combined with Pockels cells clean the beam from unwanted pre- and post-pulses. Telescopes increase the beam diameter after each amplifier to adapt to the increased pulse energy, thereby remaining below the damage threshold for each component. Multipass 1 and 2 (see Fig. 3.13) have a fixed gain defined by the available 532 nm pump power. The main amplifier is cryogenically cooled and pumped by 9 individual pump lasers, each delivering 2 Joules pump energy. Cryogenic cooling avoids thermal lensing in the amplifier crystal. For this reason, the laser wavefront is not influenced by the pump power in the main amplifier. Hence, the pulse energy can be varied by changing the number of active pump lasers.

The power of the laser after the main amplifier is about 10 GW. To achieve multi-terawatt peak power, temporal compression of the laser pulse after amplification is necessary. This can be achieved by a Treacy type grating setup [81] that provides anomalous dispersion. This compensates the optical path length differences of the spectral components, accumulated during the propagation through the stretcher unit and amplifiers. In the experiment pulse durations of 30 fs were measured.

The laser power of the compressed pulse exceeds the critical power in air by orders of magnitude. This would result in a beam profile dependent local change of the refractive index, which severely changes the beam profile [82, 83]. This effect is prevented by building a vacuum enclosure around the compressor, target areas and the

connecting beamlines. This also avoids dust-induced burn spots on the large optical components.

Relativistic intensities ($> 10^{18}$ W/cm²) at the focal plane of the laser depend on the focusability and therefore the wavefront of the laser pulse. A deformable mirror is set up after the compressor to offset wavefront errors accumulated during amplification and to pre-compensate wavefront distortions picked up in the beamline from the compressor to the target chamber.

3.2.2 TRANSFER BEAMLINE AND VACUUM SYSTEM

The interaction chamber is set up in an experimental cave adjacent to the clean-room that houses the high-intensity laser. Because of radiation safety constraints, the beamline is mounted on top of the laser and accelerator rooms, entering the experimental cave through the ceiling. This way the amount of necessary additional shielding is minimized and the accessibility to the beamline mirrors is maximized. The length of the entire beamline from the compressor output to the target chamber amounts to 50 m in different environments with and without temperature stabilization. In addition, vibrations from vacuum pumps, fans and other sources couple through the ceiling of the building into the beamline mounts and have to be taken into account. A real-time detection and control system was developed [84] to actively stabilize the beamline.

As described previously, the DRACO laser repetition rate is limited to a maximum of 10 Hz, which is too slow to be used as a pointing reference. Therefore we installed a tunable continuous wave diode laser (Sacher Mod. LYNX-S3-0730-020 [85]). The mirrors used to guide the high-intensity laser reflect laser light in the spectral range from 750 nm to 850 nm. Below or above that spectral region, the reflectivity drops rapidly. A precisely tuned laser can then be partially reflected and transmitted. A beam position detector behind each turning mirror delivers a feedback signal for the previous mirror actuators. A schematic of the beamline setup is shown in Fig. 3.15. The

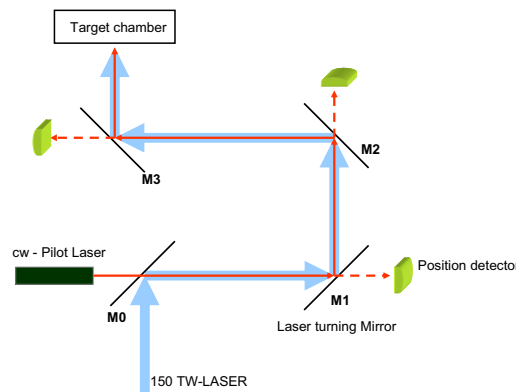


Figure 3.15: Schematic illustration of the pointing stabilization setup.

pilot laser beam's far field is imaged onto a «Hamamatsu» S2044 PSD-detector (position sensitive device). Consequently the measurement detects angular deviations, important to stabilize the interaction angle during the scattering experiment. Parallel shifts can not be detected, but their occurrence is very unlikely in the given setup. The deviations Δx and Δy from the setpoints for every mirror-detector pair are analyzed in a FPGA based real-time system (NI compactRIO). A PID control program steers a double-actuator pair for each axis on each mirror. The actuator pair consists of a slow

long travel range actuator to compensate thermal drifts and a fast piezo actuator to deal with the higher frequency vibrations.

The laser pulses contain up to 5 Joules of energy. The damage threshold of the dielectric turning mirrors in the femtosecond regime of $500 \text{ mJ}/\text{cm}^2$ demands 20 cm apertures. The necessary large optics mirror mounts limit the overall performance of the stabilization. For a quick reaction to the actuator movement, the mount's spring pre-load has to be very high. This force is limited by the actuator maximum load. The combination of mirror mount and actuator as a driven oscillator has a resonance frequency near 60 Hz (see Fig. 3.16) which defines the maximum stabilization frequency. The detection setup can operate at a refresh rate of up to several kilohertz but the stabilization operates up to 40 Hz.

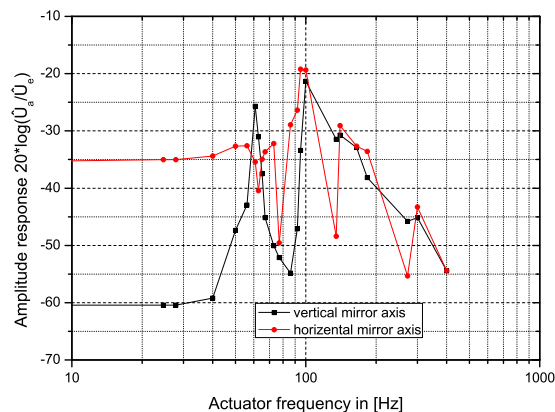


Figure 3.16: The response curve shows possible operation up to about 40 Hz actuator frequency.

The long-term performance of the stabilized beamline can be seen in Fig. 3.17. The figure shows the actuator voltage and the PSD-signal (with the Y-axis as exemplar). In order to maintain the set beam position, the actuator compensates a temperature-related linear drift and pointing jitter. After about 6400 s of measurement, the active stabilization is turned off. The magnified parts in Fig. 3.17 show that the beam position standard deviation grows by a factor of 5 in the unstabilized case. With the beamline stabilization in operation, the pointing jitter at the interaction plane was measured with the result of about $50 \mu\text{m}$ peak to peak, equivalent to one focal spot size or $16 \mu\text{rad}$.

3.3 PHOENIX TARGET AREA

Besides its primary purpose of housing the backscattering experiments, the target area was also designed for electron acceleration experiments via a laser driven wake-field inside a gaseous target [86, 87]. In this case, the accessible parameter space differs from the standard ELBE parameters, and Monte-Carlo simulations were required to ensure the fulfillment of radiation safety requirements. These studies conducted by M.Gross with the *FLUKA* code [88] led to the result depicted in Fig. 3.18, which shows that the existing radiation protection is sufficient for an assumed electron source with 1 GeV beam energy, a 1 nC bunch charge at a repetition rate of 10 Hz.

3.3.1 TARGET CHAMBER

A modified target chamber from the Strathclyde University collaboration partners was used. The modification was necessary to implement very long focal length parabolas,

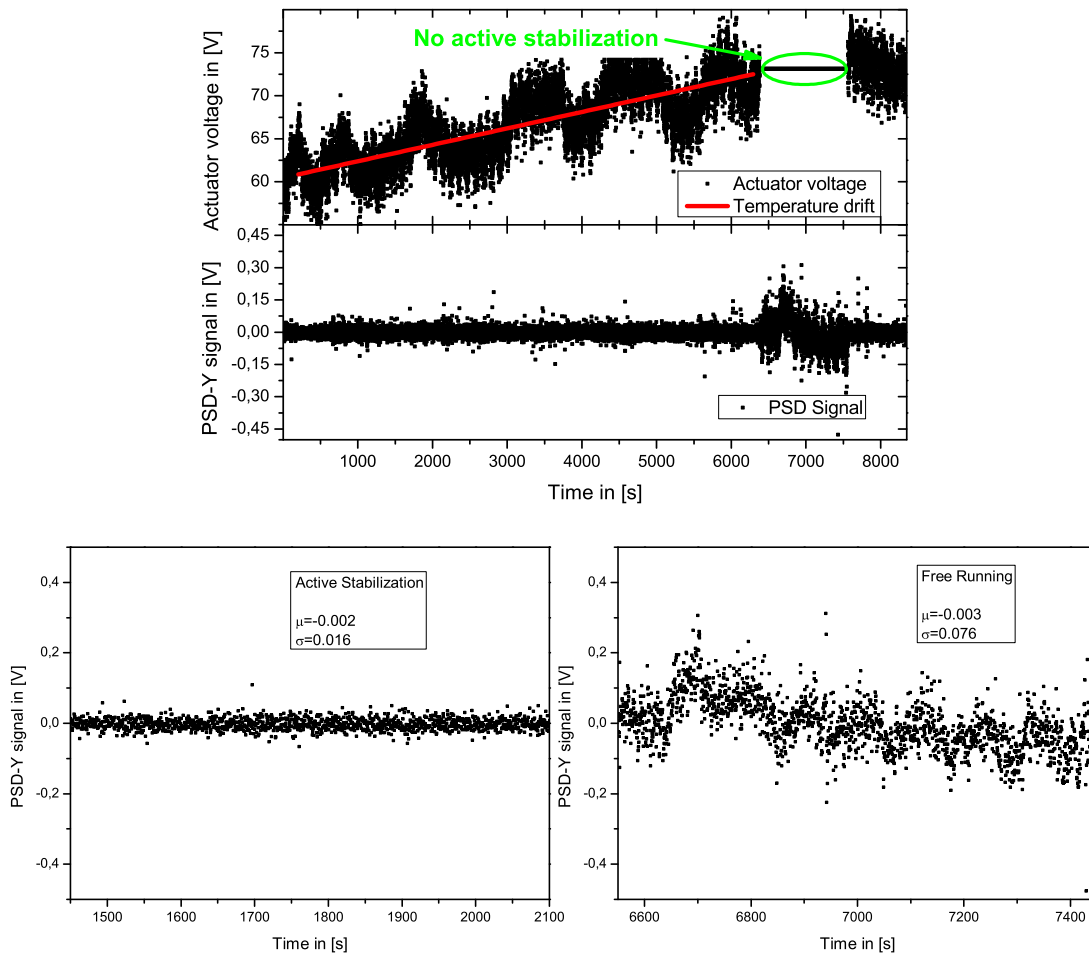


Figure 3.17: Long-term performance of the laser transfer beamline for actuator voltage and the PSD-signal (for the Y-axis). After about 6400 seconds the active stabilization was turned off. The magnified parts show that the standard deviation grows by a factor of 5 in the unstabilized case.

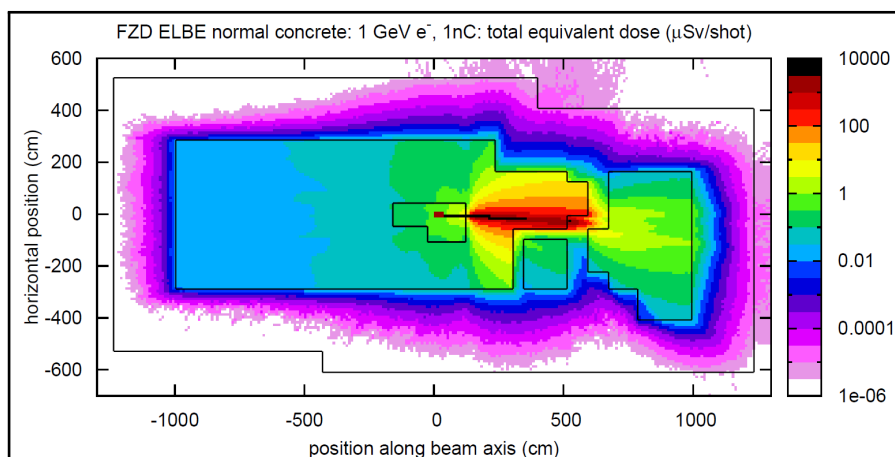


Figure 3.18: FLUKA simulation results by M. Gross for the estimated total equivalent dose distribution for a laser wakefield driven source.

which where necessary to suppress the influence of laser focusing on the X-ray bandwidth (plane-wave approximation of the laser). Large focal spots are also preferred,

with ω_0 being the size of the focal spot, as subsequently, the increased Rayleigh length z_r ,

$$z_r = \frac{\pi\omega_0^2}{\lambda} \quad (3.4)$$

becomes longer than each beam's pulse length. This ensures an interaction with quasi constant laser field strength [24].

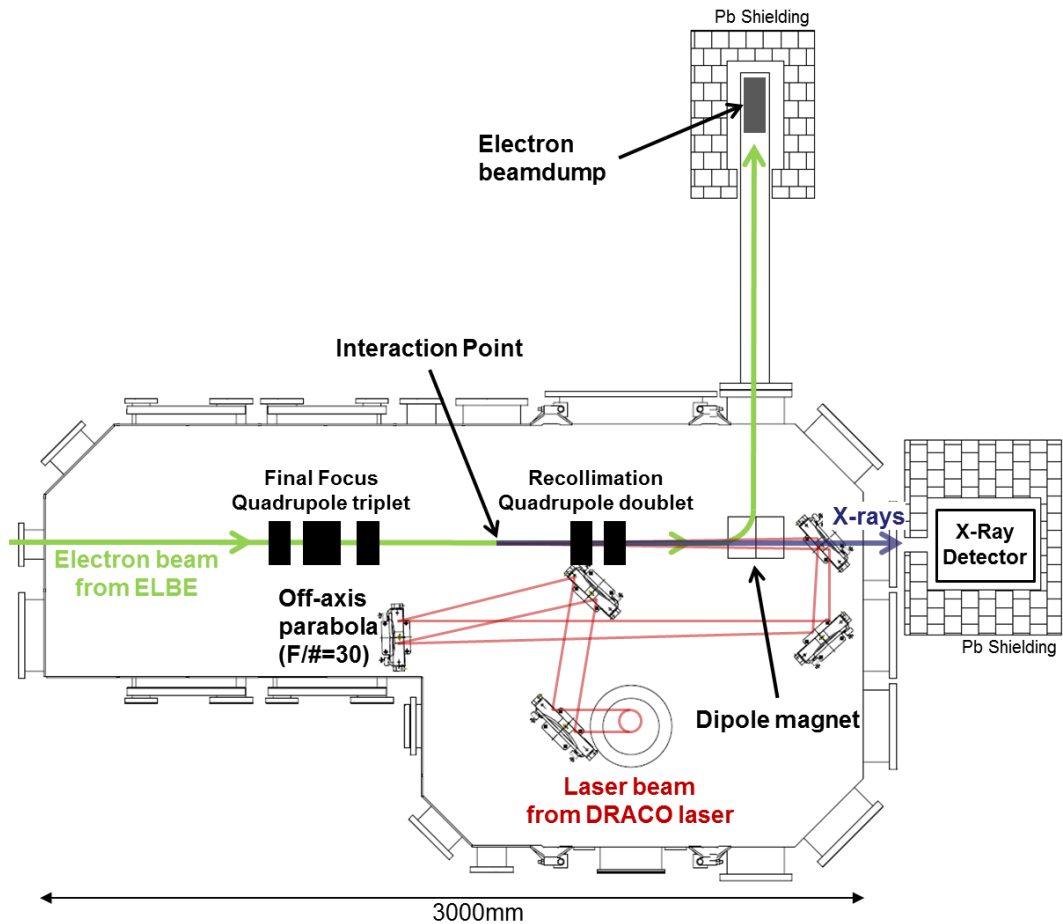


Figure 3.19: Schematic of the PHOENIX target chamber during the experiment including electron beam re-collimation, a dedicated beam-dump and extra lead shielding.

Figure 3.19 shows a schematic of the PHOENIX target chamber. The laser enters the chamber through the ceiling. An 8" mirror reflects the beam into the horizontal plane where it is focused by an $f/30$ off-axis parabola to the interaction point (IP). The electron beam enters the target chamber from the left of the image. A permanent magnet quadrupole triplet focuses the electron beam onto the interaction point. After the scattering, the electron beam is recollimated by a quadrupole doublet system, before a C-shape permanent magnet dipole deflects the beam towards the electron beam dump. The backscattered photons propagate from the interaction point to the last folding mirror, which has a 5 mm aperture along the X-ray propagation axis. This creates a pencil beam that is detected by the X-ray detection system. The detection system, as well as the electron beam dump, are enclosed by several layers of lead to suppress background photons during the measurement.

3.3.2 ELECTRON BEAM FOCUSING SETUP

A bright source requires the interacting beams to be tightly focused onto each other as a direct consequence of the small Thomson scattering cross-section [24]. For an electron beam with a given diameter, the achievable spot size decreases with the focal length of the focusing lens. The space near the target plane, the vacuum environment and the clear aperture for the counter-propagating laser pulse as well as the electron beam had to be considered during the design of the magnetic lens. The in-vacuum setup and the compactness requirements favored a design using permanent magnets, in comparison to a conventional current driven quadrupole.

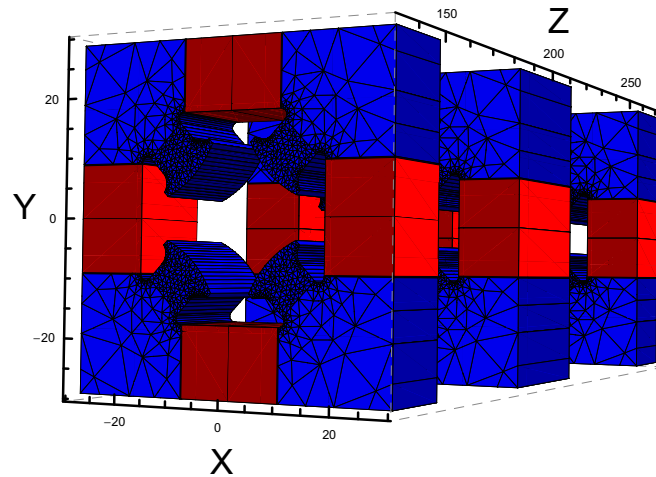


Figure 3.20: Mesh model of the simulated permanent magnet triplet (PMT) consisting of iron yokes (blue) and permanent magnets (red).

Because of the large magnet aperture, a pure Halbach design [89], as used by other groups [90, 91], was ruled out. The decision to build a hybrid system with iron yokes and Sm2Co17 permanent magnets was based on the simplicity of the needed magnet shapes and the field quality that is achieved via the precise hyperbolic shape of the yoke tips. The Sm2Co17 magnets used, offer a sufficiently high remanence of between 0.8 and 1.1 T and a very high Curie-temperature of 800°C.

A *RADIA* code [92] mesh model of the final design for the entire triplet without supporting frames and actuators is shown in Fig. 3.20. The clear aperture is 20 mm, and the field strength at the pole is 0.2 T, resulting in a field gradient of 20 T/m. The results from the magnetic field simulation were used in a *GPT* [63] particle tracking simulation in order to find the optimal magnet spacing geometry. The tracking simulation outcome is shown in Fig. 3.21 for five different transverse normalized emittance values from 0.2 to 20π mm mrad. The resulting focal spot sizes are summarized in Table 3.1 [93].

Subsequently, the sensitivity to alignment errors (see Fig. 3.22) of the individual quadrupoles in the triplet were analyzed. Tilting around the *x/y*-axes leads to higher order aberrations but does not change the spot size to first order. An offset of one of the lenses steers the beam and changes the pointing but the spot size maintains the same. In contrast, a rotation around the beam propagation axis mixes the primary planes in *x* and *y* and causes large focal spot deviations, as illustrated in Fig. 3.23.

Based on the results from the error analysis, a mounting system was developed that allowed position tuning in all relevant axes of the individual quadrupoles and the triplet itself. Figure 3.24 shows a CAD-model together with a single quadrupole mounted on a dummy frame.

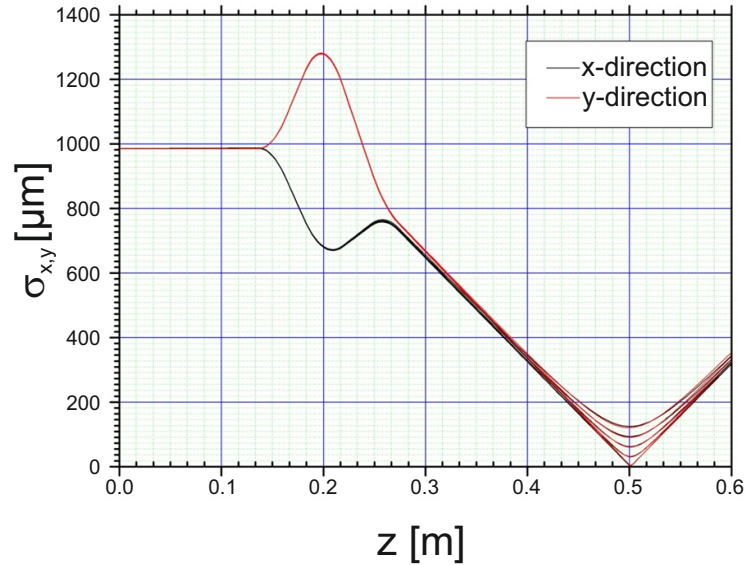


Figure 3.21: GPT results for a particle tracking simulation through the final focusing permanent magnet quadrupole triplet for various emittance values [93].

transv. norm. emittance mm mrad	x-radius (rms) μm	y-radius (rms) μm
0.2	2.5	4
5	31	30
10	62	60
15	93	90
20	125	121

Table 3.1: Spot size values from GPT simulations with simulated ideal quadrupole fields [93].

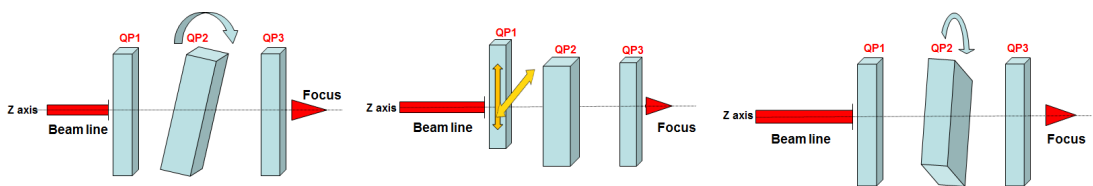


Figure 3.22: Illustration of the parameter variation for the error analysis of the permanent magnet triplet [93].

While assembling the quadrupoles, four permanent magnets with quasi identical magnetic strength were selected. The air gaps between the magnets and the yokes were filled with sheet metal of various thicknesses to compensate any manufacturing errors.

Consequently the field map of every quadrupole and the triplet had to be measured. Becker et al. [94] developed a method that was adapted to the actuator and control system planned for the permanent magnet triplet (PMT) by O.Zarini [93]. The core idea of the technique is to keep the Hall-probe fixed during the entire mapping process so as to minimize the measurement errors and allow for an automatic measurement with high spatial resolution better than $10\mu\text{m}$.

Scanning the B -field along the z -axis away from the quad centers shows the effec-

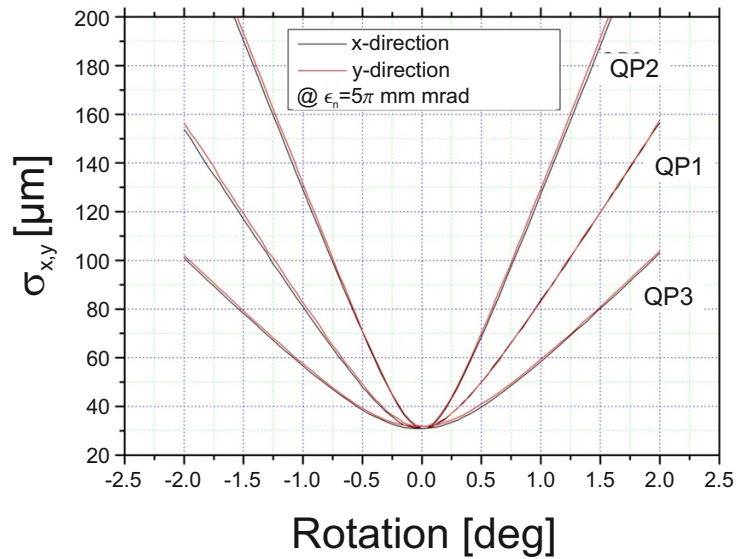


Figure 3.23: GPT simulations for the spot size dependence of the electron beam focus on the rotation of the individual quadrupole lenses [93].

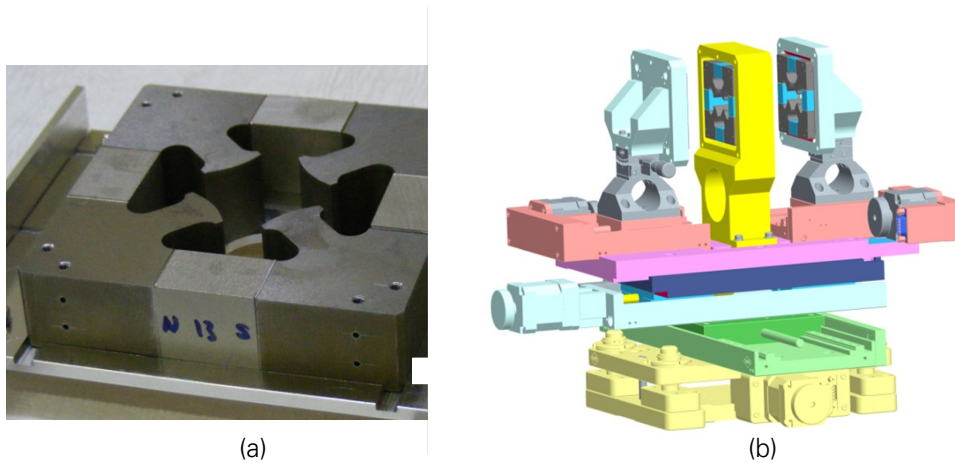


Figure 3.24: (a) Photo of an outer quadrupole lens with CNC-milled iron yokes and SmCo magnets. (b) 3D CAD model of the assembled final focusing PMT.

tive length of the magnets with their fringe fields. As is clearly visible in Fig. 3.25, the fields extend the magnets. The measurement is limited to the maximum displacement of the z-translation stage that moves the hall probe and the stability of the probe holder itself. For magnet configurations with small distances between the center magnet and the outer quadrupoles, the fields start to overlap and disturb each other. This defines an exclusion region for the moveable quadrupoles.

During the experiment, the chosen triplet settings were based on the best signal to noise ratio of the X-ray detector. Large beam radii within the triplet were a consequence of strong focusing, where the individual quadrupole separation is at the maximum travel range of the actuators. The related beam halo that was clipped in the magnets and yokes led to a tremendously increased X-ray background signal. Furthermore, the smallest possible spot sizes led to imperfect recollimation by the simple doublet system, which caused beam loss in the line towards the electron beam dump. This beam loss also added to the X-ray background. Consequently, a shallow focusing with a larger spot size was chosen. This supports the attempt, to exclude the focusing

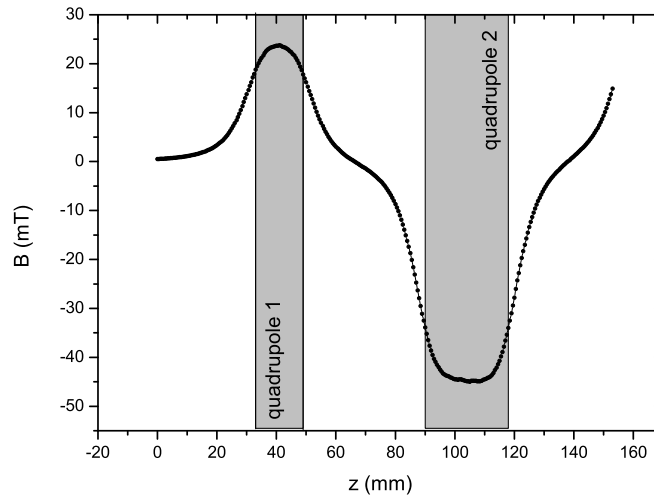


Figure 3.25: z-scan of the B-field close to the quadrupole axis. The fields of the magnets start to overlap which defines a minimal distance between them.

influence of the beam divergence on the backscattered X-ray bandwidth.

Figure 3.26 shows one ELBE focus that was used during the campaign. It forms an elliptical spot with major and minor axis $a = 136\mu\text{m}$ (rms) and $b = 103\mu\text{m}$ (rms). The pointing jitter from the electron linac is below 1% of the beam focus size.

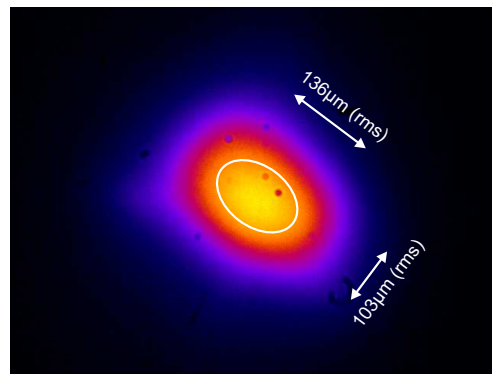


Figure 3.26: The measured focus after the final focusing PMT forms an elliptical spot with major and minor axis $a = 136\mu\text{m}$ (rms) and $b = 103\mu\text{m}$ (rms).

3.3.3 LASER BEAM FOCUSING SETUP

The smallest achievable spot size for a laser pulse with a flat wavefront is defined by the f -number of the focusing optic. To avoid an intensity-dependent nonlinear phase shift [95] and maintain the compressed pulse duration, only reflective optics can be used after the laser beam passed the compressor unit. In the PHOENIX setup, off-axis parabolas are used to focus the laser. The effective focal length of these optics is chosen depending on the desired spot size or Rayleigh length z_r from Eq. 3.4.

The laser wavefront needs to be flat throughout the interaction region in order to eliminate broadening effect related to various \mathbf{k} -vectors [24]. This is necessary for the characterization of the X-ray source and to study the fundamental kinematics during the interaction of both beams. This favors long Rayleigh lengths. In Section 4.1 the timing jitter was estimated to be about 1 ps, corresponding to $300\mu\text{m}$ interaction

length. This interaction length sets a lower threshold for the effective focal length of the parabola

$$f^2 \geq \frac{\pi}{8\lambda} D^2 c\tau_{\text{jitter}} \quad (3.5)$$

where D is defined as the 4σ beam diameter [96, 97] in the near field plane of the laser.

The maximum laser focal length in the PHOENIX setup is defined by the mirror coating damage threshold, the target chamber geometry and the interaction scenario. For a head-on collision, a final folding mirror is needed to overlap the propagation axes of the laser and the electron beam. This mirror has a 5 mm aperture at the center for the detection of X-rays. The target plane, and therefore the maximum distance to the folding mirror, is fixed in the chamber because of the position of flanges for diagnostics (see Fig. 3.27). This leaves the focal length as the single parameter to control the fluence on the folding mirror. This leads to the inequality

$$\text{distance}(\text{target plane} \rightarrow \text{folding mirror}) \geq \frac{1}{3} f \quad (3.6)$$

which includes a safety margin (factor of two) due to the projection on the mirror and the mirror coating's specified damage threshold of $1300 \text{ mJ}/\text{cm}^2$ [98] in the femtosecond pulse regime.

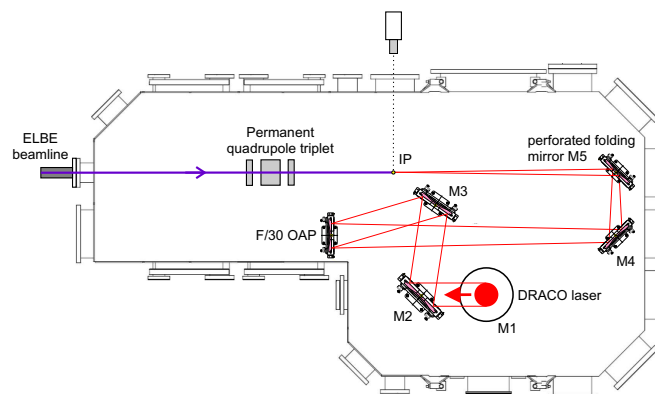


Figure 3.27: Schematic of a backscattering experiment setup with electrons from a conventional accelerator. Both beams collide at the interaction point IP.

With all these considerations, a focusing optic with 3 m focal length was chosen. This optic can later be used in experiments for wakefield acceleration in low density gas targets [99].

The achieved focal spots were measured in two diagnostic setups: a high precision measurement at the target plane and via a monitor beam from the leakage through a mirror. A slow ($f/10$) achromat lens was used to minimize aberrations of the focal plane image. Using a refractive optic required an attenuation of the beam energy by several orders of magnitude, which was realized by multiple glass wedges. With this setup it was also possible to image the focus for pulse energies of more than 4 Joules. This setup cannot be used during the operation of the electron linac because the necessary pickup mirror is on the electron propagation path.

Therefore, a transmission online diagnostic setup was developed as the internship project of J. Couperus (U Twente, NL). The internship project's title was "Diagnostics for future Thomson-backscattering and Laser Wakefield Acceleration experiments" and included the laser diagnostic design for the PHOENIX target area. These diagnos-

tics are built to show shot-to-shot deviations or long-term deviations of beam parameters and not actual spot sizes. A schematic is shown in Fig. 3.28. A plano-convex

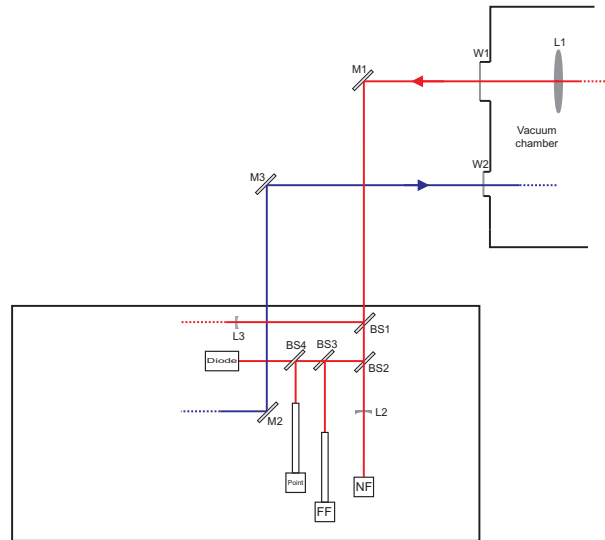


Figure 3.28: Transmission Online Diagnostic setup for important beam parameters such as far field, near field, pulse energy and pointing.

lens with 1.5 m focal length (L1) picks up the 2% leakage through the M2 mirror (see Fig. 3.27). A beam splitter (BS1) splits up part of the light for the stretcher setup while the rest is distributed to a far field (FF) camera, a PSD-detector (Point) (see Subsection 3.2.2) and a calibrated photodiode. The photodiode is used to monitor the beam energy during long-term operation. A second plano-convex lens (L2) is used to re-collimate the beam and to image a near field (NF) plane upstream in the beamline. The stretched probe beam re-enters the target chamber via another window (W2).

An early far field image from the setup is shown in Fig. 3.29b. The laser beam has a bandwidth greater than 50 nm and illuminates more than 50% of the lens. This leads to large spherical and chromatic aberrations of the focal spot. The energy of this diagnostic pulse can be as large as 100 mJ with a pulse duration of 100 fs stretched from its original 30 fs by propagating through the 25 mm thick turning mirror M2. Therefore, the power of the probe pulse is about 1 TW which is three orders of magnitude greater than the critical power P_{cr} for self-focusing in fused silica. This onset of filamentation of the beam in the lens and even more in the out-coupling window (W1) massively degrade the focus quality. The pointing position and energy transfer through the diagnostic setup is independent of these aberrations to first order.

The comparison with the HQ imaging setup from the target plan (Fig. 3.29a) indicates that there are intrinsic wavefront errors, not originating from the online diagnostic setup.

Figure 3.29 shows a focus that has significantly more energy deposited in the wings compared to a focus that was measured in a target chamber adjacent to the compressor unit without a dedicated beamline [100] (see Fig. 3.30).

The characteristic shape of the measured focus in Fig. 3.29a indicated that the origin of the focus degradation is not located in the final focusing off-axis parabola, but mainly in the transfer beamline. The source for the wavefront errors leading to a bad focus were suspected in the deformations of the large flat mirror optics caused by their own weight and the mirror mount design. The dominant Zernicke polynomial that one would expect after propagating a beam along optics deformed in such way is coma ($\sim 3 * x^2 * y + 3 * y^3 - 2 * y$). Coma can be seen as a combination of two

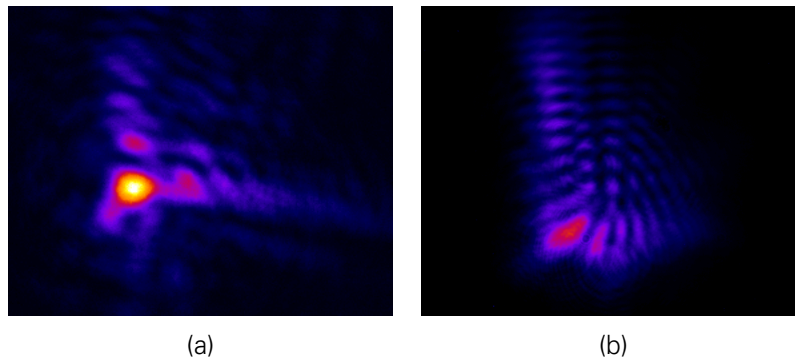


Figure 3.29: (a) High resolution image of the $f/30$ OAP-focus at the interaction point before closed-loop optimization. (b) Related transmission online diagnostic measurement result to monitor focus changes during operation when the HQ imaging setup is not accessible.

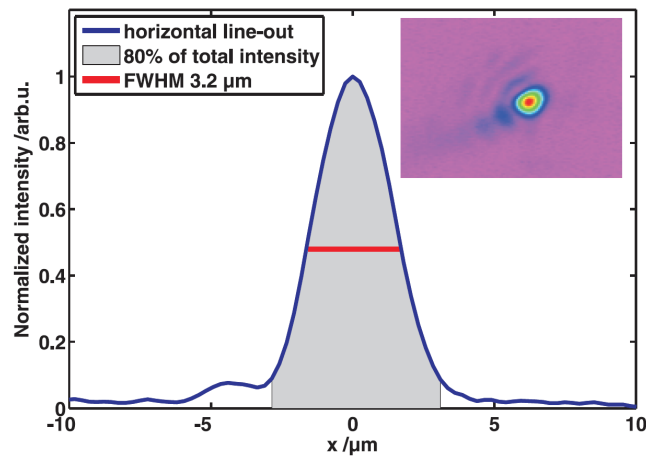


Figure 3.30: Total equivalence dose decay per shot along the z-axis in the beam forward direction

aberrations, spherical aberration and astigmatism. This hypothesis was backed up by a simple far field simulation. Assuming a perfect Gaussian beam in the near field, a wavefront deformation with coma as the leading distortion term would result in a focus as shown in Fig. 3.31, which has similar far field features to those shown in Fig. 3.29.

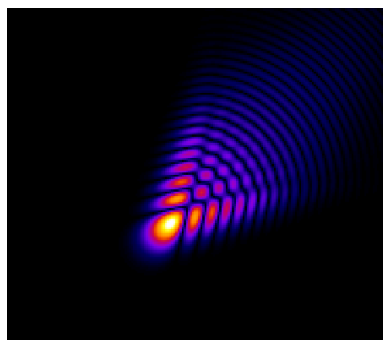


Figure 3.31: Simulated focus for a wavefront deformation with coma as the leading distortion term.

To improve the focal spot quality, we installed a «*Phasics*» *SID4* wavefront sensor [101], in a closed-loop with the deformable mirror independent from the sensor in the Draco diagnostic setup before the transfer beamline, in a closed-loop with the deformable mirror. By doing this, the wavefront errors were pre-compensated with the result of a significantly improved focal spot as shown in Fig. 3.32. The spot size is nearly diffraction limited with diameter $d = 35\mu\text{m}$ (FWHM).

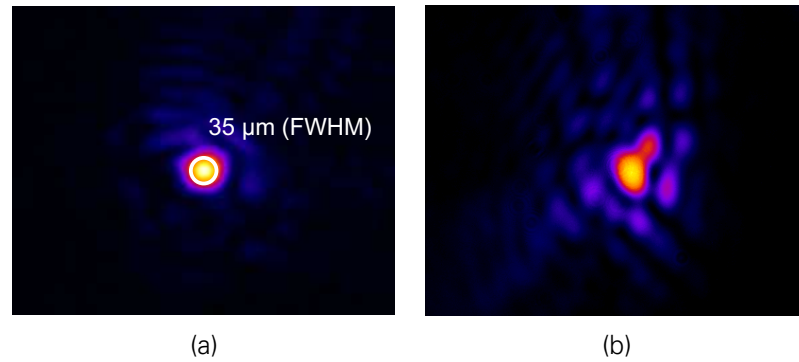


Figure 3.32: (a) High resolution image of the $f/30$ OAP-focus at the interaction point after closed-loop optimization. (b) Related transmission online diagnostic measurement result to monitor focus changes during operation.

4 PHOENIX COMMISSIONING EXPERIMENTS

Synchronization A schematic of the synchronization and timing system is shown in Fig. 4.1. The system master-clock is a low phase-noise 13 MHz RF oscillator within the ELBE low-level radio-frequency (LLRF) setup. From this oscillator, all frequencies that are required to operate the linac are derived using phase-lock loops (PLL) [102] such as 260 MHz for the buncher pill-box in the injector or 1.3 GHz for the operation of the super-conducting cavities and other part specific frequencies. The phase of the laser pulses and the RF field are synchronized by phase-locking the 6th harmonic of the laser oscillator repetition rate to the 30th harmonic of the LLRF master-clock at 390 MHz. The phase mixing of both signals and the generation of a phase-error proportional feedback-signal to tune the laser oscillator cavity length [103] is realized by the commercially available «*FEMTOLASER*» *FEMTOLOCK* device. Through this, the repetition rate of the laser oscillator follows the frequency of the master-clock.

The arrival time jitter between laser pulses and electron bunches on target includes the contribution from each of the individual unit's timing jitter during the propagation of the laser and electron bunch, as well as the reference signal distribution links. For signals with MHz repetition rate, the timing jitter is determined via a phase noise measurement relative to a carrier frequency (using the Rohde&Schwarz FSUP Signal Source Analyzer [104]) with

$$J_{\text{rms}} = \frac{1}{2\pi f_c} \sqrt{2 \int_{f_1}^{f_2} L\{f\} df} \quad [s] \quad (4.1)$$

where f_c is the carrier frequency and $L\{f\}$ the phase noise within the bandwidth df .

Figure 4.2 shows an example of the result of one of these measurements. It illustrates the increase of the timing jitter of the 13 MHz reference signal that is used to synchronize the laser oscillator by inserting a phase mixer (IQ modulator [105]), necessary for the subsequent timing.

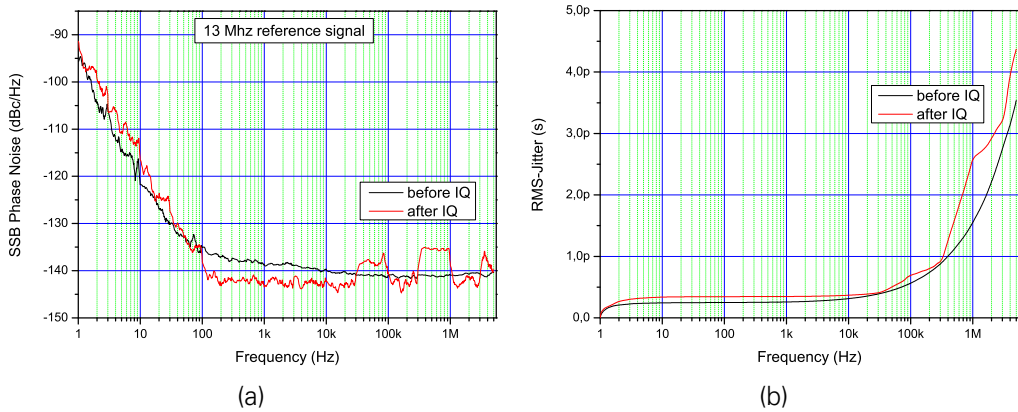


Figure 4.2: (a) Exemplary results of a phase noise measurement for the reference signal with or without the subsequent IQ phase shifter. (b) Jitter as integrated phase noise of the same measurement for the considered bandwidth between 1 Hz and 10 MHz.

The contribution to the arrival time jitter is illustrated in Fig. 4.3. The contribution from the laser chain is dominated by the path length differences related to pointing jitter in the transfer beamline. The total laser synchronization is limited by the reference signal distribution unit (optical fiber link with subsequent PLL) with an integrated timing jitter of about 600 fs. The timing jitter for the combination of laser oscillator and *FEMTOLOCK* unit is determined to be 200 fs. The electron bunch arrival time

jitter was measured with 500 fs at a repetition rate of 13 MHz using a beam position monitor (BPM) signal.

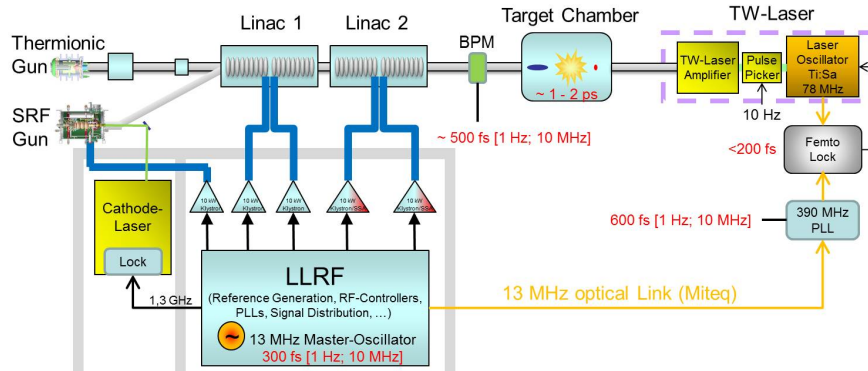


Figure 4.3: Pictogram of the ELBE/DRACO synchronization system including jitter estimates in red [106].

The total arrival time jitter between both pulses at the target plane is estimated at 1 – 2 ps which is longer than the laser pulse duration and about equal to the electron bunch duration. In order to minimize timing jitter influence and ensure scattering events in every laser shot, a head-on geometry ($\varphi = 180^\circ$) was chosen, as illustrated in Fig. 3.19, for a reliable interaction within the laser’s Rayleigh length.

Timing As previously mentioned, an adjustable time delay is necessary to compensate the path length difference of both machines from their source point to the target plane. A schematic overview of the ELBE/Laser timing diagram is shown in Fig. 4.1. From the 13 MHz-master-clock, a synchronized 10 Hz-signal is derived with a digital counter. This 10 Hz-signal serves as the external trigger signal for the “Hamburger” electron pulse picker and the *GenPulse* laser timing control unit. The signal from the digital counter to the *GenPulse* can be delayed with a digital delay generator (SRS DG645 [107]). The *GenPulse* creates the laser T_0 reference signal by a logic AND-gate with the inputs of the 10 Hz-external trigger and the 78 MHz-signal from the oscillator cavity. All delays to run the laser system (flash-lamp triggers, Pockels cell triggers, etc.) refer to T_0 .

The 10 Hz gating of the ELBE linac is necessary in order to use slow X-ray detectors with integration times much longer than the pulse-to-pulse interval. The laser repetition rate is limited to 10 Hz. Without the external gating of the linac electron bunches that did not interact with a laser pulse, would also arrive at the beam dump. The resulting bremsstrahlung would be integrated during the data acquisition of the slow detectors and decrease the signal-to-noise ratio dramatically.

As a result of the synchronization and external triggering, laser and electron pulse trains with a repetition rate of 10 Hz and a constant temporal offset (≤ 50 ns) arrive at the target plane. T_0 can be delayed in steps of 12.8 ns (as a consequence of the logic AND-gate) by the SRS DG645 delay generator to reduce this temporal offset. The temporal offset in the $\mu\text{s}/\text{ns}$ -regime is measured with an oscilloscope by comparing the signals from the integrating current transformer (ICT) and a photodiode. The scope traces from such a measurement are shown in Fig. 4.4 for a pulse separation of 1 ns.

The fine-tuning of the temporal overlap is achieved by an analogue phase shifting unit (IQ modulator [105]) in the 78 MHz laser oscillator signal line to the *FEMTOLOCK* unit. The IQ modulator can shift the phase between 0 and 360 degree, corresponding

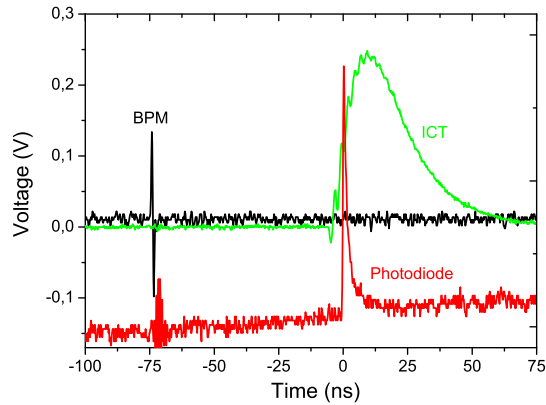


Figure 4.4: Oscilloscope traces for the determination of the temporal beam overlap in the ns-range. The beam position monitor (BPM) is located upstream in the beam-line with minimum cable length. Taking cable lengths and time-of-flight into account, the pulses are within 1 ns.

to 0 ... 12.8 ns with a step size of 250 fs. The IQ modulator is built in series with the signals from the laser oscillator to the *FEMTOLOCK* phase-locking unit required for synchronization. Its phase noise adds to the total arrival time jitter and was quantified with the results shown in Fig. 4.2.

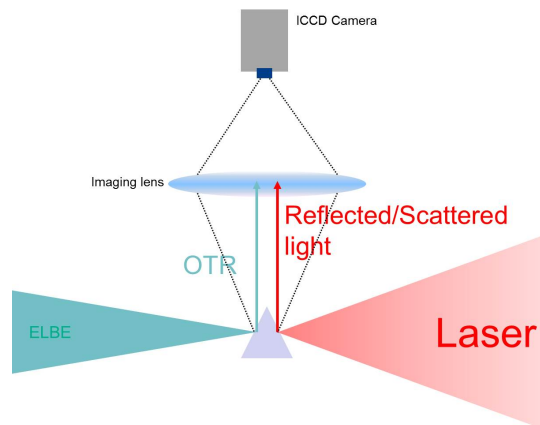


Figure 4.5: Schematic illustration of the sub-nanosecond optical arrival time detection system.

To minimize the scanning window when finding the initial temporal overlap, a high resolution optical arrival monitor (Fig. 4.5) was developed. It consists of a polished metal coated prism that can be driven in and out of the target plane. On one side, the laser light is reflected and imaged into a fast iCCD camera [108] with a temporal resolution of 200 ps. When the electron bunch propagates through the surface of the other prism side, optical transition radiation (OTR) [109, 110] is created and also imaged with the same lens into the iCCD camera. The integration window length can be chosen and gradually reduced to 200 ps ensuring both spots appear on the camera image by shifting the 78 MHz signal phase with the IQ modulator. The laser had to be attenuated by several orders of magnitude to not saturate the iCCD camera. Once the initial overlap is found, the X-ray yield is maximized by shifting the 78 MHz signal phase.

4.2 CHARACTERIZATION OF THE X-RAY DIAGNOSTIC SETUP

In the PHOENIX diagnostics setup, X-ray detectors are used to define the interaction point and temporal overlap, as well as for the energy-angle correlation measurement. All of these sensors are used to minimize the bremsstrahlung signal from the beam-lines or beam dump in order to optimize the signal-to-noise ratio.

The interaction point is defined as the charge center at the electron beam focal plane. The charge distribution was measured with a $20\mu\text{m}$ tungsten crosshair scan while simultaneously detecting the resulting bremsstrahlung with a scintillator detector (Hamamatsu R7400U PMT + BaF2 crystal [111]).

A typical oscilloscope trace for the x-direction with FWHM width $165\mu\text{m}$ is shown in Fig. 4.6. The achieved position accuracy exceeds the lanex phosphor screen resolution which is about $\sim 100\mu\text{m}$. Subsequently, the pilot laser was directed onto the same crosshair and the resulting diffraction pattern, measured on the laser focus diagnostic camera, was used to find spatial overlap.

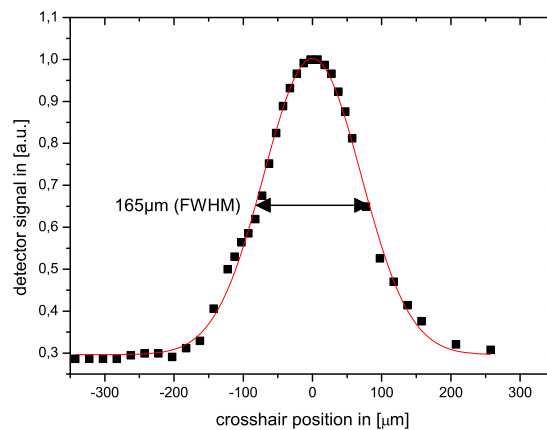


Figure 4.6: Transverse electron beam profile ($165\mu\text{m}$ FWHM) measured with the wire scan technique.

For the in situ monitoring of the temporal overlap an «AmpTek» XR-100T-CdTe detector was used [112]. It is a single pixel semiconductor detector with an active area of 5 mm by 5 mm and 1 mm thickness. It can be operated in the single-photon regime, which is necessary to achieve high temporal sensitivity. At the same time, the X-ray photon spectrum can be measured. Depending on the energy of the incoming photon, a number of electron/hole pairs is created inside the active volume. The resulting charge is directly related to the photon's energy.

The quantum efficiency of the detector is flat throughout the X-ray spectral region that is accessible with the ELBE driven setup as shown in Fig. 4.7.

The energy resolution of the XR-100T-CdTe detector depends on the exact amplifier configuration. For the calibration of the detector setup, a ^{214}Am source has been used.

Figure 4.8 shows a histogram recorded with the XR-100T-CdTe. It shows numerous peaks that were compared to known transitions from the *National Nuclear Data Center* database [113]. The inset of Fig. 4.8 shows a linear relation between ADC channel number and photon energy. The width of the 13.9 keV peak reveals an energy resolution of 0.8 keV (FWHM). The XR-100T-CdTe detector is a well established tool within the X-ray spectroscopy community and serves as a reference to cross-check measured fluxes and spectra from other diagnostics.

For an enhanced understanding of the kinematics during the scattering interaction of the laser pulse with the electron bunch, the spatial and energetic resolution has

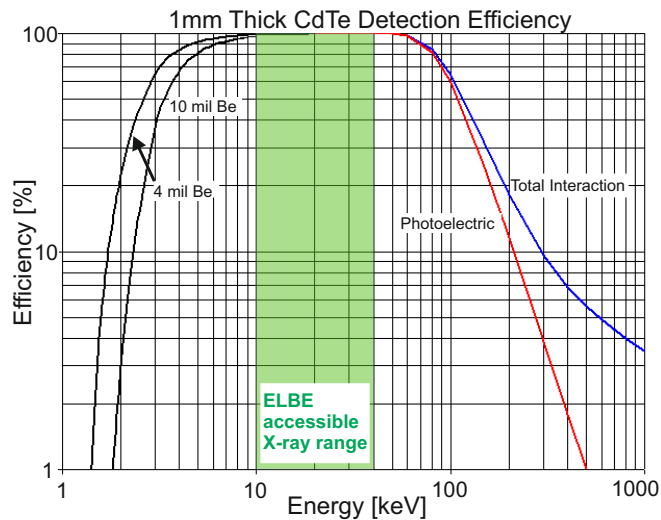


Figure 4.7: Quantum efficiency of the «AmpTek» XR-100T-CdTe detector (Efficiency curve from Amptek website [112]).

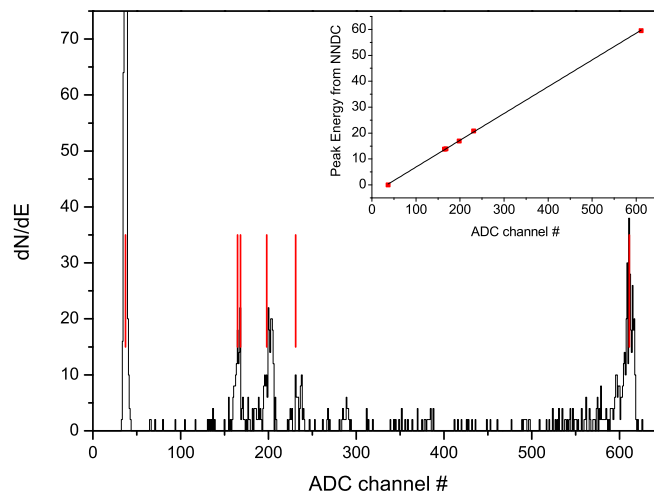


Figure 4.8: Calibration measurement of the XR-100T-CdTe detector using a ^{214}Am source.

to be much higher than is achievable with the semi-conductor detector setup. For this reason, an X-ray CCD camera has been employed to measure the energy-angle correlation with unprecedented resolution in matters of observation angle and X-ray photon energy.

The model used during the experiments is an «ANDOR Technology» DY420-BR-DD depicted in Fig. 4.9. It is actively cooled to minimize electronic noise from the CCD chip.

In the detector setup geometry at PHOENIX, the CCD is directly exposed to the generated X-ray light. For an increased quantum efficiency in the medium-energy range of 5 keV to 20 keV, a deep-depletion CCD-type camera has been used which consists of a thicker $40\mu\text{m}$ epitaxial layer compared to the standard thickness of about $20\mu\text{m}$.

When X-ray photons with an energy less than 100 keV propagate through the active layer of the CCD chip, they lose energy predominantly because of the photo-electric effect [115]. Dependent on the photon energy a certain number of electron-hole pairs is created. On average, an energy of 3.65 eV is necessary to create one pair in



Figure 4.9: Image of the «ANDOR Technology» DY420-BR-DD camera (Image from Andor Technologies website [114]).

silicon. The photon energy is deduced by summing up the entire created charge. It is crucial that the charge is collected within one pixel to maintain the correlation between charge and photon energy. The correlation is lost if the photon is absorbed in the border region between two or more pixels. Even though the generated charge cloud diameter is below $1\mu\text{m}$ [116], the charge diffuses and expands before it is collected in an individual pixel potential well. This effect is called charge-splitting and destroys the direct correlation between photon energy and pixel charge. The resulting cluster events (1x2, 2x2, 1x3 etc), as shown in Fig. 4.10, can be analyzed at the cost of significant reduced spectral resolution [117].

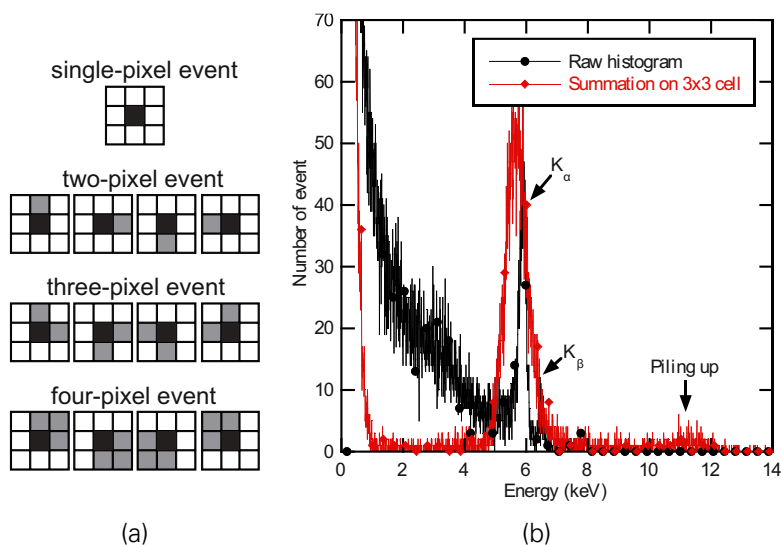


Figure 4.10: (a) An example of single- and multiple-pixel events. The dark pixels represent the counts above the single-pixel threshold and the shaded pixels show the counts between the single-pixel and multiple-pixel thresholds. (Image based on Princeton Instruments website [118]). (b) Broadening of the detected linewidth of an ^{55}Fe source due to multi-pixel events. (Image from [117])

As a consequence, only a fraction of the entire X-ray beam was directed onto the CCD detector which is positioned at a distance of 1915 mm from the source to use the divergence of the X-ray beam in order to further reduce the photon flux to 7500 photons per shot for an area of 65000 pixels (see Table 4.1). The used area of the CCD chip is about equal to the size of the XR-100T-CdTe active area but because of the pixelation the likelihood of electronic pile-up, where more than one photon hits one

pixel, is dramatically reduced. Hence, a single-pixel-absorption-event (SPA-E) analysis can be used to maintain the direct photon energy/pixel charge correlation at an energy resolution of 30 eV per bin.

Number of X-ray photons	
At interaction point	7×10^5
In beamlet after 5 mm aperture	1×10^5
After attenuation (windows, air,...) & quantum efficiency	7500

Table 4.1: Simulation results for the photon yield assuming a laser power of 4 J and a bunch charge of 50 pC at 24 MeV focused to 50 μ m respectively 165 μ m (FWHM) spot size. The beamlet is recorded with a CCD camera using an area of 5 mm \times 5 mm of the chip.

For the calibration between ADC channel number and photon energy two radioactive sources, ^{241}Am and ^{55}Fe , were used with the results shown in Fig. 4.11. The numerous peaks that were again compared to known transitions from the *National Nuclear Data Center* database [113]. The inset of Fig. 4.11 shows a linear relation between ADC channel number and photon energy. The width of the 5.9 keV peak of ^{55}Fe reveals an energy resolution of 100 eV (RMS). The bandwidth resolution is limited by incomplete charge collection or charge-transfer-efficiency (CTE). Due to recombination effects for charge clouds further away from the pixel potential well, the charge may not be conserved.

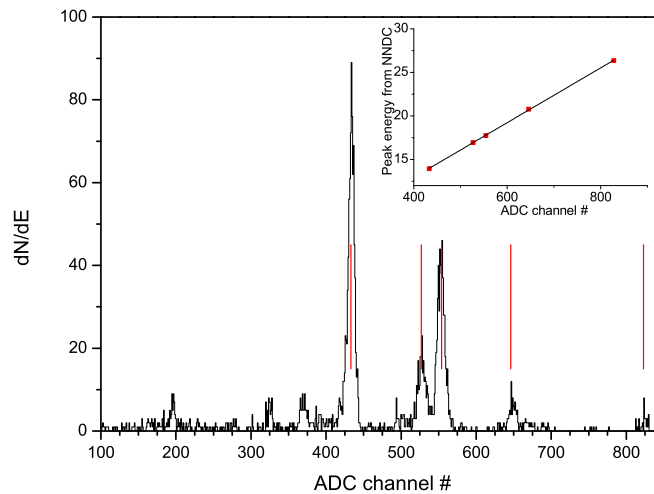


Figure 4.11: Calibration measurement of the «ANDOR Technology» DY420-BR-DD CCD camera using ^{241}Am and ^{55}Fe sources.

The resolution for a relative energy shift is governed by the CCD analog-digital converter. For the «ANDOR Technology» DY420-BR-DD camera the ADC channels are separated by 30 eV (1 bin= 30 eV).

To analyze the measured spectra the effective quantum efficiency (QE) for each channel must be known. Effective QE means that additional to the camera's silicon absorption efficiency, all layers from the source point to the depletion layer of the CCD are taken into account. This includes the target chamber exit window, air, the multiple foils to seal the camera from vacuum and make it light tight and a dead layer of silicon. The sandwich model consists of 143 μ m Mylar foil, 14 μ m polycarbonate, 0.1 μ m aluminum, 25 μ m beryllium, 475 mm of air and a 5 μ m silicon for the dead layer

of the chip [42]. The X-ray transmission curves are taken from the *CXRO* database [119]. In between the database sampling points the effective quantum efficiency curve for the setup was interpolated with linear splines. The model assumes that energy that is not transmitted through an active layer of $40\mu\text{m}$ silicon is absorbed. Scattering probabilities are not included. The resulting QE-curve is shown in Fig. 4.12.

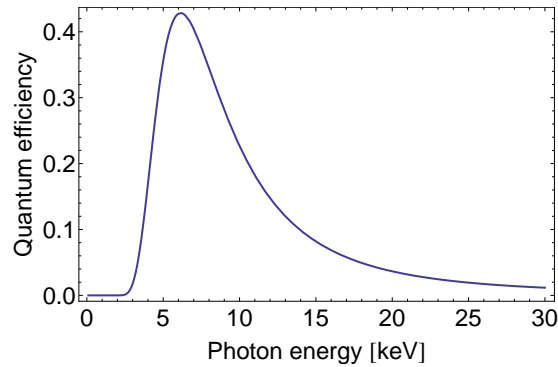


Figure 4.12: Quantum efficiency curve for the «ANDOR Technology» DY420-BR-DD in combination with the filter stack.

4.3 CHARACTERIZATION AND SUPPRESSION OF THE X-RAY BACKGROUND SIGNAL

To measure the X-ray spectrum from the inverse Compton scattering source, the photon yield has to exceed the X-ray background signal. The bremsstrahlung from the interaction of beam halo with beam transportation elements (magnets, apertures, beam tubes) is considered as the main background source. Additionally, there is bremsstrahlung from the originating from the electron beam dump. The bremsstrahlung spectrum is broadband. Only those parts of its spectrum which overlap with the spectral range, accessible with an ELBE driven electron beam, are relevant to the spectrum measurement. The X-ray background from the accelerator cavities (due to field emission, beam halo or energy tails) is suppressed by using a dedicated experimental cave which is surrounded by concrete walls (thickness 3 m) and connected through a dogleg section as shown in Fig. 4.13.

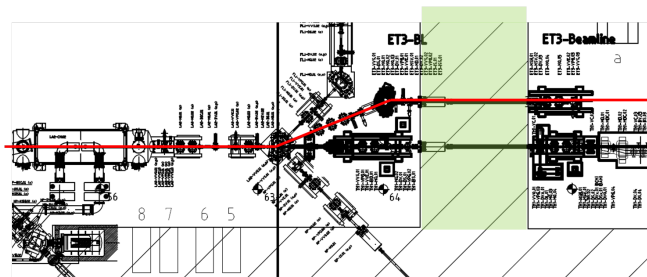


Figure 4.13: Illustration of the electron beam path (red) from the accelerator cave to the PHOENIX target area.

In an early “background study” beam time, a 0.4 T dipole was used to deflect the electrons onto a 20 cm block of aluminum which acted as the beam dump. The X-ray background signal from the operation of the electron linac without the presence of a laser recorded with the CCD camera are shown in Fig. 4.14.

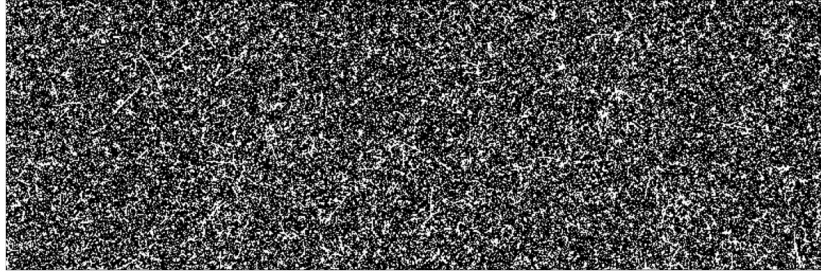


Figure 4.14: Integrated background signal from the CCD camera for 600 shots.

The image contains the integrated background counts of 600 consecutive shots onto the aluminum block. There are still single pixel events that were analyzed and histogrammed, yielding the background spectrum (grey curve) presented in Fig. 4.15. The expected background spectrum in this narrow spectral region is assumed to be flat. The background histogram curve is used to confirm the sandwich model of the CCD with its modeled quantum efficiency.

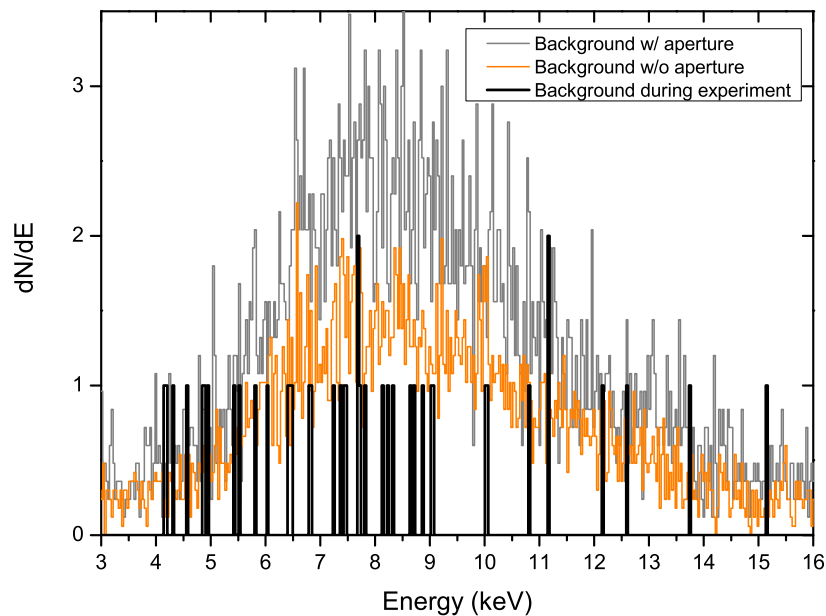


Figure 4.15: Comparison of the background signal before the campaign for a setup with and without additional differential pumping schemes and during the campaign after extensive optimization. All signals are taken with or scaled to an integration time of 60 interactions.

The target chamber vacuum is directly connected to the accelerator cavity vacuum. To meet the accelerator vacuum standards, a series of apertures and vacuum pumps were installed in a differential pumping scheme. The last aperture in the beamline, just before the PHOENIX target chamber was identified as a main source of the bremsstrahlung signal. The aperture diameter was about 5σ of the beam, but fixed in position without the possibility to verify the relative alignment with respect to the beam axis defined by the magnet centers.

A test run without the aperture was granted. The resulting histogram (orange curve) is included in Fig. 4.15. The background signal amplitude is reduced approximately by a factor of two. The measurement confirmed the aperture as a main background source. It was also shown that the accelerator vacuum was undisturbed after the aperture removal.

For the purpose of further attenuation of the background signal, the distance from the X-ray detector to the beam dump was increased. A stronger 1 T magnet was installed to deflect the beam in a 90° angle to a dedicated beam dump chamber with 10 cm lead shielding. The installation of this new beamline required a recollimation of the previously focused electron beam to avoid clipping of the beam causing additional bremsstrahlung.

A schematic of the final setup that was used during the campaign can be found in Fig. 3.19. As a result of all improvements the background counts almost vanished completely as shown in Fig. 4.16. The background SPAE signal can be seen next

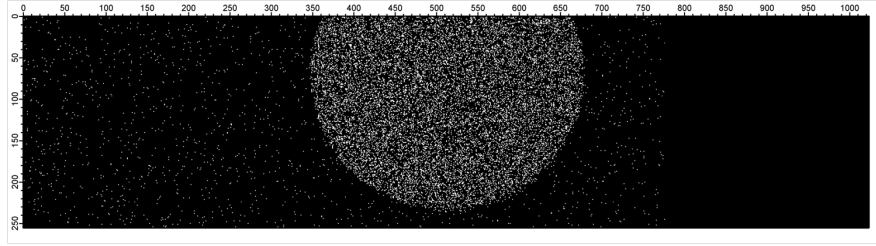


Figure 4.16: PHOENIX pencil beam image after the summation over 900 scattering events.

to the beamlet spot from the ICS interaction, summed up for 900 scattering events. The background histogram resulting from this data is again shown in Fig. 4.15 (black curve). Within the observed spectral range, only four bins have count values greater than one, showing that the background signal is sufficiently suppressed.

4.4 FIRST LIGHT AND γ -DEPENDENCE OF THE X-RAY SPECTRUM

For the first scattering experiments [40], a proven machine setting of the linac was chosen. The kinetic energy of $22.5 \text{ MeV} \pm 0.25\%$ is suitable for the permanent magnet triplet. The electron beam spot size of $\sigma_r = 136\mu\text{m} \times 103\mu\text{m}$ (RMS) is the result of background suppression as explained in Subsection 3.3.2. The projections onto the x- and y-axis are $\sigma_x = 124\mu\text{m}$ and $\sigma_y = 115\mu\text{m}$. The electron bunch duration was 1.7 ps (FWHM) [70]. The laser spectrum has a bandwidth of about 20 nm (RMS) centered at 800 nm, corresponding to a photon energy range from 1.49 eV to 1.63 eV. The laser focal spot size is nearly diffraction limited with $15\mu\text{m}$ (RMS) or $35\mu\text{m}$ (FWHM). Because the spot sizes are different, only a fraction of the total charge in the electron bunch interacts with the laser, and an effective bunch charge is introduced by multiplying the total bunch charge with the spot size ratio of laser and electron beam. A schematic illustration of the interaction geometry is shown in Fig. 4.17 together with the actual beam foci images.

For the analysis of the measured spectra, the charge density and laser intensity are assumed to remain constant within the interaction length L_{int} [24] defined as

$$L_{\text{int}} = (\tau_{\text{laser}} + \tau_{\text{bunch}}) \cdot c/2 \quad (4.2)$$

where τ_{laser} is the laser pulse duration and τ_{bunch} the electron bunch duration. For the experimental parameters $\tau_{\text{laser}} = 210 \text{ fs}$ (rms) and $\tau_{\text{bunch}} = 1.7 \text{ ps}$ (rms), this gives $L_{\text{int}} = 0.3 \text{ mm}$, which is much smaller than the laser Rayleigh length ($z_R = 0.8 \text{ mm}$) and the electron β -function ($z_b = \gamma \frac{\sigma_r^2}{\epsilon_N} = 55 \text{ mm}$) [53]. This results in constant scattering parameters during the interaction.

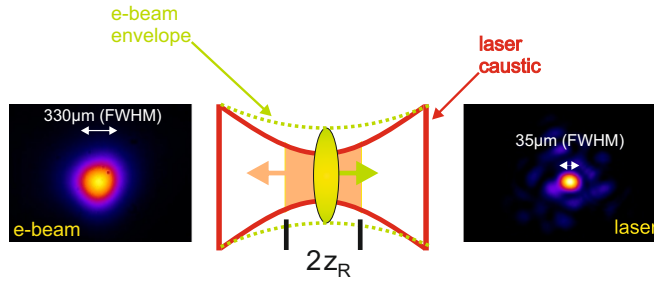


Figure 4.17: Illustration of the spatial beam overlap. The FWHM sizes of the spots are $330\mu\text{m}$ ($140\mu\text{m}$ rms) for the electron beam and $35\mu\text{m}$ for the laser. (Image from [40])

The shallow focusing leads to an almost laminar beam. Using Eq. 3.2 and the measured parameters for the electron beam energy and beam spot size in combination with the measured normalized transverse emittance of $\epsilon_N = 16\pi$ mm mrad, the expected angular spread is very small $\sigma_\varphi \approx 2.6$ mrad. Based on the direct feedback signal, the XR-100T-CdTe semi-conductor detector was used to find the initial temporal overlap. Because the maximum bunch charge of 70 pC would saturate the detector, the total bunch charge was reduced to 2 pC, resulting in a effective interacting charge of 40 fC.

After setting the parameters for both machines, the temporal offset between laser and accelerator was varied. The result of the delay scan is presented in Fig. 4.18. It shows the X-ray yield as a function of temporal offset between laser pulse and electron bunch. The first delay curve was recorded with a total bunch charge of 2 pC and a high laser pulse energy of 1.5 J on target. At the maximum signal position, the detector was saturated. In order to reduce the X-ray flux and to ensure an interaction in the linear scattering regime (laser strength parameter $a_0 \ll 1$), the laser pulse energy was reduced to 100 mJ on target ($a_0 = 0.05$). From this second scan, a magnification around the maximum is shown in the inset in Fig. 4.18. A full width at half maximum of 300 ps was deduced. The low sensitivity to the temporal offset is a result of the larger divergence of the focused laser beam compared to the electron beam, which leads to a better spatial overlap with higher X-ray flux and compensates for the decreasing laser intensity.

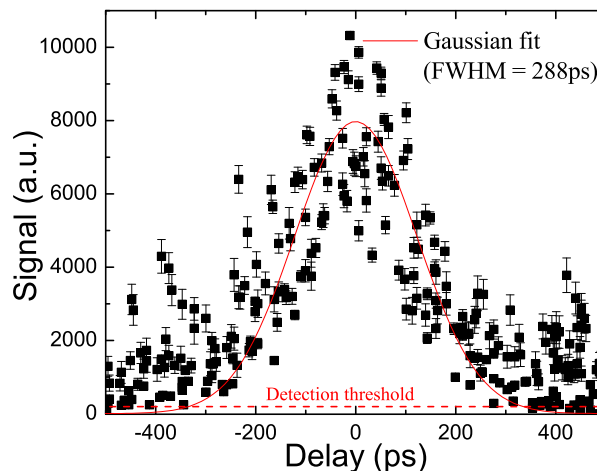


Figure 4.18: X-ray signal yield for head-on collision with variable temporal offset of the interacting pulses [40].

Once the timing was optimized for the X-ray yield, the signal was integrated over 10 minutes in “single photon counting-mode” to measure the X-ray spectrum. For the histogram shown in Fig. 4.19, 6000 interactions were summed up. It is important to remember that because of the different spot sizes of both interacting beams the total interacting charge was only 40 fC. Figure 4.19 demonstrates the achieved high

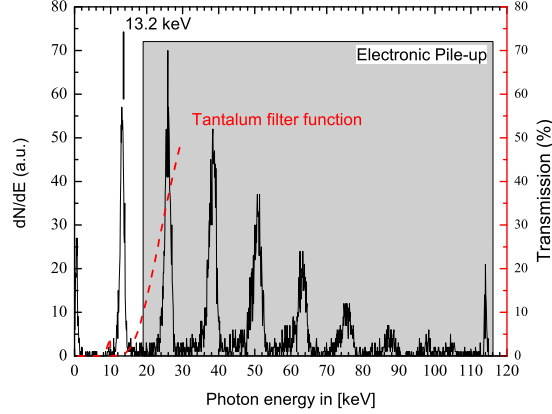


Figure 4.19: Backscattered X-ray spectrum from CdTe detector with pile-ups (black curve) taken with 100 mJ laser energy and 2 pC total bunch charge (40 fC effective charge). After adding tantalum foil filter (red dashed curve) X-ray signal vanishes (Filter data from *CXRO* database [119], Image from [40]).

signal to noise ratio. Clearly visible are a peak at $\hbar\omega \approx 4\gamma^2 E_0$ and peaks at about $2\hbar\omega, 3\hbar\omega \dots 7\hbar\omega$. The latter peaks are the result of electronic pile-up, when more than one photon is absorbed within the detector during one read-out cycle. This was confirmed by inserting a tantalum foil. The transmission function of 25 μ m tantalum is also plotted in Fig. 4.19. For the measured fundamental signal peak at 12.3 keV the foil blocks the X-rays and only real higher harmonics could penetrate the foil. With the foil in place, no signal was recorded, proving the nature of the peaks to be of electronic origin. The cut-off energy is about 13.2 keV, which is in good agreement with Eq. 2.12 taking a laser photon energy of 1.63 eV and an electron energy of 22.5 MeV. The detected X-ray bandwidth is $\sigma_{\text{rms}} = 0.53$ keV which is slightly more than the detector resolution limit.

Integrating the counts from the first to the eighth peak, with weights according to the pile-up order, and taking into account filter transmission, vacuum windows, air as well as the ratio between emission cone and detector solid angle, about 150 X-ray photons per shot were emitted from the source.

The spectrum has also been measured for electron energies of $\rho c = 23$ MeV, 26 MeV and 29 MeV. For each chosen energy, the final focusing triplet was adjusted in focusing strength for maximum signal to noise ratio. From the recorded histograms, the peak positions of the X-ray signal were determined in a range from about 10 – 20 keV. The transition of the X-ray peak energy varies with the Lorentz factor squared in good agreement with Eq. 2.12. A plot is shown in Fig. 4.20.

In the current setup, the tuning range is limited by several factors. For energies above 30 MeV, the permanent magnet triplet’s focusing strength is too weak. This results in a longer focal length so that the whole unit needs to be shifted away from the target plane. In our setup, we were limited by the length of the linear translation stage. For electron energies below 22 MeV, the triplet (designed for electrons with 24 MeV) is too strong and required shifting into the “exclusion-area” around the target plane defined by the position of optical components. It is important to emphasize that these setup changes, even though requiring a complete re-alignment through

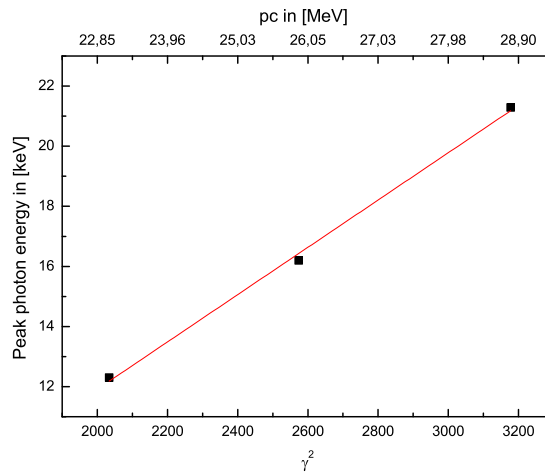


Figure 4.20: Linear X-Ray tuning range from 12 keV to 21 keV for electron energies $pc = 23$ MeV, 26 MeV and 29 MeV (Image from [40]).

the accelerator, were reliably done within less than two hours, and the production of X-rays could be called “turn-key” once the accelerator was set.

This was still true after a break of several days in between individual runs during the campaign with a total “Switch-On time” of about four hours. This included a complete start of both machines, laser and accelerator, from the off-state.

The measurements with the semiconductor detector were meant to optimize the setup and interaction conditions based on the fast readout/response to any parameter variation. Also, this type of detector is well established in the community of X-ray spectroscopy, and the data, even displaying low spatial and energy resolution, will be used to verify the data from the CCD camera.

5 HIGH RESOLUTION X-RAY SPECTROSCOPY ON AN ICS SOURCE

In the previous chapter, the results from the first light measurement were presented after achieving spatial and temporal overlap of the electron beam with the laser pulse. In this chapter, the influence of beam and laser parameters on the emitted radiation shall be investigated. To improve the spatial and energy resolution, an X-ray CCD camera replaced the previously used single element detector. The obtained spectra are subsequently compared to CLARA predictions to answer the crucial questions:

- What is the correlation of the electron (transverse emittance, energy) and laser (spectrum) parameters with the characteristics of the emitted X-ray radiation (energy-angle correlation, flux)?
- How accurate is the interaction process modeled in CLARA? Can this tool be used for future source design?

In order to reduce uncertainties during the analysis, it was important to precisely control the parameters of both interacting beams, most importantly: electron beam energy, laser wavelength and observation angle (see Eq. 2.12). The superconducting accelerator ELBE produces stable electron beams with a kinetic energy of 22.5 MeV.

The laser is located in a temperature stabilized cleanroom that minimizes spectral drifts within the time span of the measurements. The laser pulse energy ($E = 100$ mJ) and focal spot size ($35\mu\text{m}$ (FWHM)) is monitored to ensure a constant laser strength parameter $a_0 = 0.05$ for the linear regime. Because of the pixelated detector, no pile-up occurred, and the maximum total bunch charge of $Q_b = 77$ pC was used. As a consequence of the spot size ratio, this results in an effective interacting charge of $Q_{\text{eff}} = 1.2$ pC as explained in Section 4.4.

To gain insight into the interaction kinematics, a full data-set of energy spectra at various observation angles was collected. To illustrate the scanning direction and the path of the backscattered photons from the interaction point to the camera, the detector area from the setup illustration in Fig. 3.19 is shown (not in scale) in Fig. 5.1.

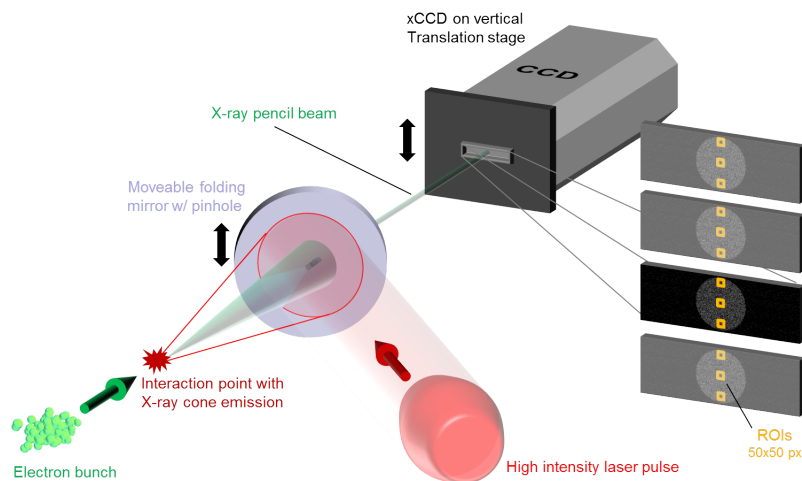


Figure 5.1: Schematic illustration of the X-ray propagation path to the detection system (not to scale). The deflection dipole magnet is not shown for better clarity. The magnet is located between the interaction point and the laser mirror.

The X-ray photons are emitted in a cone with full angle $2/\gamma$. They propagate towards the last laser folding mirror 1400 mm away from the source, where they are stopped within the 20 mm fused silica substrate. Only the photons that propagate through a

5 mm-diameter aperture in the mirror arrive at the CCD detector at 1915 mm distance. For every camera position, the flat laser folding mirror can independently be moved for maximum X-ray transmission onto the camera.

Within every camera image, “regions of interest” (ROIs) with dimensions 50 by 50 pixel (respectively 1.3 mm \times 1.3 mm) were defined (see illustration in Fig. 5.2). Only SPAEs inside those regions were analyzed, leading to an angular resolution of 0.67 mrad. In order to compare the experimentally determined spectrum to numerical simulations, this resolution is necessary to probe the evolution of the spectrum with increasing detection angle without significant spectral broadening because of the detector size [33]. The separation between the single ROIs is 1.15 mrad.

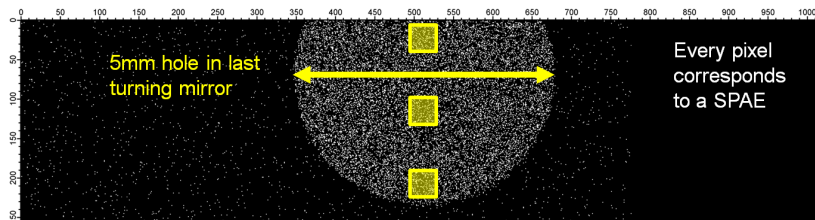


Figure 5.2: X-ray spot on the CCD with three defined regions of interest (ROI) after an integration of 900 shots.

In order to observe larger observation angles, the CCD camera was moved to four positions. With four camera positions, which cover an opening angle of $\sim 1/\gamma$ and three ROIs within every image, there are 12 histograms sampling the angular space. The angular resolution is up to now limited by the X-ray flux which results in low count rates at larger observation angles. The integration time was chosen based on the long-term stability of the laser spectrum and should not be further increased. With the same setup and beam parameters, the angular resolution can be increased by using circular ring shaped ROIs instead of squares, which cover the same or even larger area on the CCD chip. The analysis algorithms are currently updated to implement this procedure.

As seen in Subsection 3.3.2, the electron beam is asymmetric, and the width and divergence and all derived quantities have to be considered for the x- and y-axis separately. The camera was moved in the y-direction. The correlations between observation angle and beam angular spread are therefore limited to the y-z plane. It follows that in Fig. 3.26 the projection onto the y-axis with $\sigma_y = 115\mu\text{m}$ is relevant for the estimation of $\sigma_{\varphi,y}$ from Eq. 3.2. For asymmetric beams, the normalized transverse emittance has to be treated independently for the x- and y-direction.

Figure 4.15 in Section 4.3 represents the background signal for the whole CCD area. The background within a ROI scales with its size, which means that the data, presented in the following, is effectively background free.

5.1 PHOTON FLUX DISTRIBUTION

Figure 5.3 contains a full data-set for the angle-energy correlation studies of Thomson backscattering at PHOENIX. It shows the measured spectra for twelve observation angles with an energy bin width of 30 eV and an angular resolution of 0.67 mrad. One histogram is the result of the integration of 900 consecutive interactions between laser and electron beam. The channel numbers are already converted into energy based on the calibration as explained in Section 4.2. The histograms are corrected for the energy dependent quantum efficiency of the whole setup. The efficiency of the

SPAEC algorithm was determined to be 80% (not corrected in the histogram counts) [120].

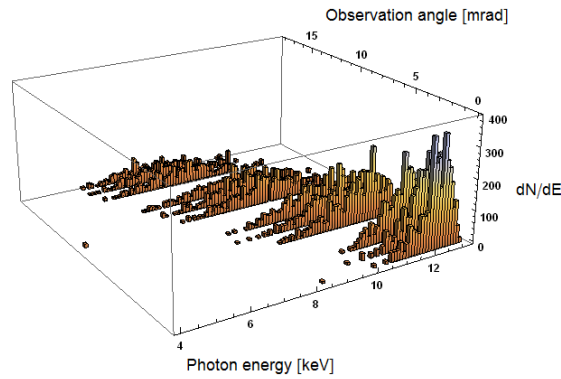


Figure 5.3: Histogram data for all camera positions and related regions of interest. For better visibility the histogram is binned.

The flux per ROI for the full spectral bandwidth was determined by integrating the histograms in Fig. 5.3. The result is shown in Fig. 5.4. The plot illustrates the decrease of the flux with increasing observation angle for the full bandwidth (black squares). Also shown is the prediction by the CLARA code (black curve). The curve re-samples the angular flux distribution similar to a moving aperture.

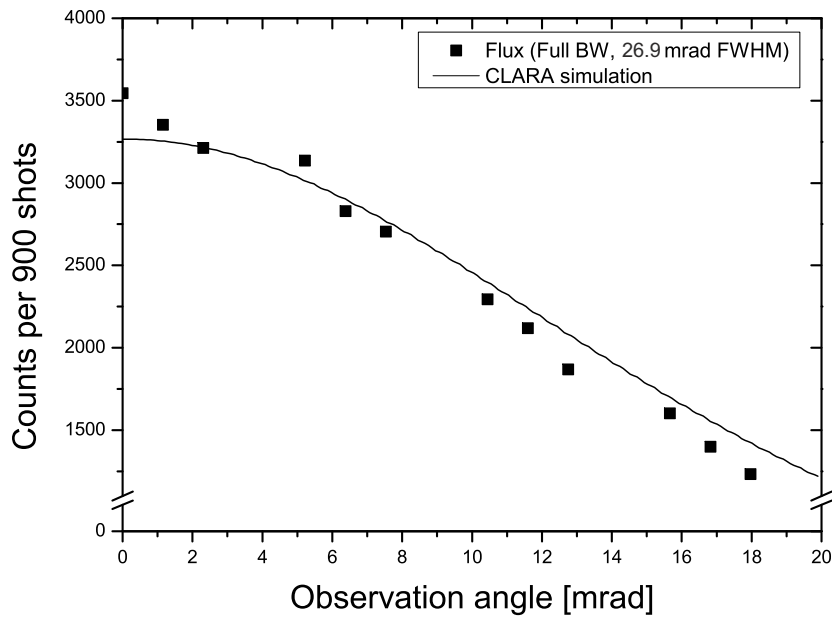


Figure 5.4: Photon flux in good agreement to simulation result. Integration of 900 consecutive scattering events per ROI. The photon flux is peak along the electron beam propagation axis.

The total flux angular distribution is peaked on the electron beam propagation axis. For the parameters used in the experiment, the full angular width is 26.9 mrad (FWHM). This is significantly less than the $2/\gamma$ -opening angle ≈ 44 mrad generally used to normalize measured flux quantities for comparison reasons.

Within the on-axis region of interest (ROI), corresponding to a solid angle of $0.46 \mu\text{sr}$, 13 photons per shot were detected with $Q_{\text{eff}} = 1.2 \text{ pC}$.

The number of emitted X-ray photons with the bandwidth $\Delta\omega/\omega$ depends linearly

on the electron bunch charge Q and the laser power P as stated in [19]

$$N_{\text{xray}} = 8.4 \times 10^{19} \frac{N_0 \lambda_0^2}{2\pi d_{\text{bunch}}^2} \cdot Q[\text{C}] \cdot P[\text{TW}] \cdot \left(\frac{\Delta\omega}{\omega} \right) \quad (5.1)$$

where N_0 is the number of oscillations during the interaction, λ_0 the laser wavelength and d_{bunch} is the electron bunch diameter.

The design parameters for the ELBE superconducting photo-gun include a maximum bunch charge of 1 nC [121]. With the available laser power of 150 TW from the DRACO-Ti:Sa laser system and under the assumption of an ideal beam overlap, the number of photons can be scaled to 1×10^5 photons per shot in a solid angle of $0.46 \mu\text{sr}$. This corresponds to a $600 \mu\text{m}$ X-ray spot 1 m away from the interaction point. The integration over the full emission cone would yield an X-ray photon flux of 1×10^8 photons per shot.

It had been suggested in previous publications that X-ray sources based on inverse Compton scattering can be tuned in photon energy and bandwidth by an aperture with variable diameter and position. The histograms in Fig. 5.3 obtained with an angular resolution of 0.6 mrad effectively represent the intrinsic bandwidth defined by the interacting beams, which cannot be reduced further by reducing the aperture diameter. Therefore, spectral filtering is required to reduce the bandwidth on-axis or even to maintain the “on-axis bandwidth” for observation angles $\theta > 0$.

As a consequence of the parameters accessible with today’s accelerators and lasers, the yield that is necessary for single-shot pump-probe experiments limits the energy and bandwidth tunability via the detection angle. Hence, it is even more important to understand the parameter influence on the spectral properties in order to fit the experimental needs on-axis without further alteration of the source spectrum.

5.2 MEASUREMENT OF THE ANGLE-ENERGY CORRELATION (AEC)

As derived in Subsection 2.1.1, for one relativistic electron ($v \approx c$) oscillating in a linearly polarized laser field (ω_0), the angular frequency of the scattered photon ω_{sc} is given by

$$\omega_{sc} = \frac{2\gamma^2 (1 - \cos \varphi)}{1 + (a_0^2/2) + \gamma^2 \theta^2} \omega_0,$$

where φ is the collision angle ($\varphi = 180^\circ$ for head-on geometry). For linear Thomson backscattering, it is required that the laser strength parameter a_0 is small ($a_0 \ll 1$). In this experiment, the angles are related to the laboratory frame, i.e. the emission/observation angle θ is measured with respect to the average electron propagation direction (beam axis). From Eq. 2.12, the maximum photon energy $E_{\text{max}} = 4\gamma^2 E_0$ directly follows that can be detected along the beam axis for head-on geometry. Any deviation in either collision or observation angle from a head-on geometry reduces the Doppler shift, resulting in lower photon energies.

The histograms in Fig. 5.3 are the result of numerous collision events between electrons and photons. For every single event, the equation above is valid. It is important to mention that the aforementioned beam axis is the average of all propagation directions. For an individual electron, the angle θ is related to its propagation direction and φ to its interaction angle with the laser photon. By placing a detector at a certain

position, the measured spectrum is an averaged result for many different scattering geometries.

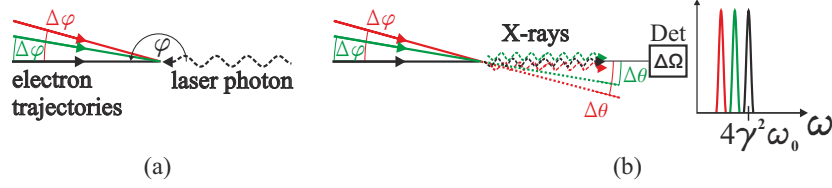


Figure 5.5: (a) Schematic of the interaction for head-on geometry ($\varphi = \pi$) including kinematic effects ($\Delta\varphi$) as well as detector size ($\Delta\Omega_{\text{Det}}$). (b) The detector is placed on the electron beam axis ($\theta = 0$). (Image from [122])

An ensemble of electrons in a bunch crosses the interaction plane at multiple angles relative to the beam axis owing to the beam's transverse emittance as sketched in Fig. 5.5(a). The electron direction deviation $\Delta\varphi$ has to be added to the observation angle and therefore causes an observation angle spread $\Delta\theta$ (Fig. 5.5(b)). Superposition of the emitted X-ray photons causes the detected X-ray spectrum to be broadened. For a detector placed at $\theta = 0$, these photons can only contribute to the low-energy tail of the spectral distribution ($\omega < 4\gamma^2\omega_0$). This effect, caused by the θ -dependence in Eq. 2.12, results in a skewed X-ray spectrum, assuming symmetric distributions of the electron beam energy and the laser bandwidth.

From the histogram images in Section 5.1, it is qualitatively apparent that the X-ray photon energy and bandwidth, as well as spectral shape, vary with the observation angle. The focus of the analysis is centered on the statistical moments of the photon distribution, namely center, width and skewness. By fitting a skewed Gaussian distribution function defined by [123]

$$f(x, x_0, Y, \Delta x) = Y \exp \left\{ -\ln 2 \left[\ln \left(1 + \frac{2b(x - x_0)}{\Delta x} \right) \frac{1}{b} \right]^2 \right\} \quad (5.2)$$

with the amplitude Y and abscissa shift x , these moments can be calculated much faster than by using Eq. 2.27 in its differential form. Analytical expressions for the distribution moments are of great value for analyzing data-sets with low count rates. Often the moments are underestimated because of the lack of data far away from the peak of the distribution. The asymmetry parameter b has a positive sign for skewed distributions in the direction $x > 0$ and negative sign for $x < 0$. A symmetric Gaussian function is represented by $b = 0$. The full width at half max value is related to Δx by

$$FWHM = \Delta x \frac{\sinh b}{b}$$

During the fitting process, the logarithm in Eq. 5.2 may become undefined. This happens for $x \leq x_0 - \frac{\Delta x}{2b}$ and positive skew or $x \geq x_0 - \frac{\Delta x}{2b}$ and negative skew. The height of the distribution function, when approaching these values x_{Limit} , is negligibly small. Hence, the fitting function $f(x, x_0, Y, \Delta x)$ used during the further analysis was defined piecewise with

$$f(x, x_0, Y, \Delta x) = \begin{cases} Y \exp \left\{ -\ln 2 \left[\ln \left(1 + \frac{2b(x-x_0)}{\Delta x} \right) \frac{1}{b} \right]^2 \right\} & \\ 0 & \text{if } x \leq x_0 - \frac{\Delta x}{2b} \text{ and } b > 0 \\ 0 & \text{if } x \geq x_0 - \frac{\Delta x}{2b} \text{ and } b < 0 \end{cases} \quad (5.3)$$

Figure 5.6 shows examples of three histograms at different observation angles $\theta = 1.15$ mrad, $\theta = 5.22$ mrad and $\theta = 15.66$ mrad. The plots also include the fit function $f(x, x_0, Y, \Delta x)$ as described above. They show the expected behavior with the energy shifting to lower values while the bandwidth increases and the spectra become more symmetric with increasing angle.

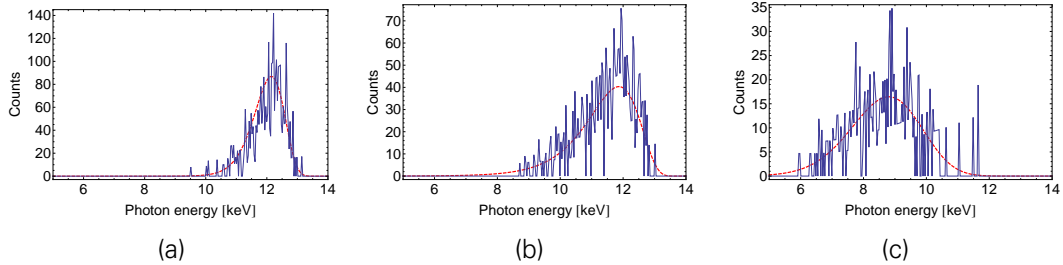


Figure 5.6: Measured X-ray spectra and Eq. 5.2-fit at various observation angles $\theta =$ (a)1.15 mrad, (b)5.22 mrad, (c)15.66 mrad.

The fit results for all observation angles are plotted in Fig. 5.7. The spectrum peaks at 12.3 keV on the axis ($\theta = 0$) and shifts to 8.2 keV at $\theta = 18.0$ mrad. The measured maximum cut-off energy, which results from a head-on collision of an electron with a photon from the blue end of the laser spectrum, is 13.2 keV. This is in good agreement with the prediction from Eq. 2.12, taking a laser photon energy of 1.63 eV and an electron kinetic energy of 22.5 MeV. The position of the X-rays peaks are found to deviate from Eq. 2.12, particularly near the electron beam propagation axis. This is because of the angular spread of the incoming electrons, which destroys the simple correlation between scattered photon energy and observation direction in Eq. 2.12.

Values from skewed gaussian fits

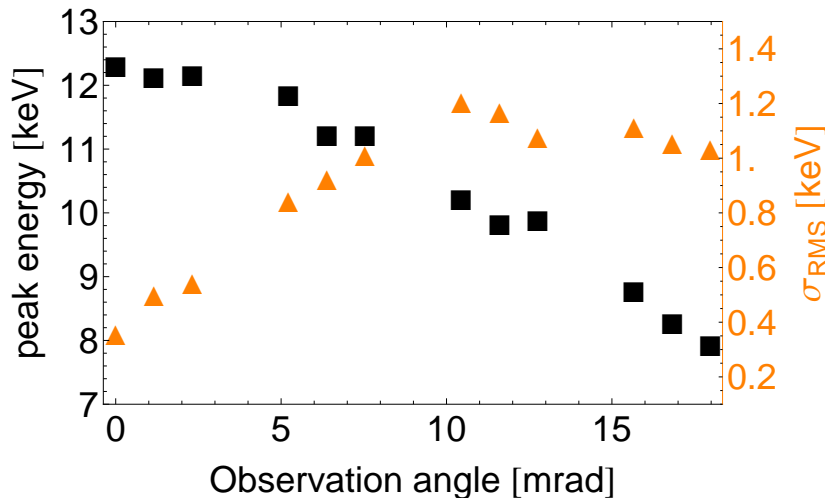


Figure 5.7: Peak energy and bandwidth according to Eq. 5.2 for all sampled observation angles.

At $\theta = 0$, the electron beam angular spread results in X-rays that only contribute to the low energy part of the spectrum. At larger angles the correlation between X-ray photon energy and observation angle is smeared out completely, leading to symmetric histograms with the peak/average energy agreeing with Eq. 2.12 for the single electron and tails to both ends of the spectrum (see Fig. 5.6(c)).

The bandwidth, therefore, is minimal on axis, where the broadening due to the angular spread is asymmetric. It grows with increasing observation angle before saturating at about $\theta \approx 10$ mrad for our experimental conditions.

5.3 DEPENDENCE OF THE ANGLE-ENERGY CORRELATION ON THE ELECTRON BEAM ENERGY

The experimental measurements were supported by numerical calculations with the CLARA code to estimate the influence of certain parameters on the emitted radiation. For a direct comparison, the simulation output was sampled at the same angles as the measurement data and Eq. 5.2 was employed as the fitting function, as explained in the previous section. An example of this is shown in Fig. 5.8 for a simulation result of an electron beam with 22.5 MeV kinetic energy and a normalized transverse emittance of 7π mm mrad. The spectral intensity as a function of photon energy and observation angle is normalized to the on-axis maximum value.

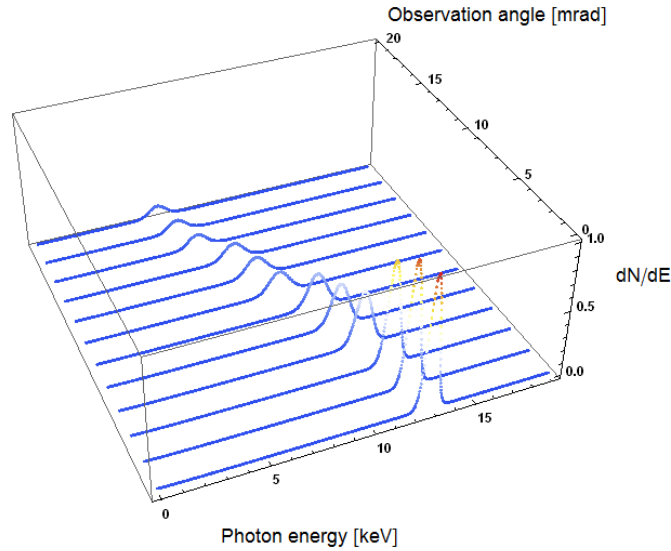


Figure 5.8: CLARA simulation result for the emitted radiation. GPT traces of 5×10^4 electrons were used in the simulation of the interaction to avoid numerical noise problems.

In order to study the dependence of the emitted spectrum on a change of the electron beam energy, simulations of the scattering process with different electron beam energies were performed. In a second set of simulations, the transverse emittance was varied at a fixed electron kinetic energy of 22.5 MeV. The comparison of both simulations revealed characteristic changes of the emitted spectra for changes of either electron beam energy or beam emittance.

Figure 5.9 illustrates the spectral peak position for both simulation sets together with the experimental data.

Figure 5.9a contains the first simulation set results for electron kinetic energies of 21.5 MeV, 22.5 MeV and 23.5 MeV with a normalized transverse emittance of 16π mm mrad. Depending on the electron energy, the spectrum experiences a vertical shift (photon energy axis), where the larger the absolute γ -dependent photon energy deviation is the flatter the angle-energy curve is, with the maximum deviation on the electron beam propagation axis. The sensitivity to a change of the kinetic energy is well below 1 MeV absolute or 5% relative deviation.

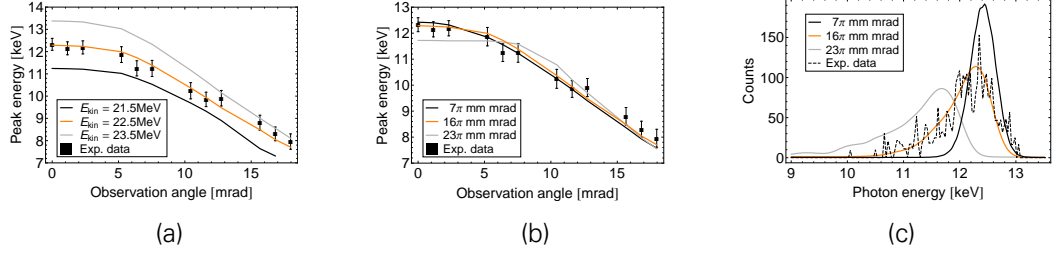


Figure 5.9: CLARA simulation for various beam energies (a) or transverse emittances (b). (c) Histograms of the measured data and simulations for transverse emittances of 7π mm mrad, 16π mm mrad and 23π mm mrad at $\theta = 0$ for a kinetic energy of 22.5 MeV.

The variation of the emitted spectra because of a change of the transverse emittance for a fixed kinetic energy of 23 MeV is illustrated in Fig. 5.9b. On the electron beam propagation axis, the peak energy varies with the beam divergence of the electrons defined by $\epsilon/\gamma\sigma_r$. As expected from the description in Section 5.2, the photon peak energy at larger observation angles ($\gtrsim 10$ mrad in our experimental setup) is effectively independent from the beam emittance/divergence. At small observation angles ($\lesssim 10$ mrad), the beam divergence changes the shape of the spectrum, as shown for $\theta = 0$ in Fig. 5.9c. With more divergent electron beams, the spectrum is asymmetrically broadened, leading to skewed photon distribution with a tail towards the low energy side. A laminar beam, a beam with no angular spread, would result in an angle-energy curve described by the undulator equation in Eq. 2.12. Emittance is responsible for the specific curve shape such as width and skewness of the distributions.

Because of the independence of the X-ray spectra from the transverse emittance at larger angles, resulting in a vanishing skewness, these data points can be used to deduce the electron beam kinetic energy. In Section 5.2, it was explained that the peak values for symmetric X-ray distributions agree with Eq. 2.12.

Following this argumentation, the electron beam energy can be deduced by fitting Eq. 2.12 to the peak positions of the experimental data, allowing only large observation angles with unskewed spectra. The result of such a fit is shown in Fig. 5.10 with the expected deviation for $\theta \rightarrow 0$. As a reminder: Eq. 2.12 describes a single electron interaction and does not include collective effects like emittance that lead to skewness and different angle-energy curves.

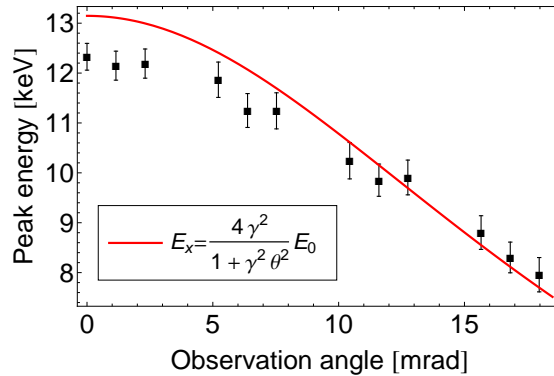


Figure 5.10: Determination of the electron beam energy via Eq. 2.12.

The fit result of the electron beam kinetic energy of $E_{\text{kin}} = 23.4$ MeV is within 5% of the ELBE machine parameter of $E_{\text{kin}} = 22.5$ MeV. It is important to keep in mind

that the selection of data which is used during the fitting process is very important and needs to be based on the skewness of the photon distribution. The angle from where the spectra are symmetric depends on the electron beam parameters and the interaction geometry. Alternatively one could use the high energy cut-off of the X-ray spectrum at $\theta = 0$ to determine the electron beam energy. The weakness of this method is that it relies on a single observation angle and the determination of the cut-off energy can be difficult if there is a small signal to noise ratio. Additionally if the spectra are broadened due to electron beam energy spread or laser bandwidth the cut-off energy is not directly related to the electron beam mean energy anymore.

5.4 DEPENDENCE OF THE ANGLE-ENERGY CORRELATION ON THE LASER SPECTRUM

Figure 5.7 shows the change of the X-ray bandwidth with increasing observation angle. The minimal value, which is found on the electron beam propagation axis, reads $\Delta\lambda_{\text{xray}} = 0.36$ keV (RMS), or $\Delta\omega/\omega = 4.5\%$ (RMS).

A finite bandwidth of a Thomson scattering X-ray source results from the complex interplay between electron energy spread ($\Delta\gamma$), electron beam emittance ($\propto \Delta\varphi^1$), laser focusing geometry ($\Delta k \propto \Delta\varphi$), laser bandwidth ($\Delta\omega_0$) and detector solid angle ($\Delta\Omega_{\text{Det}}$) as described by Eq. 2.24.

The influence of the laser wavefront curvature on the X-ray bandwidth because of the focusing geometry was estimated by [24]

$$\frac{\Delta\omega}{\omega} \sim \frac{\gamma^2}{1 + a_0^2/2} \left(\frac{\pi d_{\text{laser}}}{L_{\text{int}}/2 + z_0^2/(2/L_{\text{int}})} \right)^2 \quad (5.4)$$

where γ and a_0 are the electron Lorentz factor and the laser interaction strength, L_{int} is the interaction length from Eq. 4.2 and z_0 is the laser Rayleigh length.

When $L_{\text{int}} \ll z_0$ as is the case when using a short pulse laser, the electrons interact with a flat laser wave-front.

In this experiment, the influence of laser focusing was suppressed by using a long focal length parabola ($f/30$).

Giving the experimental parameters: $\gamma = 45.1$, $a_0 = 0.05$, $d_{\text{laser}} = 15\mu\text{m}$ (RMS), $L_{\text{int}} = 0.3$ mm and $z_0 = 3.5$ mm, the estimated broadening is about 6×10^{-4} . This is much smaller than the measured X-ray bandwidth ($\Delta\omega/\omega = 4.5\%$). Therefore, it can be concluded that the laser wave-front curvature has a negligible effect on the X-ray spectrum in this experiment.

The electron beam energy spread illustrated in Fig. 3.11 is $\Delta\gamma/\gamma = 0.001$ (RMS), hence negligible for further considerations.

Because of the finite detector size, it collects scattered X-ray photons emitted in a certain solid angle, thereby increasing the detected X-ray bandwidth ($\sim \gamma^2 \Delta\Omega_{\text{Det}}^2$) [46, 51, 124]. By choosing a ROI-size corresponding to a solid angle $\Omega_{\text{Det}} = 0.46 \mu\text{sr}$, the effect of the finite detector size may be made immeasurably small ($\Delta\omega/\omega < 10^{-10}$). Therefore, Eq. 2.24 reduces to

$$\frac{\Delta\omega}{\omega} \approx \sqrt{\left(\frac{\Delta\omega}{\omega}\right)_{\lambda}^2 + \left(\frac{\Delta\omega}{\omega}\right)_{\epsilon}^2} \quad (5.5)$$

In comparison to other inverse Compton scattering light sources [26, 28, 30, 31,

¹ φ from Eq. 2.12

33, 55, 125, 126], the PHOENIX X-ray source is based on a short-pulse high-intensity Ti:Sapphire laser system. The main motivation for this approach is that this laser system can produce pulse energies up to several joules on target in a small focal spot in order to explore the kinematics of the interaction in the highly nonlinear scattering regime ($a_0 \geq 1$).

Another aspect of the PHOENIX–DRACO setup is the future possibility to resonantly drive a plasma density wave to accelerate electrons from the plasma background to relativistic energies. This process, which is called laser wakefield acceleration, requires femtosecond laser pulses matched to the plasma frequency. The bunch duration of these electrons was recently measured [127] to be shorter than 10 fs. The pulse duration of inverse Compton scattering sources driven by a laser wakefield accelerated electron beam would be greatly reduced, which directly translates to the temporal resolution in a subsequent pump-probe experiment.

A femtosecond laser pulse intrinsically has a broad bandwidth, in the case of DRACO: $\Delta\lambda = 60$ nm or $\Delta\omega_0/\omega_0 = 2.5\%$ (RMS), which is a major contribution to the bandwidth according to Eq. 5.5.

Depending on the initial setup during the laser warm-up process, the spectrum of the laser can vary from a top hat shape to slightly asymmetric distributions toward the blue or red spectral range as shown in Fig. 5.11.

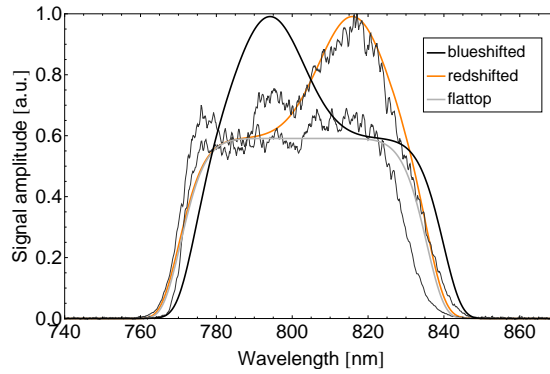


Figure 5.11: Possible spectra caused by thermal drifts in the laser amplifier chain during the experimental run together with their implementation functions for the simulation in CLARA.

To determine the influence of the laser spectrum shape, CLARA simulations, using the three laser spectrum models, shown in Fig. 5.11, were performed. All three spectrum models have identical mean and bandwidth.

The X-ray photon distributions, as the result of a convolution of the laser spectrum with the other parameter distributions, will differ from a simple continuous Gaussian distribution, skewed or not skewed, in the case of a measured laser spectrum as shown in Fig. 5.11.

The histograms are characterized in the following by the general statistical moments: mean μ , standard deviation σ and skewness α_3 defined by

$$\begin{aligned}\mu &= \int x f(x) dx \\ \sigma^2 &= \int (x - \mu)^2 f(x) dx \\ \alpha_3 &= \int \frac{(x - \mu)^3}{\sigma^3} f(x) dx\end{aligned}\tag{5.6}$$

where $f(x)$ is the probability density function or normalized amplitude for each x bin with $\int_{-\infty}^{\infty} f(x) dx = 1$. Note that here, μ is not the peak energy but the mean of the photon distribution.

From Eq. 5.6 follow the definitions for a 1σ -confidence interval for σ and α_3 [128]

$$\Delta\sigma = \frac{\sigma}{2(\sum_i n_i)} \left(\sum_i n_i \left[\frac{(i-\mu)^2}{\sigma^2} - 1 \right]^2 \right)^{1/2} \quad (5.7)$$

$$\Delta\alpha_3 = \frac{1}{(\sum_i n_i)} \left(\sum_i n_i \left[\frac{(i-\mu)^3}{\sigma^3} - \frac{3\alpha_3}{2} \frac{(i-\mu)^2}{\sigma^2} + \frac{\alpha_3}{2} \right]^2 \right)^{1/2}$$

after the transition from a continuous probability density function $f(x)$ to a discrete form n_i .

Taking a fixed spot size of $\sigma_r = 140\mu\text{m}$, the CLARA code was used to simulate the scattering interaction using a transverse emittance of 20π mm mrad and an electron kinetic energy of 22.5 MeV. The ratio of electron beam focal spot size and transverse emittance in this simulation corresponds to the same electron beam angular spread at the interaction plane as the experimental parameters of $\sigma_\gamma = 115\mu\text{m}$ and 16π mm mrad. The simulation results are illustrated in Fig. 5.12.

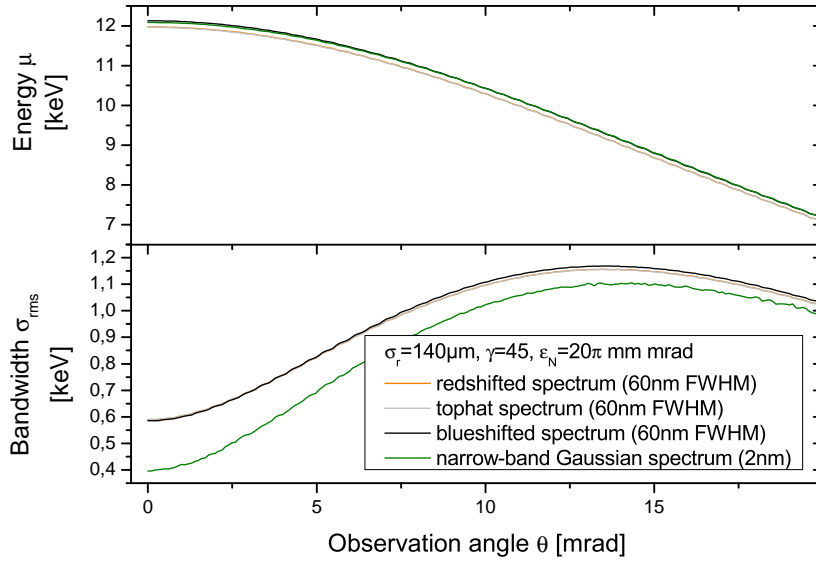


Figure 5.12: Mean energy and bandwidth of the backscattered X-rays for broad laser spectra with various spectral distribution shapes.

In both cases, for mean energy and bandwidth, the difference of the observation angle dependent curves is well below a 1σ -error bar for each individual curve. Figure 5.12 also contains the simulation result for the interaction with a narrow-band laser of 2 nm spectral width to show the influence of the laser spectral width. The X-ray spectrum is narrow because of the reduced bandwidth of the laser with the biggest difference (compared to the broadband laser interaction) on the electron beam axis. For larger observation angles the smearing effects related to the electron beam angular spread dominate. If the bandwidth of the laser is on the order of a few percent, the emitted radiation is significantly broadened and effectively independent from the specific spectral shape of the laser.

5.5 DEPENDENCE OF THE ANGLE-ENERGY CORRELATION ON THE ELECTRON BEAM ANGULAR SPREAD

The peak energy at small observation angles ($\lesssim 10$ mrad) depends on the beam transverse emittance as seen in Fig. 5.9b.

The on-axis ($\theta = 0$) mean photon energy $\langle \omega_{\text{SC}} \rangle$ can be estimated by averaging ω_{SC} from Eq. 2.12 over a distribution $f(\varphi)$ of collision angles φ , using a monochromatic plane wave approximation for the laser electric field². The integral $\langle \omega_{\text{SC}} \rangle = \int d\varphi f(\varphi) \omega_{\text{SC}}(\varphi)$ can be solved by expanding ω_{SC} in powers of the angle φ with $\Delta\varphi = \sigma_\varphi = \epsilon_n / (\gamma\sigma_r)$ leading to

$$\langle \omega_{\text{SC}} \rangle_{\theta=0} \approx 4\gamma^2 \omega_0 \left(1 - 2(\gamma\Delta\varphi)^2 \right). \quad (5.8)$$

A comparison of this analytic scaling to the full-physics 3D numerical result from the CLARA code is presented in Fig. 5.13.

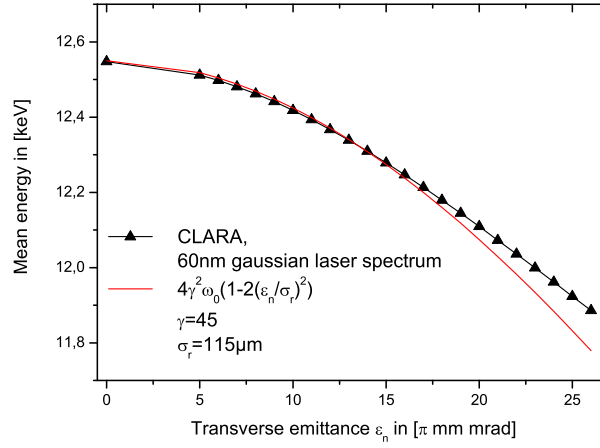


Figure 5.13: Mean energy from Eq. 2.12 as a function of the transverse emittance of the electron beam on the beam axis ($\theta = 0$).

The difference of $\langle \omega_{\text{SC}} \rangle$ from Eq. 5.8 and CLARA in the experimentally accessible parameter space is about 1%, which is below the detector resolution in the setup used. The approximation in Eq. 5.8 can be used for the prediction of the X-ray mean energy in most experimental scenarios as seen in Fig. 5.13.

As explained in Section 5.4 the X-ray bandwidth ($\Delta\omega/\omega$) scales with the electron beam emittance ($\sim \gamma^2 \Delta\varphi^2$), which causes an asymmetric broadening of the emitted radiation near the electron beam axis ($\lesssim 10$ mrad) and couples the parameters collision angle φ and observation angle θ in Eq. 2.12 (see Section 5.2).

In a plane-wave approximation of the laser for head-on interaction ($\varphi = 180^\circ$), assuming a small angular spread of the electron beam, the emittance-dependent contribution to the X-ray spectral broadening can be estimated for on-axis observation ($\theta = 0$). If the interaction occurs at the focal plane of the electron beam, $\Delta\varphi$ can be approximated by σ_φ from Eq. 3.2 leading to

$$(\Delta\omega/\omega)_{\text{emit}} \approx \gamma^2 \Delta\varphi^2 \approx \left(\frac{\epsilon_N}{\sigma_Y} \right)^2 \quad (5.9)$$

for the emittance contribution.

²A detailed derivation is presented in the Appendix section.

With Eq. 2.25 and the conclusions from the previous section which lead to Eq. 5.5, this results in

$$\Delta\omega/\omega \approx \sqrt{\left(\frac{\Delta\omega_0}{\omega_0}\right)^2 + \left(\frac{\epsilon_N}{\sigma_Y}\right)^4} \quad (5.10)$$

for the total bandwidth estimation on axis.

Inserting the measured values for the transverse emittance $\epsilon_N = 16\pi$ mm mrad, focal spot $\sigma_Y = 115\mu\text{m}$ and laser bandwidth $\Delta\omega_0/\omega_0 = 0.025$ in Eq. 5.10 yields an X-ray bandwidth of $\Delta\omega/\omega = 0.032$, corresponding to 0.39 keV at 12.3 keV peak energy.

This is in good agreement with the measured bandwidth in Fig. 5.7 ($\Delta\omega_{\text{rms}} = 0.36$ keV) where a skewed Gaussian distribution (Eq. 5.2) was used to deduce the bandwidth from the measured X-ray histograms.

The beam angular spread changes the general shape of the angle-dependent histograms in terms of peak/mean energy, bandwidth and skewness. There are no general analytic expressions for the bandwidth of the emitted radiation away from the electron beam axis.

The influence of the transverse emittance or electron beam angular spread on the X-ray radiation at all observation angles has been extensively studied using CLARA simulations. The results of four different examples of angular spreads are depicted in Fig. 5.14. The numerical predictions from the CLARA code are shown as quasi-continuous spectral intensity color maps with an angular resolution of 0.1 mrad and an energy resolution of 0.01 keV. This is more than one order higher than the energy resolution of the X-ray detector and five times higher than the experimentally achieved angular resolution. Common to all simulations is the electron beam spot size of $\sigma_r = 140\mu\text{m}$ and the electron beam kinetic energy $E_{\text{kin}} = 22.5$ MeV.

With increasing electron beam angular spread or transverse emittance, the on-axis spectrum peak shifts to lower photon energies (red-shift). The X-ray bandwidth and the on-axis skewness value are proportional to the beam divergence and increase from Fig. 5.14 (a) to (d). The least angle for which the distributions are entirely smeared out leading to a negligible skewness, is approximately constant at $\theta \approx 10$ mrad.

Characterizing the X-ray spectra with a fit of Eq. 5.2 requires (skewed) Gaussian-like X-ray spectral distributions, which is not necessarily the case with laser spectra as seen in Fig. 5.11. For this reason, the first moments: mean μ , standard deviation σ and skewness α_3 from Eq. 5.6 are used again for the subsequent analysis.

The quality of the experimental data, being effectively background free, and the high angular resolution allow the entire data set (350 histogram bins at 12 detector positions) to be used, instead of only the on-axis data point, in order to cross-check the simulation results and to determine the spectral sensitivity of an inverse Compton scattering based transverse emittance measurement.

The sensitivity to the spectral shape and bandwidth can be used to deduce the electron beam angular spread by comparing simulation results of various transverse emittances from 10π mm mrad to 31π mm mrad at a fixed spot size of $140\mu\text{m}$ with experimental data using a maximum-likelihood analysis. Every bin is treated as a single counting-experiment and the expectation value is given by the CLARA prediction. Following Baker and Cousins [129], a Poisson likelihood chi-square χ_p^2 can be defined by

$$\chi_p^2 = 2 \sum_i y_i - n_i + n_i \ln \left(\frac{n_i}{y_i} \right) \quad (5.11)$$

with the prediction/model-vector $\mathbf{y} = (y_1, y_2, y_3 \dots y_k)$ and the the estimate-vector $\mathbf{n} =$

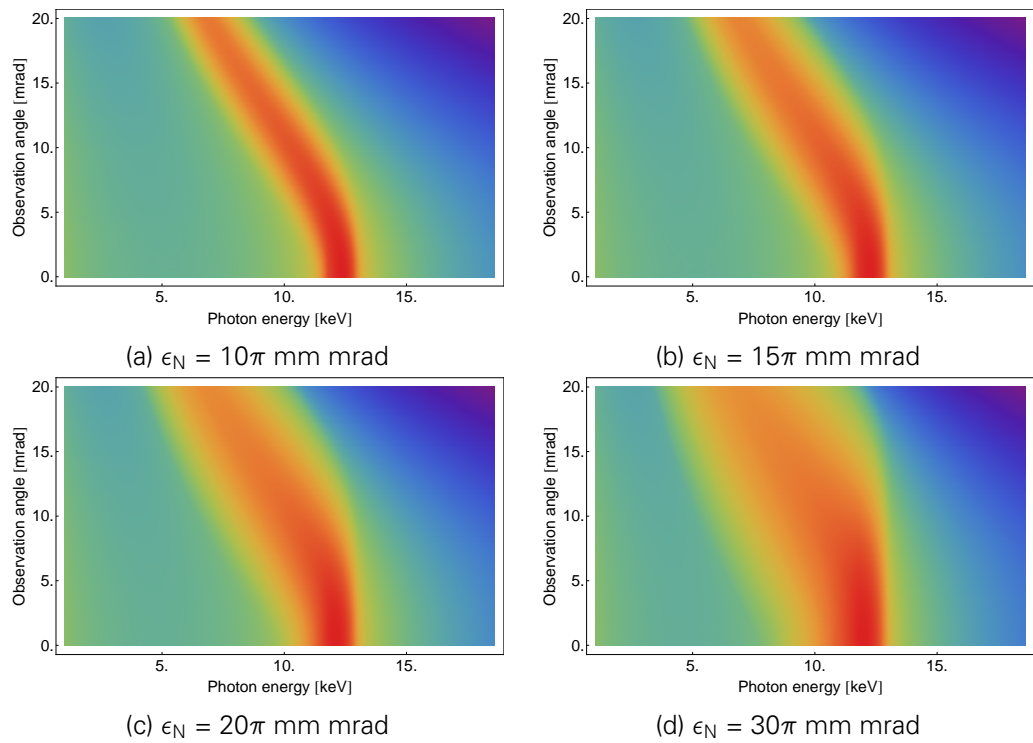


Figure 5.14: CLARA simulation results of the spectral intensity for various beam divergences. The simulation has an angular resolution of 0.01 mrad and an energy resolution of 0.01 keV. Common to all simulations is the electron beam spot size of $\sigma_r = 140\mu\text{m}$ and the electron beam energy $p c = 23$ MeV. The intensity color coding uses a logarithmic function.

$(n_1, n_2, n_3 \dots n_k)$, built from the raw data.

Before the analysis begins, 12 lineouts from the 2D intensity color map are selected at the θ -values of the experimental data points. In the following, these 12 histograms are re-sampled so the energy axis is identical to the experimental energy axis, meaning that two bins at position x_i relate to the same energy. In a next step, the quantum efficiency from Fig. 4.12 for the whole setup is applied. As the last step to build the prediction/model-vector \mathbf{y} , an average background signal had to be extracted from the experimental results. For this reason, the counts in 100 bins far away from the signal peaks were summed up over all observation angles and averaged yielding an average background signal per bin of 0.076, which is then added to all simulation results after the QE correction. The simulation results are normalized to 1 for the on-axis peak. A free parameter for the amplitude was therefore used to scale the simulation flux to the experiment.

With the estimate-vector \mathbf{n} , built from the raw data signal before any correction, two special cases of Eq. 5.11 have to be considered. If the model predicts zero counts in bin x_i , then the term inside the logarithm is not defined (division by zero). By adding a constant background amplitude, this case does not occur here, unlike the second case when the experiment signal n_i was zero in bin x_i leading to “ $0 \cdot \infty$ ” for the second addend in the summation over i . These cases were identified and their contribution to χ_p^2 was set to $2y_i$.

Several models were tested for different laser spectral shapes, electron beam energy and electron beam divergence. The overall minimal χ_p^2 was found for a slightly red-shifted laser spectrum (black curve in Fig. 5.11), an electron beam with 23 MeV kinetic energy and an emittance of 21π mm mrad for a spot size of $\sigma_r = 140\mu\text{m}$. The reduced chi-square is

$$\chi_{p,\text{red}}^2 = \frac{\chi_p^2}{\text{Degrees of freedom}} = \frac{\chi_p^2}{N - P} = 0.77 \quad (5.12)$$

taking 350 bins at 12 different angles with the parameters: amplitude A and angular spread σ_φ . This could be an indicator that the experimental noise is still underestimated by the numerical model.

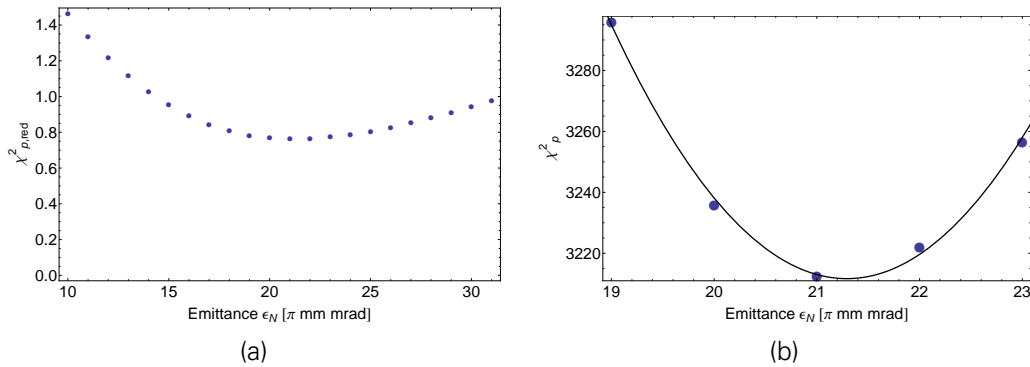


Figure 5.15: (a) $\chi_{p,\text{red}}^2$ with respect to the transverse normalized emittance. (b) Parabolic fit near the minimum to determine the electron beam angular divergence.

Figure 5.15a shows the trend of $\chi_{p,\text{red}}^2$ with respect to the transverse normalized emittance. Near the minimum, a quadratic fit yields the local minimum at $\epsilon_{N\gamma} = (21.29 \pm 0.25)$ mm mrad. This value has to be interpreted as a beam divergence of $\sigma_{\varphi\gamma} = (3.34 \pm 0.05)$ mrad, given a fixed spot size of $140\mu\text{m}$.

At the focus, the electron beam transverse emittance is correlated to the angular spread via Eq. 3.2. With the measured quantities $\gamma = 45 \pm 0.25\%$ and $\sigma_\gamma =$

$(115 \pm 6) \mu\text{m}$, a normalized emittance of $\epsilon_{\text{ny}} = (17.48 \pm 1.22) \text{ mm mrad}$ can be deduced. The result agrees very well with the machine parameters (see Subsection 3.1.3), the uncertainty of about 7% is dominated by the spot size measurement.

Using the definitions from Eq. 5.6, as well as Eq. 5.7, for the mean, the bandwidth and the skewness, the simulation yielding the least χ^2 -value can be quantitatively compared to the measured data as shown in Fig. 5.16. There is a good agreement of the numerical predictions and the experimental data within a $\pm 1\sigma$ -error bar.

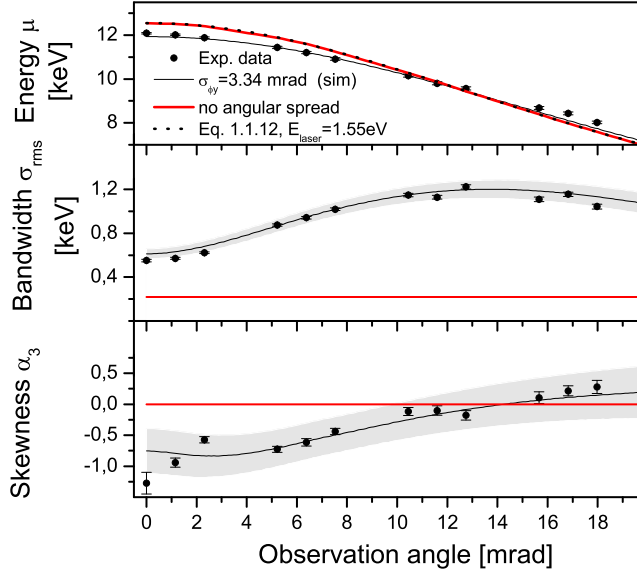


Figure 5.16: Comparison of measured data (black markers) with CLARA simulation (black curve) within a 95% confidence interval (shaded area) for the quantities bandwidth and skewness. The red line illustrates the CLARA simulation of a laminar beam ($\sigma_{\varphi} = 0$). (Image from [122])

The red line in Fig. 5.16 represents the case of a laminar electron beam ($\sigma_{\varphi} = 0$) interacting with a Gaussian laser spectrum with $\Delta\omega_0/\omega_0 = 2.5\%$ (rms). The bandwidth is a result of the short pulse (high bandwidth) laser used in the simulation. As expected, the histograms are symmetric at all angles, expressed by a vanishing skewness α_3 .

The influence of the angular spread ($\sim (\epsilon/\sigma_r)$) on the spectral parameters is presented in Fig. 5.17 over a broad span of transverse emittances. Other simulation parameters such as beam energy, spot size or laser spectrum were kept the same during this comparison. The angular distribution of electrons has a strong influence on the Thomson X-ray energy, spectral shape and bandwidth. Controlling this spread (the ratio of beam emittance and spot size) is necessary in designing future inverse Compton X-ray sources. The necessary steps towards pump-probe experiments with an ICS probe beam will be explained in the next chapter.

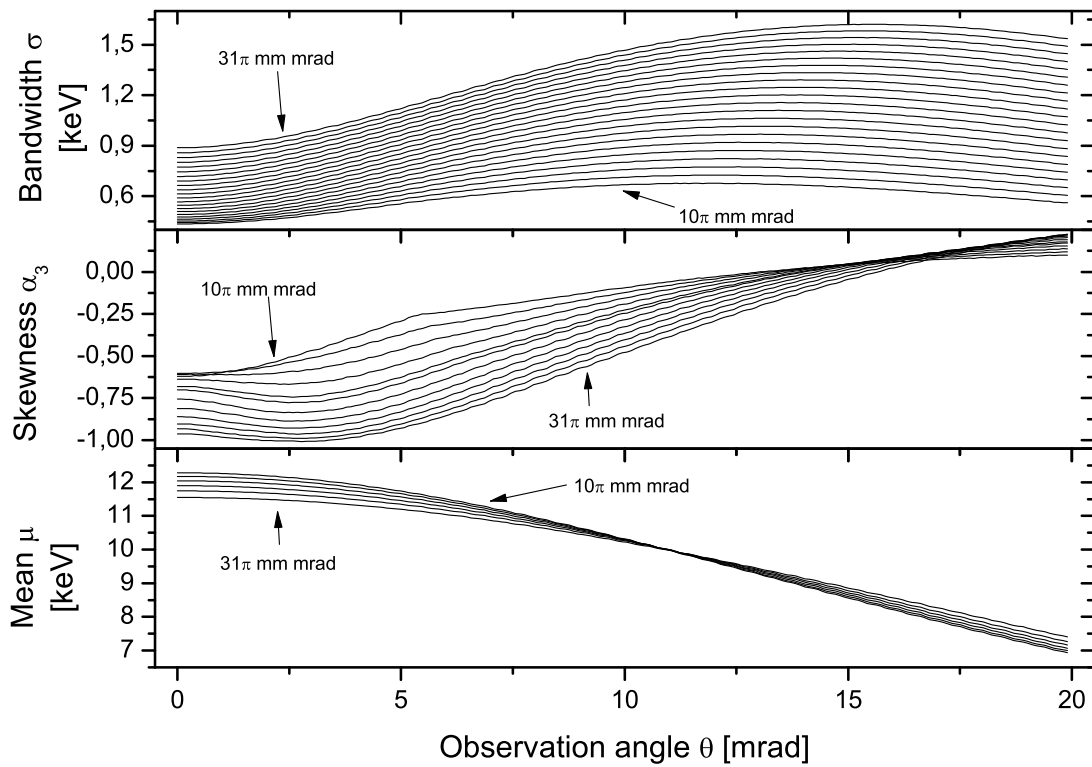


Figure 5.17: Summary of various CLARA simulations in terms of mean energy, bandwidth and skewness.

6 CONCLUSION AND OUTLOOK

In order to understand the kinematics during the interaction of the electron beam with the laser pulse certain tools were developed. Among those are, for instance, a numerical radiation code for a predictive analysis as well as a setup with high spatial and high energy resolution for X-ray spectroscopy. They were used to deduce beam parameters like the local angular spread or the beam kinetic energy. These techniques can easily be adapted to transverse and longitudinal slice emittance measurements of an electron beam by altering the laser focal geometry. The achieved quality for the source prediction so far is summarized in Fig. 6.1.

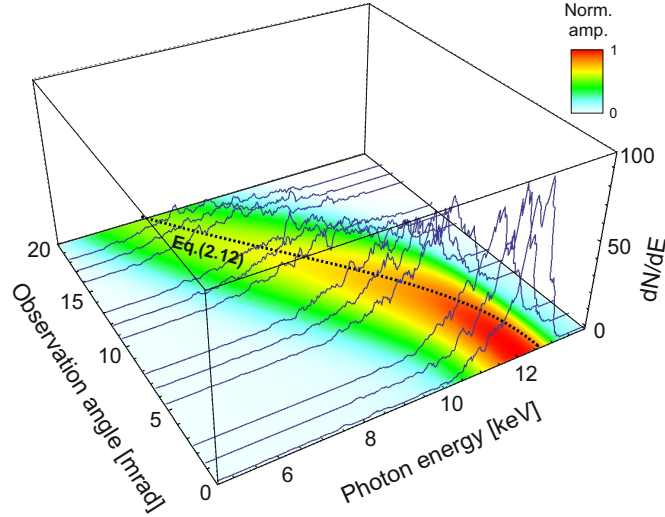


Figure 6.1: Normalized colormap of the predicted spectral intensity combined with the measured spectra from the PHOENIX ICS source using an electron beam at $\gamma = 45$ in head-on geometry [122].

The figure contains the measured histograms at various probed observation angles. Underlying the histograms is a colormap of the spectral intensity from a CLARA simulation with the electron and laser parameters from the experiment. The necessary sensitivity during the analysis is in turn essential to enable making a prediction on the emitted X-ray radiation based on the interaction parameters. The angular distribution of electrons has a strong influence on the Thomson X-ray spectral shape and bandwidth. Controlling this spread (the ratio of beam emittance and spot size) is necessary for designing Thomson X-ray sources with a specific bandwidth suited to an application.

In order to use PHOENIX for pump-probe experiments, the number of photons per pulse needs to be increased. The currently low photon flux is caused by the small amount of interacting charge. With the commissioning of the next generation SRF-gun cavities, bunch charges up to 1 nC will be feasible with a normalized transverse emittance below 2π mm mrad. This combination will lead to a matched laser/electron focal spot where the interaction charge equals the total bunch charge. With the full laser pulse energy available from the DRACO Ti:Sapphire laser, an X-ray yield of 1×10^8 photons per shot within 1.6π msr ($\sim 1/\gamma$), or 1×10^5 photons per shot with $\Delta\omega/\omega = 4.5\%$ (RMS) in a solid angle of 0.36π μ sr (corresponding to a 600 μ m X-ray spot 1 m away from the interaction point), is predicted. This will make PHOENIX a competitive X-ray source with finite bandwidth well suited for many types of time-resolved measurements in the sub-picosecond regime. In the future, the brightness of Laser-Thomson light sources can be further increased by employing the traveling wave Thomson scattering scheme [58] where the interaction length is increased by orders of magnitude.

Already, with a photon flux of 1×10^8 photons per shot in a broadband X-ray beam (also called pink beam), high energy density physics (HEDP) experiments are feasible. The shift of a K-absorption edge (see simulation results in Fig. 6.2) in a laser-heated copper foil will be one of the first experiments addressed with the PHOENIX X-ray source [130]. The laser, with its inhomogeneous intensity profile, will create matter at different temperatures within its focus. Because of the ultra-short nature of the driving laser pulses, the so heated matter will not reach an equilibrium state during the duration of the laser pulse. The sample is probed with a pink X-ray beam in combination with a pixelated detector (X-ray CCD camera) to record a space-averaged spectrum. With defined region of interests, one can analyze the local absorption edge shift and correlate this to a local plasma temperature as a result of the local laser intensity. The measured bandwidth of 0.39 keV (RMS) at $\theta = 0$ qualify PHOENIX as a well suited source for this experiment, as seen in Fig. 6.2b.

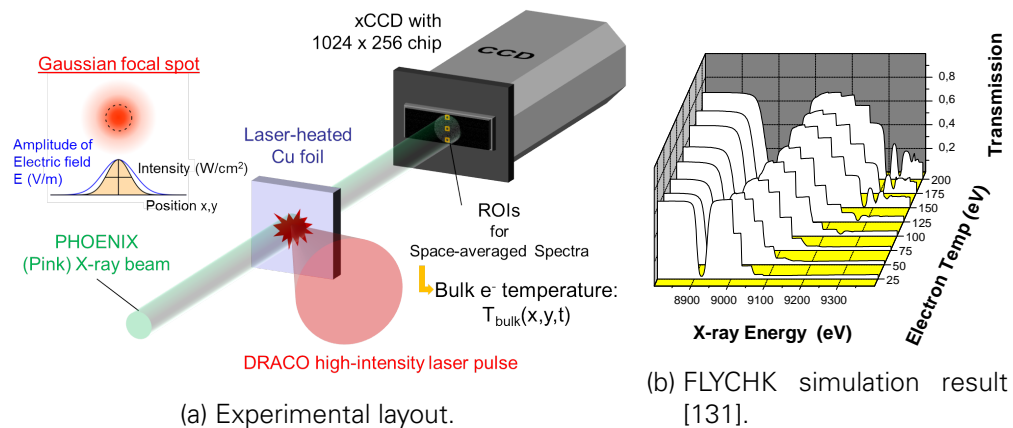


Figure 6.2: (a) Schematic experimental layout with a pink X-ray beam from in ICS source. (b) FLY code simulation for temperature dependent K-edge absorption.

While the linear inverse Compton scattering regime has been studied by us and several other groups, the nonlinear ICS regime has only been investigated once [132]. The qualitative result, a beam profile of the emitted radiation, which was modulated with inserted filter stacks, needs to be improved by high resolution spectral measurements in an effort to extend the understanding of the interaction to the nonlinear regime for testing existing scaling laws [24, 133] and high field QED effects and to quantify the distinction to classical Thomson scattering [134].

Already, with the existing setup, some data points were recorded, as shown in Fig. 6.3, which presents an initial observation of non-linear inverse Compton scattering.

The analysis is ongoing. During the measurement, the reflectivity of the mirror coating gradually degraded. For this reason, Fig. 6.3 is an average over many laser strength parameters a_0 . For more quantitative results, more data points have to be utilized during the single pixel absorption analysis to increase the spatial and temporal resolution. The expected nonlinear broadening towards lower X-ray energies is already evident but can be refined. At this moment, the setup cannot detect higher harmonics for the chosen electron beam kinetic energy, because of the quantum efficiency of the X-ray CCD camera. In a near term experiment, we plan to measure the emitted X-ray radiation from the nonlinear interaction of the DRACO laser and ELBE accelerator with the same spectral and spatial resolution as described for the linear regime in this PhD thesis.

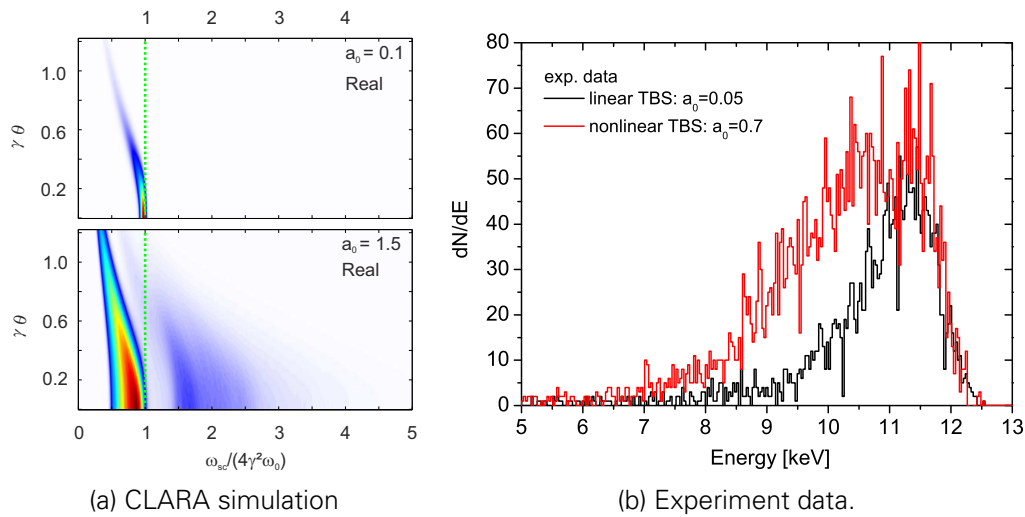


Figure 6.3: Comparison of numerically predicted X-ray spectra (a) and preliminary experimental results (b) for the non-linear interaction of an electron beam with a high-intensity laser pulse.

The knowledge gained from the interaction of the laser and a conventional linear accelerator, with the benefits of high reproducibility and control of the electron bunch parameters, can be used to predict the emitted radiation from more compact less reproducible sources such as ICS sources driven by a laser wakefield accelerator (LWFA)[135].

Such an all-optical source, not only has the advantage of an intrinsic synchronization of laser and electron and X-ray pulse, but also the peak current of the driving electron bunch can reach up to 100 kA with pulse durations as short as 1 fs. Tailoring a special interaction geometry as described by HZDR colleagues [59, 136] will drastically increase the photon yield and ultimately might lead to an optical free electron laser.

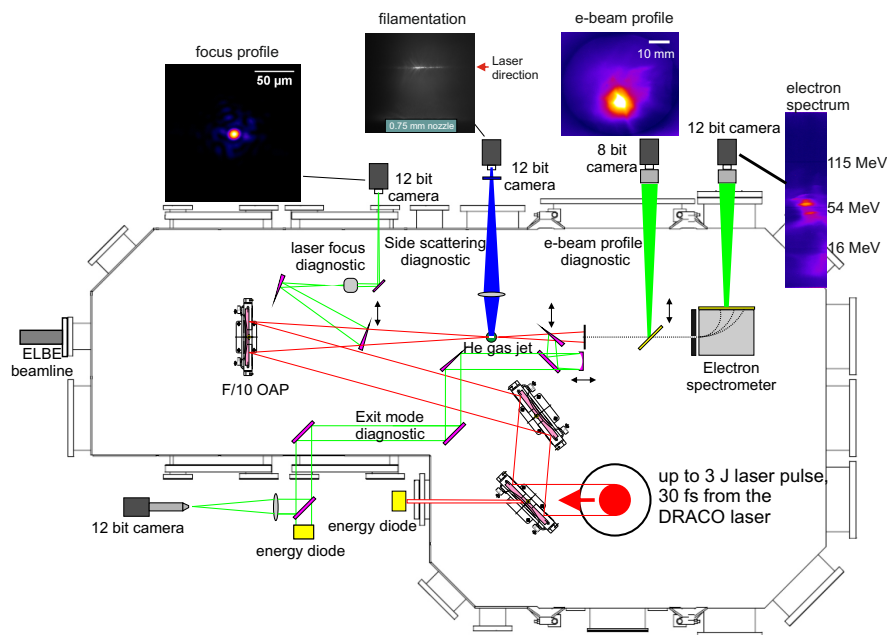


Figure 6.4: Modified PHOENIX experiment chamber for laser wakefield acceleration studies. The experiment was conducted in parallel to the ICS campaign.

To study the acceleration process in the plasma density wave, the PHOENIX setup was modified to suit the needs of a LWFA experiment during the breaks of the ICS experimental campaign. The result of the modification is shown in Fig. 6.4.

Already, in this very early stage of the experiment, electrons from the plasma background were accelerated to relativistic energies above 100 MeV, and a sensitivity to the gas backing pressure was seen. Exemplary spectra for different gas pressures and a line out for a backing pressure of $2.2 \times 10^{19} \text{ cm}^{-3}$ are illustrated in Fig. 6.5. The laser pulse contained 1.4 J energy in 30 fs. It was focused with an off-axis parabola ($f/10$) to a spot size of $9 \mu\text{m}$ ($1/e^2$ radius of the intensity), which results in a peak intensity of $I_{\text{peak}} = 3.4 \times 10^{19} \text{ W/cm}^2$, or a laser strength parameter $a_0 = 3.9$. The target was a supersonic gas jet with a nozzle opening of $750 \mu\text{m}$ resulting in a flat-top gas density profile of $400 \mu\text{m}$.

Spectra

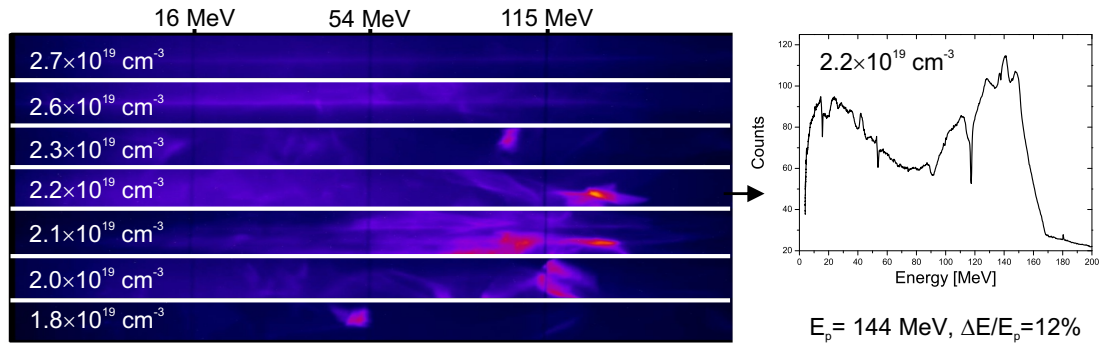


Figure 6.5: Preliminary laser wakefield acceleration results show a dependence of the electron beam energy on the gas backing pressure.

The experimental findings are in good agreement with particle-in-cell simulations and an analytic theory [87] that predicts the electron energy by

$$W_{\text{gain}} \approx 1.7 \left(\frac{P[\text{TW}]}{100} \right)^{1/3} \left(\frac{10^{18}}{n_p[\text{cm}^{-3}]} \right)^{2/3} \left(\frac{0.8}{\lambda_{\text{laser}}[\mu\text{m}]} \right)^{4/3} \\ \approx 147 \text{ MeV}$$

The obtained results are promising and comparable to findings made by other groups worldwide. The results demonstrate large acceleration gradients which ultimately can enable ultra-compact accelerator structures. Unfortunately, they also show that there is a huge difference between *acceleration* and an *accelerator*. The stability is not only linked to the gas backing pressure and gas density profile, but also to the laser focus homogeneity, the laser pulse duration and spectral shape, the laser pointing and more complex parameters such as the pulse front tilt angle and so on. Many of these parameters have highly nonlinear relations, and therefore, precise knowledge and control is important to isolate unwanted effects during the acceleration process.

Finding robust operation regimes and controlling all relevant laser and setup parameters in order to build a reliable accelerator, based on laser wakefield acceleration, is a challenging and ongoing task. An all-optical X-ray source, driven by an LWFA electron beam, would be compact and feasible for many laboratories, even at university scale. This will lead to a hugely increased number of contributors from these facilities, resulting in a great advancement in the field of ultrafast light-matter interaction.

APPENDIX

A.1 ANALYTIC SCALING OF THE PHOTON MEAN ENERGY DEVIATION ON AXIS

The subsequent derivation is based on the PhD work of D.Seipt and his contribution to our publication [122].

PRELIMINARIES

The frequency for the backscattered photon in linear Laser-Thomson backscattering ($n = 1$) from Eq. 2.12 reads

$$\omega_{sc} = \frac{2\gamma^2 (1 - \cos \varphi)}{1 + (a_0^2/2) + \gamma^2 \theta^2} \omega_0 \quad (\text{A.1})$$

For $a_0 \rightarrow 0$, and defining $\phi = \pi - \varphi$, this results in

$$\omega_{sc} = \frac{2\gamma^2 (1 + \cos \phi)}{1 + \gamma^2 \theta^2} \omega_0 \quad (\text{A.2})$$

The head-on geometry is characterized by $\phi = 0$. For the radiation on axis, one has to set $\theta = \phi$.

EMITTANCE AVERAGE

To estimate the influence of emittance, we average the frequency $\omega_{sc}(\phi)$ over a distribution $f(\phi)$ of angles ϕ (normalization $\int d\phi f(\phi) = 1$)

$$\langle \omega_{sc} \rangle = \int d\phi f(\phi) \omega_{sc}(\phi) . \quad (\text{A.3})$$

The distribution for the polar angles ϕ is assumed as

$$f(\phi) = \frac{\phi e^{-\frac{\phi^2}{2(\Delta\phi)^2}}}{(\Delta\phi)^2} , \quad (\text{A.4})$$

i.e., a χ^2 -distribution with two degrees of freedom defined over the interval $[0, \infty]$. For small $\Delta\phi$ we make an approximation to shift the upper integration boundary of the ϕ -integration from π to ∞ .

Performing a series expansion of ω_{sc} in powers of the angle ϕ with the assumption $\gamma \gg 1$ yields¹

$$\frac{\omega_{sc}}{4\gamma^2\omega_0} = 1 - \gamma^2\phi^2 + \gamma^4\phi^4 - \gamma^6\phi^6 + \mathcal{O}(\phi^8) \quad (\text{A.5})$$

Using this expansion in (A.3), the following integrals have to be solved

$$I_{2k} = \frac{1}{(\Delta\phi)^2} \int_0^\infty d\phi \phi^{2k+1} e^{-\frac{\phi^2}{2(\Delta\phi)^2}} = 2^k \Gamma(1+k) (\Delta\phi)^{2k} = 2^k k! (\Delta\phi)^{2k}. \quad (\text{A.6})$$

They read $I_0 = 1$ (normalization), $I_2 = 2(\Delta\phi)^2$, $I_4 = 8(\Delta\phi)^4$ and $I_6 = 48(\Delta\phi)^6$. Thus,

$$\langle \omega_{sc} \rangle = 4\gamma^2\omega_0 \left[1 - 2(\gamma\Delta\phi)^2 + 8(\gamma\Delta\phi)^4 - 48(\gamma\Delta\phi)^6 \right], \quad (\text{A.7})$$

with $\gamma\Delta\phi = \frac{\epsilon_n}{\sigma_r}$. For Eq. 5.8 the expansion was stopped after the quadratic term. With the experimental values $\gamma\Delta\phi = \frac{\epsilon}{\sigma_T} = \frac{21.3 \text{ mm mrad}}{140 \mu\text{m}} = 0.152$, we find the following values for ω_{sc} as a function of the order of expansion of Eq. A.7:

order	0	2	4	6
$\langle \omega_{sc} \rangle$ [keV]	13.047	12.443	12.499	12.491

INCLUDING a_0 -EFFECTS

The formula for the scattered frequency changes to

$$\omega_{sc} = \omega_0 \frac{2\gamma^2(1 + \cos \phi)}{1 + 2\gamma^2(1 - \cos \theta) + \frac{(1 + \cos \eta) a_0^2}{1 + \cos \phi}}, \quad (\text{A.8})$$

where η denotes the angle of the outgoing photon with respect to the negative laser beam direction, i.e. $\eta = 0$ means back-scattering. The angles are related by $\cos \theta = \cos \phi \cos \eta + \sin \phi \sin \eta \cos(\Delta\text{azimuths})$. Thus, for back-scattering ($\eta = 0$), it follows that $\cos \theta = \cos \phi$ and

$$\omega_{sc}(\phi) = \omega_0 \frac{2\gamma^2(1 + \cos \phi)}{1 + 2\gamma^2(1 - \cos \phi) + \frac{a_0^2}{1 + \cos \phi}}, \quad (\text{A.9})$$

$$\omega_{sc}(\phi = 0) = \omega_0 \frac{4\gamma^2}{1 + \frac{a_0^2}{2}}, \quad (\text{A.10})$$

and the ratio

$$\frac{\omega_{sc}(\phi)}{\omega_{sc}(0)} = \frac{1 + \frac{a_0^2}{2}}{2} \frac{1 + \cos \phi}{1 + 2\gamma^2(1 - \cos \phi) + \frac{a_0^2}{1 + \cos \phi}}. \quad (\text{A.11})$$

Equation A.11 can be expanded in a series in small ϕ via $\frac{\omega_{sc}(\phi)}{\omega_{sc}(0)} = \sum_k c_k \phi^{2k}$. In the limit, $\gamma \gg 1$ and for not too large a_0 ($a_0 \ll \gamma$), one simply has to replace γ^2 in the

¹ This is a series $\frac{\omega_{sc}(\phi)}{\omega_{sc}(0)} = \sum_k c_k \phi^{2k}$, with the coefficients $c_k = (-1)^k \gamma^{2k} (1 + \mathcal{O}(1/\gamma^{n>2}))$.

coefficients c_k by:

$$\gamma^2 \rightarrow \frac{\gamma^2}{1 + \frac{a_0^2}{2}}. \quad (\text{A.12})$$

Thus,

$$\langle \omega_{sc} \rangle = \frac{4\gamma^2\omega_0}{1 + \frac{a_0^2}{2}} \left[1 - 2 \frac{\gamma^2(\Delta\phi)^2}{1 + \frac{a_0^2}{2}} + 8 \frac{\gamma^4(\Delta\phi)^4}{\left(1 + \frac{a_0^2}{2}\right)^2} - 48 \frac{\gamma^6(\Delta\phi)^6}{\left(1 + \frac{a_0^2}{2}\right)^3} \right] \quad (\text{A.13})$$

The results are collected in the following table:

	order	0	2	4	6
$\langle \omega_{sc} \rangle$ [keV], $a_0 = 0$		13.047	12.443	12.499	12.491
$\langle \omega_{sc} \rangle$ [keV], $a_0 = 0.05$		13.030	12.428	12.484	12.476

A.2 DERIVATION OF THE POISSON LIKELIHOOD χ^2

Following Baker and Cousins [129], these definitions are used:

$$n_i = \text{number of events in bin } i \quad (\text{A.14})$$

$$\mathbf{n} = (n_1, n_2, n_3 \dots n_k) \quad (\text{A.15})$$

$$N = \sum_i n_i \quad (\text{A.16})$$

$$\boldsymbol{\alpha} = \text{set of parameters } (\alpha_1, \alpha_2, \alpha_3 \dots \alpha_j) \quad (\text{A.17})$$

$$y_i = \text{number of events predicted by CLARA in bin } i \quad (\text{A.18})$$

with $\mathbf{y} = (y_1, y_2, y_3 \dots y_k)$ being a function of $\boldsymbol{\alpha}$ and k being the number of bins in a histogram.

The likelihood function of observing a particular \mathbf{n} is the product of the Poisson probability of observing the total number of events N .

$$L_p(\mathbf{y}, \mathbf{n}) = \prod_i \exp(-y_i) \frac{y_i^{n_i}}{n_i!} \quad (\text{A.19})$$

The likelihood ratio λ ,

$$\lambda = L_p(\mathbf{y}, \mathbf{n}) / L_p(\mathbf{m}, \mathbf{n}) \quad (\text{A.20})$$

where \mathbf{m} are the unknown values of \mathbf{n} if there were no errors, can be used to define a likelihood- χ^2 :

$$\chi^2 = -2 \ln \lambda = -2 \ln L_p(\mathbf{y}, \mathbf{n}) + 2 L_p(\mathbf{m}, \mathbf{n}) \quad (\text{A.21})$$

The second addend is independent of \mathbf{y} ; hence, the minimization of χ^2 is the same as maximizing the ratio λ .

For Poisson distributed histograms (as in this experiment with many bin values ≤ 5) the unknown values $(m_1, m_2, m_3 \dots m_k)$ can be replaced by their estimated

$(n_1, n_2, n_3 \dots n_k)$. This leads to the Poisson likelihood chi-square χ_p^2 [129, 137]

$$\chi_p^2 = 2 \sum_i y_i - n_i + n_i \ln \left(\frac{n_i}{y_i} \right) \quad (\text{A.22})$$

BIBLIOGRAPHY

- [1] Y. Ding, F.-J. Decker, P. Emma, C. Feng, C. Field, et al. "Femtosecond X-Ray Pulse Characterization in Free-Electron Lasers Using a Cross-Correlation Technique". In: *Phys. Rev. Lett.* 109.25 (Dec. 2012), p. 254802 (cit. on p. 2).
- [2] T. Ishikawa, H. Aoyagi, T. Asaka, Y. Asano, N. Azumi, et al. "A compact X-ray free-electron laser emitting in the sub-ångström region". In: *Nat. Photonics* 6.8 (June 2012), pp. 540–544 (cit. on p. 2).
- [3] S.M. Vinko, O. Ciricosta, B.I. Cho, K. Engelhorn, H.-K. Chung, et al. "Creation and diagnosis of a solid-density plasma with an X-ray free-electron laser." In: *Nature* 482.7383 (Feb. 2012), pp. 59–62 (cit. on p. 2).
- [4] C. Rischel, A. Rousse, I. Uschmann, P.-A. Albouy, J.-P. Geindre, et al. "Femtosecond time-resolved X-ray diffraction from laser-heated organic films". In: *Nature* 390.6659 (Dec. 1997), pp. 490–492 (cit. on p. 2).
- [5] H.N. Chapman, P. Fromme, A. Barty, T.A. White, R.A. Kirian, et al. "Femtosecond X-ray protein nanocrystallography." In: *Nature* 470.7332 (Feb. 2011), pp. 73–7 (cit. on p. 2).
- [6] X. Zhang, E.C. Wasinger, A.Z. Muresan, K. Attenkofer, G. Jennings, et al. "Ultrafast stimulated emission and structural dynamics in nickel porphyrins." In: *J. Phys. Chem. A* 111.46 (Nov. 2007), pp. 11736–42 (cit. on p. 2).
- [7] P. Patel, A. Mackinnon, M. Key, T. Cowan, M. Foord, et al. "Isochoric Heating of Solid-Density Matter with an Ultrafast Proton Beam". In: *Phys. Rev. Lett.* 91.12 (Sept. 2003), p. 125004 (cit. on p. 2).
- [8] F. Perez, L. Gremillet, M. Koenig, S.D. Baton, P. Audebert, et al. "Enhanced Isochoric Heating from Fast Electrons Produced by High-Contrast, Relativistic-Intensity Laser Pulses". In: *Phys. Rev. Lett.* 104.8 (Feb. 2010), p. 085001 (cit. on p. 2).
- [9] H.-P. Liermann, W. Morgenroth, A. Ehnes, A. Berghäuser, B. Winkler, et al. "The Extreme Conditions Beamline at PETRA III, DESY: Possibilities to conduct time resolved monochromatic diffraction experiments in dynamic and laser heated DAC". In: *J. Phys. Conf. Ser.* 215 (Mar. 2010), p. 012029 (cit. on p. 2).

- [10] Y. Sentoku, E. D Humieres, L. Romagnani, P. Audebert, and J. Fuchs. "Dynamic Control over Mega-Ampere Electron Currents in Metals Using Ionization-Driven Resistive Magnetic Fields". In: *Phys. Rev. Lett.* 107.13 (Sept. 2011), p. 135005 (cit. on p. 2).
- [11] E. Gaul, M. Martinez, J. Blakeney, M. Ringuette, D. Hammond, et al. "Petawatt lasers based on hybrid, OPCPA-Nd: glass amplification". In: *Lasers and Electro-Optics 2009 and the European Quantum Electronics Conference. CLEO Europe-EQEC 2009. European Conference on.* IEEE. 2009, pp. 1–1 (cit. on p. 2).
- [12] E.W. Gaul, M. Martinez, J. Blakeney, A. Jochmann, M. Ringuette, et al. "1.1 Petawatt Hybrid, OPCPA-Nd: glass Laser Demonstrated". In: *Frontiers in Optics.* Optical Society of America. 2008, FWX3 (cit. on p. 2).
- [13] M. Siebold, M. Hornung, R. Boedefeld, S. Podleska, S. Klingebiel, et al. "Terawatt diode-pumped Yb:CaF₂ laser". In: *Optics letters* 33.23 (2008), pp. 2770–2772 (cit. on p. 2).
- [14] Mathias Siebold, Fabian Roeser, Markus Loeser, Daniel Albach, and Ulrich Schramm. "PEneLOPE: a high peak-power diode-pumped laser system for laser-plasma experiments". In: vol. 8780. 2013, pages (cit. on p. 2).
- [15] A.H. Compton. "A quantum theory of the scattering of X-rays by light elements". In: *Phys. Rev.* 5 (1923), p. 483 (cit. on pp. 2, 8).
- [16] E. Feenberg and H. Primakoff. "Interaction of Cosmic-Ray Primaries with Sunlight and Starlight". In: *Physical Review* 73.5 (Mar. 1948), pp. 449–469 (cit. on p. 3).
- [17] R.H. Milburn. "Electron scattering by an intense polarized photon field". In: *Phys. Rev. Lett.* 10 (1963), p. 75 (cit. on pp. 3, 8).
- [18] P. Sprangle, A. Ting, E. Esarey, and A. Fisher. "Tunable, short pulse hard x-rays from a compact laser synchrotron source". In: *J. Appl. Phys.* 72.11 (Dec. 1992), p. 5032 (cit. on p. 3).
- [19] E. Esarey, S.K. Ride, and P. Sprangle. "Nonlinear Thomson scattering of intense laser pulses from beams and plasmas". In: *Phys. Rev. E* 48 (1993), p. 3003 (cit. on pp. 3, 8, 13, 14, 63).
- [20] S.K. Ride, E. Esarey, and M. Baine. "Thomson scattering of intense lasers from electron beams at arbitrary interaction angles". In: *Phys. Rev. E* 52 (1995), p. 5425 (cit. on pp. 3, 8).
- [21] C. Bula, K.T. McDonald, E.J. Prebys, C. Bamber, S. Boege, et al. "Observation of nonlinear effects in Compton scattering." In: *Phys. Rev. Lett.* 76.17 (Apr. 1996), pp. 3116–3119 (cit. on p. 3).
- [22] P. Catravas, E. Esarey, and W.P. Leemans. "Femtosecond x-rays from Thomson scattering using laser wakefield accelerators". In: *Spectrum* 12 (2001), pp. 1828–1834 (cit. on pp. 3, 13).

- [23] P. Tomassini, A. Bacci, J. Cary, M. Ferrario, A. Giulietti, et al. "Linear and Non-linear Thomson Scattering for Advanced X-ray Sources in PLASMONX". In: *IEEE Trans. Plasma Sci.* 36.4 (Aug. 2008), pp. 1782–1789 (cit. on p. 3).
- [24] A. Debus, S. Bock, M. Bussmann, T.E. Cowan, A. Jochmann, et al. "Linear and non-linear Thomson-scattering x-ray sources driven by conventionally and laser plasma accelerated electrons". In: *Proc. SPIE* (2009), pages (cit. on pp. 3, 13, 14, 16, 17, 33, 34, 37, 54, 68, 79).
- [25] R.W. Schoenlein, W.P. Leemans, A.H. Chin, P. Volfbeyn, T.E. Glover, et al. "Femtosecond X-ray Pulses at 0.4A Generated by 90° Thomson Scattering: A Tool for Probing the Structural Dynamics of Materials". In: *Science* (80-.). 274. October (1996), pp. 236–238 (cit. on pp. 3, 4).
- [26] I.V. Pogorelsky, T. Hirose, S. Kashiwagi, V. Yakimenko, K. Kusche, et al. "Demonstration of 8×10^{18} photons/second peaked at 1.8 \AA in a relativistic Thomson scattering experiment". In: *Phys. Rev. Spec. Top. - Accel. Beams* 3 (2000), pp. 2–9 (cit. on pp. 3, 4, 13, 68).
- [27] S.G. Anderson, C.P.J. Barty, S.M. Betts, W.J. Brown, J.K. Crane, et al. "Short-pulse, high-brightness X-ray production with the PLEIADES Thomson-scattering source". In: *Appl. Phys. B Lasers Opt.* 78.7-8 (May 2004), pp. 891–894 (cit. on p. 3).
- [28] W.S. Graves, W. Brown, F.X. Kaertner, and D.E. Moncton. "MIT inverse Compton source concept". In: *Nucl. Instruments Methods Phys. Res. Sect. A Accel. Spectrometers, Detect. Assoc. Equip.* 608.1 (Sept. 2009), S103–S105 (cit. on pp. 3, 68).
- [29] G. Priebe, D. Filippetto, O. Williams, Y.M. Saveliev, L.B. Jones, et al. "Status of the inverse Compton backscattering source at Daresbury Laboratory". In: *Nucl. Instruments Methods Phys. Res. Sect. A Accel. Spectrometers, Detect. Assoc. Equip.* 608.1 (Sept. 2009), S109–S112 (cit. on p. 3).
- [30] D.J. Gibson, F. Albert, S.G. Anderson, S.M. Betts, M.J. Messerly, et al. "Design and operation of a tunable MeV-level Compton-scattering-based γ -ray source". In: *Phys. Rev. Spec. Top. - Accel. Beams* 13.7 (July 2010), pp. 1–12 (cit. on pp. 3, 4, 68).
- [31] W. Luo, W. Xu, Q.Y. Pan, X.Z. Cai, J.G. Chen, et al. "A laser-Compton scattering prototype experiment at 100 MeV linac of Shanghai Institute of Applied Physics." In: *Rev. Sci. Instrum.* 81.1 (Jan. 2010), p. 013304 (cit. on pp. 3, 68).
- [32] W.P. Leemans, R.W. Schoenlein, P. Volfbeyn, A.H. Chin, T.E. Glover, et al. "X-Ray Based Subpicosecond Electron Bunch Characterization Using 90° Thomson Scattering." In: *Phys. Rev. Lett.* 77.20 (Nov. 1996), pp. 4182–4185. eprint: [/link.aps.org/doi/10.1103/PhysRevLett.77.4182](http://link.aps.org/doi/10.1103/PhysRevLett.77.4182) (http:) (cit. on pp. 3, 4).
- [33] K. Chouffani, F. Harmon, D. Wells, J. Jones, and G. Lancaster. "Determination of electron beam parameters by means of laser-Compton scattering". In: *Phys. Rev. Spec. Top. - Accel. Beams* 9.5 (May 2006) (cit. on pp. 3, 4, 14, 15, 61, 68).

- [34] C. Sun, J. Li, G. Rusev, A. Tonchev, and Y. Wu. “Energy and energy spread measurements of an electron beam by Compton scattering method”. In: *Phys. Rev. Spec. Top. - Accel. Beams* 12.6 (June 2009), pp. 062801– (cit. on p. 3).
- [35] C. Harvey, T. Heinzl, and M. Marklund. “Symmetry breaking from radiation reaction in ultra-intense laser fields”. In: *Phys. Rev. D* 84.11 (2011), p. 116005 (cit. on p. 4).
- [36] E. Lötstedt, U.D. Jentschura, and C.H. Keitel. “Laser Channeling of Bethe-Heitler Pairs”. In: *Phys. Rev. Lett.* 101.20 (Nov. 2008), p. 203001 (cit. on p. 4).
- [37] T. Heinzl, B. Liesfeld, K.-U. Amthor, H. Schwöerer, R. Sauerbrey, and A. Wipf. “On the observation of vacuum birefringence”. In: *Opt. Commun.* 267.2 (Nov. 2006), pp. 318–321 (cit. on p. 4).
- [38] S. Chen, N. D. Powers, I. Ghebregziabher, C. M. Maharjan, C. Liu, et al. “MeV-Energy X Rays from Inverse Compton Scattering with Laser-Wakefield Accelerated Electrons”. In: *Phys. Rev. Lett.* 110 (15 Apr. 2013), p. 155003 (cit. on p. 4).
- [39] K. Ta Phuoc, S. Corde, C. Thaur, V. Malka, A. Tafzi, et al. “All-optical Compton gamma-ray source”. In: *Nature Photon.* 6 (5 Apr. 2012), p. 308 (cit. on p. 4).
- [40] A. Jochmann, A. Irman, U. Lehnert, J.P. Couperus, M. Kuntzsch, et al. “Operation of a picosecond narrow-bandwidth Laser–Thomson-backscattering X-ray source”. In: *Nuclear Instruments and Methods in Physics Research Section B: Beam Interactions with Materials and Atoms* 309 (2013), pp. 214–217 (cit. on pp. 4, 54–57).
- [41] D B Thorn, C G R Geddes, N H Matlis, G R Plateau, E H Esarey, et al. “Spectroscopy of betatron radiation emitted from laser-produced wakefield accelerated electrons.” en. In: 81.10 (Oct. 2010), 10E325 (cit. on p. 4).
- [42] G. Plateau, C. Geddes, D. Thorn, M. Chen, C. Benedetti, et al. “Low-Emittance Electron Bunches from a Laser-Plasma Accelerator Measured using Single-Shot X-Ray Spectroscopy”. In: *Phys. Rev. Lett.* 109.6 (Aug. 2012) (cit. on pp. 4, 52).
- [43] D. Attwood. *Soft x-rays and extreme ultraviolet radiation : principles and applications*. Cambridge New York: Cambridge University Press, 2007 (cit. on p. 8).
- [44] W. Brown and F. Hartemann. “Three-dimensional time and frequency-domain theory of femtosecond x-ray pulse generation through Thomson scattering”. In: *Phys. Rev. Spec. Top. - Accel. Beams* 7.6 (June 2004), p. 060703 (cit. on p. 8).
- [45] G. Fiocco and E. Thompson. “Thomson scattering of optical radiation from an electron beam”. In: *Phys. Rev. Lett.* 10 (1963), p. 89 (cit. on p. 8).
- [46] F. Hartemann, H. Baldi, A. Kerman, A. Le Foll, N. Luhmann, and B. Rupp. “Three-dimensional theory of emittance in Compton scattering and x-ray protein crystallography”. In: *Phys. Rev. E* 64.1 (June 2001), pp. 1–26 (cit. on pp. 8, 16, 68).

- [47] J.D. Jackson. *Classical Electrodynamics*. 3rd. De Gruyter, 1999 (cit. on pp. 8, 11, 12).
- [48] K.-J. Kim, S. Chattopadhyay, and C.V. Shank. "Generation of femtosecond X-rays by 90° Thomson scattering". In: *Nucl. Instruments Methods Phys. Res. Sect. A Accel. Spectrometers, Detect. Assoc. Equip.* 341.1-3 (Mar. 1994), pp. 351–354 (cit. on p. 8).
- [49] Y.Y. Lau, F. He, D.P. Umstadter, and R. Kowalczyk. "Nonlinear Thomson scattering: A tutorial". In: *Phys. Plasmas* 10.5 (2003), p. 2155 (cit. on p. 8).
- [50] W. Luo, W. Xu, Q.Y. Pan, Z.D. An, X.L. Cai, et al. "A 4D Monte Carlo laser-Compton scattering simulation code for the characterization of the future energy-tunable SLEGS". In: *Nucl. Instruments Methods Phys. Res. Sect. A Accel. Spectrometers, Detect. Assoc. Equip.* 660.1 (Dec. 2011), pp. 108–115 (cit. on pp. 8, 16).
- [51] C. Sun and Y. Wu. "Theoretical and simulation studies of characteristics of a Compton light source". In: *Phys. Rev. Spec. Top. - Accel. Beams* 14.4 (Apr. 2011), pp. 044701– (cit. on pp. 8, 13, 16, 68).
- [52] Y.K. Wu. "A 4D Monte Carlo Compton scattering code". In: *2009 IEEE Nucl. Sci. Symp. Conf. Rec.* IEEE, Oct. 2009, pp. 477–480 (cit. on p. 8, 16).
- [53] K. Wille. *The Physics of Particle Accelerators*. Oxford University Press, 2000 (cit. on pp. 10, 54).
- [54] F. Träger, ed. *Springer Handbook of Lasers and Optics*. Springer Berlin / Heidelberg, 2012 (cit. on p. 10).
- [55] F.H. OShea, O. Williams, G. Andonian, S. Barber, Y. Sakai, et al. "Single shot diffraction of picosecond 8.7-keV x-ray pulses". In: *Phys. Rev. Spec. Top. - Accel. Beams* 15.2 (Feb. 2012), p. 020702 (cit. on pp. 13, 69).
- [56] W.P. Leemans, R.W. Schoenlein, P. Volfbeyn, A.H. Chin, T.E. Glover, et al. "Interaction of relativistic electrons with ultrashort laser pulses: generation of femtosecond X-rays and microprobing of electron beams". In: *IEEE J. Quantum Electron.* 33.11 (1997), pp. 1925–1934 (cit. on pp. 14, 15).
- [57] W. Leemans, S. Chattopadhyay, E. Esarey, A. Zholents, M. Zolotarev, et al. "Femtosecond X-ray generation through relativistic electron beam-laser interaction". In: *Comptes Rendus l'Académie des Sci. - Ser. IV - Phys.* 1.3 (Apr. 2000), pp. 279–296 (cit. on p. 14).
- [58] A.D. Debus, M. Bussmann, M. Siebold, A. Jochmann, U. Schramm, et al. "Traveling-wave Thomson scattering and optical undulators for Å high-yield EUV and X-ray sources". In: *Appl. Phys. B* 100.1 (May 2010), pp. 61–76 (cit. on pp. 15, 78).
- [59] K. Steiniger, R. Widera, R. Pausch, A. Debus, M. Bussmann, and U. Schramm. "Wave optical description of the Traveling-Wave Thomson-Scattering optical undulator field and its application to the TWTS-FEL". In: *Nucl. Instruments Methods Phys. Res. Sect. A Accel. Spectrometers, Detect. Assoc. Equip.* 740 (Mar. 2014), pp. 147–152 (cit. on pp. 15, 80).

- [60] B. Terzic, K. Deitrick, A.S. Hofler, and G.A. Krafft. "Narrow-Band Emission in Thomson Sources Operating in the High-Field Regime". In: *Phys. Rev. Lett.* 112.7 (Feb. 2014), p. 74801 (cit. on p. 15).
- [61] I. Ghebregziabher, B. Shadwick, and D. Umstadter. "Spectral bandwidth reduction of Thomson scattered light by pulse chirping". In: *Phys. Rev. Spec. Top. - Accel. Beams* 16.3 (Mar. 2013), p. 030705 (cit. on p. 15).
- [62] Alexander D. Debus. "Brilliant radiation sources by laser-plasma accelerators and optical undulators". PhD thesis. TU Dresden, HZDR, 2012 (cit. on p. 16).
- [63] *Pulsar Physics GPT*. <http://www.pulsar.nl/gpt> (cit. on pp. 16, 34).
- [64] F. Richard, J.R. Schneider, D. Trines, and A. Wagner. *TESLA Technical Design Report*. Tech. rep. March. DESY, 2001 (cit. on p. 20).
- [65] A. Arnold, H. Büttig, D. Janssen, T. Kamps, G. Klemz, et al. "Development of a superconducting radio frequency photoelectron injector". In: *Nucl. Instruments Methods Phys. Res. Sect. A Accel. Spectrometers, Detect. Assoc. Equip.* 577.3 (July 2007), pp. 440–454 (cit. on p. 23).
- [66] R. Xiang, A. Arnold, H. Büttig, D. Janssen, M. Justus, et al. "Cs₂Te normal conducting photocathodes in the superconducting rf gun". In: *Phys. Rev. Spec. Top. - Accel. Beams* 13.4 (Apr. 2010), p. 043501 (cit. on pp. 22, 23).
- [67] J. Valdmanis and G. Mourou. "Subpicosecond electrooptic sampling: principles and applications". In: *Quantum Electron. IEEE J.* 22. January (1986), pp. 69–78 (cit. on p. 23).
- [68] D. Oepts. "Picosecond electronbunch length measurement using an electro-optic sensor". In: *21st Int. FEL Conf.* Hamburg, 1999 (cit. on p. 23).
- [69] C. Schneider. *ELBE Log-Book*. Apr. 2014 (cit. on pp. 23, 24).
- [70] C. Kaya, C. Schneider, A. Al-Shemmary, W. Seidel, M. Kuntzsch, et al. "Phase sensitive monitoring of electron bunch form and arrival time in superconducting linear accelerators". In: *Appl. Phys. Lett.* 100.14 (Apr. 2012), p. 141103 (cit. on pp. 23, 24, 54).
- [71] C.P. Browne. "Broad-Range Magnetic Spectrograph". English. In: *Rev. Sci. Instrum.* 27.11 (Nov. 1956), p. 899 (cit. on p. 25).
- [72] C. Nair, M. Erhard, A. Junghans, D. Bemmerer, R. Beyer, et al. "Photoactivation experiment on Au¹⁹⁷ and its implications for the dipole strength in heavy nuclei". In: *Physical Review C* 78.5 (Nov. 2008), p. 055802 (cit. on p. 26).
- [73] K.B. Unser. *Measuring bunch intensity, beam loss and bunch lifetime in LEP*. Tech. rep. Geneva: CERN, 1990 (cit. on p. 27).
- [74] K. Zeil, S.D. Kraft, A. Jochmann, F. Kroll, W. Jahr, et al. "Absolute response of Fuji imaging plate detectors to picosecond-electron bunches". In: *Review of Scientific Instruments* 81.1 (2010), p. 013307 (cit. on p. 27).

- [75] D. Strickland and G. Mourou. "Compression of amplified chirped optical pulses". In: *Opt. Commun.* 56.3 (Dec. 1985), pp. 219–221 (cit. on p. 28).
- [76] O. Martinez. "Design of high-power ultrashort pulse amplifiers by expansion and recompression". In: *IEEE J. Quantum Electron.* 23.8 (Aug. 1987), pp. 1385–1387 (cit. on p. 28).
- [77] T. Brabec, C. Spielmann, P.F. Curley, and F. Krausz. "Kerr lens mode locking". In: *Opt. Lett.* 17.18 (Sept. 1992), p. 1292 (cit. on p. 28).
- [78] G. Cheriaux, P. Rousseau, F. Salin, J.P. Chambaret, B. Walker, and L.F. Dimauro. "Aberration-free stretcher design for ultrashort-pulse amplification." In: *Opt. Lett.* 21.6 (Mar. 1996), pp. 414–6 (cit. on p. 29).
- [79] P. Tournois. "Acousto-optic programmable dispersive filter for adaptive compensation of group delay time dispersion in laser systems". In: *Opt. Commun.* 140.4-6 (Aug. 1997), pp. 245–249 (cit. on p. 29).
- [80] T. Oksenhendler, D. Kaplan, P. Tournois, G.M. Greetham, and F. Estable. "Intracavity acousto-optic programmable gain control for ultra-wide-band regenerative amplifiers". In: *Appl. Phys. B* 83.4 (May 2006), pp. 491–494 (cit. on p. 29).
- [81] E. Treacy. "Optical pulse compression with diffraction gratings". English. In: *IEEE J. Quantum Electron.* 5.9 (Sept. 1969), pp. 454–458 (cit. on p. 29).
- [82] Y. Petit, S. Henin, W.M. Nakaema, P. Béjot, A. Jochmann, et al. "1-J white-light continuum from 100-TW laser pulses". In: *Physical Review A* 83.1 (2011), p. 013805 (cit. on p. 29).
- [83] S. Henin, Y. Petit, J. Kasparian, J.-P. Wolf, A. Jochmann, et al. "Saturation of the filament density of ultrashort intense laser pulses in air". In: *Applied Physics B* 100.1 (2010), pp. 77–84 (cit. on p. 29).
- [84] C. Erler. "Aufbau und Entwicklung einer Lagestabilisierung für einen Hochleistungslaserstrahl". MA thesis. University of Applied Sciences Jena, 2009 (cit. on p. 30).
- [85] *Sacher Lasertechnik*. <http://www.sacher-laser.com/> (cit. on p. 30).
- [86] A. Pukhov, S. Gordienko, S. Kiselev, and I. Kostyukov. "The bubble regime of laser-plasma acceleration: monoenergetic electrons and the scalability". In: *Plasma Phys. Control. Fusion* 46.12B (2004), B179 (cit. on p. 31).
- [87] W. Lu, M. Tzoufras, C. Joshi, F. Tsung, W. Mori, et al. "Generating multi-GeV electron bunches using single stage laser wakefield acceleration in a 3D nonlinear regime". In: *Phys. Rev. Spec. Top. - Accel. Beams* 10.6 (June 2007), pp. 1–12 (cit. on pp. 31, 81).
- [88] F. Ballarini, G. Battistoni, M. Campanella, M. Carboni, F. Cerutti, et al. "The FLUKA code: an overview". In: *J. Phys. Conf. Ser.* 41 (May 2006), pp. 151–160 (cit. on p. 31).

- [89] K. Halbach. "Design of permanent multipole magnets with oriented rare earth cobalt material". In: *Nucl. Instruments Methods* 169.1 (Feb. 1980), pp. 1–10 (cit. on p. 34).
- [90] J. Lim, P. Frigola, J.B. Rosenzweig, S. Telfer, G. Travish, et al. "An adjustable permanent magnet quadrupole (PMQ) final focus system for low energy experiments". In: *Proc. 2003 Bipolar/BiCMOS Circuits Technol. Meet. (IEEE Cat. No.03CH37440)* (2003), pp. 2192–2194 (cit. on p. 34).
- [91] T. Eichner, F. Grüner, S. Becker, M. Fuchs, D. Habs, et al. "Miniature magnetic devices for laser-based, table-top free-electron lasers". In: *Phys. Rev. Spec. Top. - Accel. Beams* 10.8 (Aug. 2007), p. 082401 (cit. on p. 34).
- [92] O. Chubar, P. Elleaume, and J. Chavanne. "A three-dimensional magnetostatics computer code for insertion devices". In: *J. Synchrotron Radiat.* 5.3 (1998), pp. 481–484 (cit. on p. 34).
- [93] O. Zarini. "Student internship". Supervised by A. Debus, A. Jochmann, A. Irman and M. Bussmann (cit. on pp. 34–36).
- [94] S. Becker, M. Bussmann, S. Raith, M. Fuchs, R. Weingartner, et al. "Characterization and tuning of ultrahigh gradient permanent magnet quadrupoles". In: *Phys. Rev. Spec. Top. - Accel. Beams* 12.10 (Oct. 2009), pp. 1–7 (cit. on p. 35).
- [95] $B = \frac{2\pi}{\lambda} \int n_2 l(z) dz$ (cit. on p. 37).
- [96] *ISO Standard 11146: Lasers and laser-related equipment, Test methods for laser beam widths, divergence angles and beam propagation ratios.* 2005 (cit. on p. 38).
- [97] Newport. *Technical Notes, Gaussian Beam Optics.* <http://www.newport.com/Gaussian-Beam-Optics/144899/1033/content.aspx> (cit. on p. 38).
- [98] *E.g., CVI TLMB coating: 1.3 J/cm² damage threshold (measured with 46 fs pulse duration at 800 nm).* <http://www.idex-op.com/> (cit. on p. 38).
- [99] P.A. Walker, N. Bourgeois, W. Rittershofer, J. Cowley, N. Kajumba, et al. "Investigation of GeV-scale electron acceleration in a gas-filled capillary discharge waveguide". en. In: *New Journal of Physics* 15.4 (Apr. 2013), p. 045024 (cit. on p. 38).
- [100] K. Zeil, S.D. Kraft, S. Bock, M. Bussmann, T.E. Cowan, et al. "The scaling of proton energies in ultrashort pulse laser plasma acceleration". In: *New J. Phys.* 12.4 (Apr. 2010), p. 045015 (cit. on p. 39).
- [101] J. Primot and L. Sogno. "Achromatic three-wave (or more) lateral shearing interferometer". In: *J. Opt. Soc. Am. A* 12.12 (Dec. 1995), p. 2679 (cit. on p. 41).
- [102] S.C. Gupta. "Phase-locked loops". In: *Proc. IEEE* 63.2 (1975), pp. 291–306 (cit. on p. 45).
- [103] G.M. Knippels, M.J. van de Pol, H.P. Pellemans, P.C. Planken, and A.F. van der Meer. "Two-color facility based on a broadly tunable infrared free-electron

- laser and a subpicosecond-synchronized 10-fs-Ti:sapphire laser." In: *Opt. Lett.* 23.22 (Nov. 1998), pp. 1754–6 (cit. on p. 45).
- [104] Rohde & Schwarz FSUP. http://www.rohde-schwarz.com/en/product/fsup-productstartpage_63493-8429.html (cit. on p. 45).
- [105] S. Sabah and R. Lorenz. "Design and calibration of IQ-Mixers". In: *EPAC* (1998), pp. 1589–1591 (cit. on pp. 45, 46).
- [106] M. Kuntzsch. *Personal communication*. 2010 (cit. on p. 46).
- [107] Stanford Research Systems. *SRS DG645*. <http://www.thinksrs.com/products/DG645.htm> (cit. on p. 46).
- [108] Stanford Computer Optics. *4 Picos*. <http://www.stanfordcomputeroptics.com> (cit. on p. 47).
- [109] A.H. Mahan and A. Gallagher. "Transition radiation for the diagnosis of low-energy electron beams". In: *Rev. Sci. Instrum.* 47.1 (Aug. 1976), p. 81 (cit. on p. 47).
- [110] D.W. Rule. "Transition radiation diagnostics for intense charged particle beams". In: *Nucl. Instruments Methods Phys. Res. Sect. B Beam Interact. with Mater. Atoms* 24-25 (Apr. 1987), pp. 901–904 (cit. on p. 47).
- [111] J. Wang, Y. Wang, D. Gonzalez-Diaz, H. Chen, X. Fan, et al. "Development of high-rate MRPCs for high resolution time-of-flight systems". In: *Nuclear Instruments and Methods in Physics Research Section A: Accelerators, Spectrometers, Detectors and Associated Equipment* 713 (June 2013), pp. 40–51 (cit. on p. 48).
- [112] *Amptek*. <http://www.amptek.com/anczt2.html> (cit. on pp. 48, 49).
- [113] B. Pritychenko, R. Arcilla, T.W. Burrows, C.L. Dunford, M.W. Herman, et al. "NNDC Stand: Activities and Services of the National Nuclear Data Center". In: *International Conference on Nuclear Data for Science and Technology*. Ed. by R. C. Haight, M. B. Chadwick, T. Kawano, and P. Talou. Vol. 769. American Institute of Physics Conference Series. May 2005, pp. 132–135 (cit. on pp. 48, 51).
- [114] *Andor Technologies*. <http://www.andor.com/scientific-cameras/idus-spectroscopy-cameras/idus-420-series> (cit. on p. 50).
- [115] F. Attix. *Introduction to radiological physics and radiation dosimetry, Ch.7*. New York: Wiley, 1986 (cit. on p. 49).
- [116] A.C. Brinkman, H.J. Aarts, G. Branduardi-Raymont, C.J. Hailey, F.A. Jansen, et al. "Spectroscopic Investigations With A Reflection Grating Spectrometer". In: *Proc. SPIE* 1159 (1989), pp. 495–509 (cit. on p. 50).
- [117] C. Fourment, N. Arazam, C. Bonte, T. Caillaud, D. Descamps, et al. "Broadband, high dynamics and high resolution charge coupled device-based spectrometer in dynamic mode for multi-keV repetitive x-ray sources." In: *Rev. Sci. Instrum.* 80.8 (Aug. 2009), p. 083505 (cit. on p. 50).

- [118] *Princeton Instruments*. http://www.princetoninstruments.com/Uploads/Princeton/Documents/TechNotes/Direct_detection_of%20xrays_technote_1RevA0.pdf (cit. on p. 50).
- [119] B.L. Henke, E.M. Gullikson, and J.C. Davis. "X-Ray Interactions: Photoabsorption, Scattering, Transmission, and Reflection at $E = 50\text{--}30,000$ eV, $Z = 1\text{--}92$ ". In: *At. Data Nucl. Data Tables* 54.2 (July 1993), pp. 181–342 (cit. on pp. 52, 56).
- [120] S. Trotsenko. *Personal communication*. 2013 (cit. on p. 62).
- [121] J. Teichert, A. Arnold, H. Büttig, U. Lehnert, P. Michel, et al. "Operation of the superconducting RF photo gun at ELBE". en. In: *J. Phys. Conf. Ser.* 298.1 (May 2011), p. 012008 (cit. on p. 63).
- [122] A. Jochmann, A. Irman, M. Bussmann, J.P. Couperus, T.E. Cowan, et al. "High Resolution Energy-Angle Correlation Measurement of Hard X Rays from Laser-Thomson Backscattering". In: *Physical review letters* 111.11 (2013), p. 114803 (cit. on pp. 64, 75, 78, 83).
- [123] P.F. Rusch and J.P. Lelieur. "Analytical Moments of Skewed Gaussian Distribution Functions". In: *Anal. Chem.* 45.8 (1973), pp. 1541–1543 (cit. on p. 64).
- [124] F. Albert, S.G. Anderson, D.J. Gibson, R.A. Marsh, S.S. Wu, et al. "Design of narrow-band Compton scattering sources for nuclear resonance fluorescence". In: *Phys. Rev. Spec. Top. - Accel. Beams* 14.5 (May 2011), p. 050703 (cit. on p. 68).
- [125] K. Chouffani, D. Wells, F. Harmon, J. Jones, and G. Lancaster. "Laser-Compton scattering from a 20MeV electron beam". In: *Nucl. Instruments Methods Phys. Res. Sect. A Accel. Spectrometers, Detect. Assoc. Equip.* 495.2 (Dec. 2002), pp. 95–106 (cit. on p. 69).
- [126] A.S. Chauchat, V. Le Flanchec, A. Binet, J.L. Flament, P. Balleyguier, et al. "Construction of a Compton source for X-rays in the ELSA facility". In: *Nucl. Instruments Methods Phys. Res. Sect. A Accel. Spectrometers, Detect. Assoc. Equip.* 608.1 (Sept. 2009), S99–S102 (cit. on p. 69).
- [127] O. Lundh, J. Lim, C. Rechatin, L. Ammoura, A. Ben-Ismaïl, et al. "Few femtosecond, few kiloampere electron bunch produced by a laser-plasma accelerator". In: *Nat. Phys.* 7.3 (Jan. 2011), pp. 219–222 (cit. on p. 69).
- [128] T.E. Cowan. *Personal communication*. 2013 (cit. on p. 70).
- [129] S. Baker and R.D. Cousins. "Clarification of the use of CHI-square and likelihood functions in fits to histograms". In: *Nucl. Instruments Methods Phys. Res.* 221.2 (Apr. 1984), pp. 437–442 (cit. on pp. 72, 85, 86).
- [130] *HSQ Scientific Case - Matter under extreme conditions*. Unpublished - Internal use only. Nov. 2009 (cit. on p. 79).
- [131] H.-K. Chung, M.H. Chen, W.L. Morgan, Y. Ralchenko, and R.W. Lee. "FLY-CHK: Generalized population kinetics and spectral model for rapid spectro-

- scopic analysis for all elements". In: *High Energy Density Physics* 1.1 (2005), pp. 3–12 (cit. on p. 79).
- [132] M. Babzien, I. Ben-Zvi, K. Kusche, I. Pavlishin, I. Pogorelsky, et al. "Observation of the Second Harmonic in Thomson Scattering from Relativistic Electrons". In: *Phys. Rev. Lett.* 96.5 (Feb. 2006), pp. 1–4 (cit. on p. 79).
- [133] D. Seipt and B. Kämpfer. "Scaling law for the photon spectral density in the nonlinear Thomson-Compton scattering". In: *Phys. Rev. Spec. Top. - Accel. Beams* 14.4 (Apr. 2011), p. 040704 (cit. on p. 79).
- [134] T. Heinzl, D. Seipt, and B. Kämpfer. "Beam-shape effects in nonlinear Compton and Thomson scattering". In: *Phys. Rev. A* 81.2 (Feb. 2010), p. 022125 (cit. on p. 79).
- [135] T. Tajima and J. Dawson. "Laser Electron Accelerator". In: *Phys. Rev. Lett.* 43.4 (July 1979), pp. 267–270 (cit. on p. 80).
- [136] A.D. Debus, M. Bussmann, M. Siebold, A. Jochmann, U. Schramm, et al. "Traveling-wave Thomson scattering and optical undulators for high-yield EUV and X-ray sources". In: *Applied Physics B* 100.1 (2010), pp. 61–76 (cit. on p. 80).
- [137] J. Beringer, J.-F. Arguin, R.M. Barnett, K. Copic, O. Dahl, et al. "Review of Particle Physics". In: *Phys. Rev. D* 86.1 (July 2012), p. 010001 (cit. on p. 86).

PUBLICATIONS BY THE AUTHOR

- [1] A. Jochmann, A. Irman, M. Bussmann, J.P. Couperus, T.E. Cowan, et al. "High Resolution Energy-Angle Correlation Measurement of Hard X Rays from Laser-Thomson Backscattering". In: *Physical review letters* 111.11 (2013), p. 114803
- [2] A. Jochmann, A. Irman, U. Lehnert, J.P. Couperus, M. Kuntzsch, et al. "Operation of a picosecond narrow-bandwidth Laser-Thomson-backscattering X-ray source". In: *Nuclear Instruments and Methods in Physics Research Section B: Beam Interactions with Materials and Atoms* 309 (2013), pp. 214–217
- [3] Y. Petit, S. Henin, W.M. Nakaema, P. B ejot, A. Jochmann, et al. "1-J white-light continuum from 100-TW laser pulses". In: *Physical Review A* 83.1 (2011), p. 013805
- [4] M. Kuntzsch, A. Buechner, M. Gensch, A. Jochmann, T. Kirschke, et al. "Concept of femtosecond timing and synchronization scheme at elbe". In: *Proc. of IPAC* (2011)
- [5] K.W.D. Ledingham, S.S. Abuazoum, T. McCanny, J.J. Melone, K. Spohr, et al. "Comparison of hard x-ray production from various targets in air using a short pulse kHz laser with photon production from a high power multifilament laser beam from the same targets in air". In: *arXiv preprint arXiv:1106.4152* (2011)
- [6] A.D. Debus, M. Bussmann, M. Siebold, A. Jochmann, U. Schramm, et al. "Traveling-wave Thomson scattering and optical undulators for high-yield EUV and X-ray sources". In: *Applied Physics B* 100.1 (2010), pp. 61–76
- [7] A.D. Debus, M. Bussmann, M. Siebold, A. Jochmann, U. Schramm, et al. "Erratum to: Traveling-wave Thomson scattering and optical undulators for high-yield EUV and X-ray sources". In: *Applied Physics B: Lasers and Optics* 101.1 (2010), pp. 483–483
- [8] K. Zeil, S.D. Kraft, A. Jochmann, F. Kroll, W. Jahr, et al. "Absolute response of Fuji imaging plate detectors to picosecond-electron bunches". In: *Review of Scientific Instruments* 81.1 (2010), p. 013307
- [9] A. Buck, K. Zeil, A. Popp, K. Schmid, A. Jochmann, et al. "Absolute charge calibration of scintillating screens for relativistic electron detection". In: *Review of Scientific Instruments* 81.3 (2010), p. 033301

- [10] S. Henin, Y. Petit, J. Kasparian, J.-P. Wolf, A. Jochmann, et al. "Saturation of the filament density of ultrashort intense laser pulses in air". In: *Applied Physics B* 100.1 (2010), pp. 77–84
- [11] E.W. Gaul, M. Martinez, J. Blakeney, A. Jochmann, M. Ringuette, et al. "Demonstration of a 1.1 petawatt laser based on a hybrid optical parametric chirped pulse amplification/mixed Nd: glass amplifier". In: *Applied optics* 49.9 (2010), pp. 1676–1681
- [12] A. Debus, S. Bock, M. Bussmann, T.E. Cowan, A. Jochmann, et al. "Linear and non-linear Thomson-scattering x-ray sources driven by conventionally and laser plasma accelerated electrons". In: *Proc. SPIE* (2009), pages
- [13] S. Kraft, A. Jochmann, C. Erler, A. Debus, M. Bussmann, et al. "Injected wake field acceleration with a 40 MeV electron linac". In: *APS Meeting Abstracts*. Vol. 1. 2009, p. 4001
- [14] T. Kudyakov, A. Jochmann, K. Zeil, S. Kraft, K.H. Finken, et al. "High energy electron crystal spectrometer". In: *Review of Scientific Instruments* 80.7 (2009), p. 076106
- [15] E. Gaul, M. Martinez, J. Blakeney, M. Ringuette, D. Hammond, et al. "Petawatt lasers based on hybrid, OPCPA-Nd: glass amplification". In: *Lasers and Electro-Optics 2009 and the European Quantum Electronics Conference. CLEO Europe-EQEC 2009. European Conference on*. IEEE. 2009, pp. 1–1
- [16] E.W. Gaul, M. Martinez, J. Blakeney, A. Jochmann, M. Ringuette, et al. "Demonstration of a 1.1 Petawatt Hybrid OPCPA-Nd: glass Laser". In: *Advanced Solid-State Photonics*. Optical Society of America. 2009, WD1
- [17] E.W. Gaul, M. Martinez, J. Blakeney, M. Ringuette, D. Hammond, et al. "Activation of a 1.1 Petawatt hybrid, OPCPA-Nd: glass laser". In: *International Quantum Electronics Conference*. Optical Society of America. 2009, JWB2
- [18] E.W. Gaul, M. Martinez, J. Blakeney, A. Jochmann, M. Ringuette, et al. "1.1 Petawatt Hybrid, OPCPA-Nd: glass Laser Demonstrated". In: *Frontiers in Optics*. Optical Society of America. 2008, FWX3
- [19] M. Siebold, M. Hornung, R. Boedefeld, S. Podleska, S. Klingebiel, et al. "Terawatt diode-pumped Yb:CaF₂ laser". In: *Optics letters* 33.23 (2008), pp. 2770–2772

ACKNOWLEDGMENT

I see graduation as a process, not an event. I am tempted to say, it was ultra-intense at times, even though, this process cannot be called ultra-short anymore. In return, I was given the chance to build something from scratch, shape it the way I prefer, and finally, give it a name. Of course, a successful project like this is the result of the efforts of many people and I'd like to thank everyone of them.

First of all, I would like to thank Prof. Roland Sauerbrey for the opportunity to be part of this exciting field. He created research opportunities that are unique on international standards and a great chance for his students. His high research standards are also a good challenge, one that I enjoyed very much. I'd like to highlight the great fun I had, brainstorming about possible experiments with the laser through the ELBE halls. His skills in back-of-the-envelope calculations are impressive and I never left these meetings without having learned a new spectral line of some element.

He also supported me in going to Texas, which turned out to be one of the best decisions so far. Somehow, I bumped into Todd Ditmire, Mikael Martinez, Erhard Gaul and their Petawatt group. From those guys I learned a lot about how to get big projects on track, which was key for PHOENIX in the beginning days. Especially Mikael taught me the thin line you have to walk in order to be tough with your vendors and keep them on the boat at the same time. Not to forget the uncounted rounds that we spent around the greens. Thank you for these moments, Mike.

The whole TPW "Can do"-attitude is something I haven't experienced anywhere else, where I have been so far and I hope I could conserve a tad of it. Thank y'all.

Because of Roland Sauerbrey I met Ken Ledingham, who not only showed me that a bump'n run is rather more effective than pretty, and also showed me similar things in other areas, too. Thanks to him, I kept focused on the target, and he was there when I needed a kick in the butt or a clap on the shoulder.

I am grateful to my adviser Prof. Ulrich Schramm for his support and advice during the experiment and for all those "half-way"-conversations. Thank you also for signing the uncounted contract-extensions through the years. Having this support was the necessary backbone that finally got us the PRL.

Prof. Thomas Cowan... where do I begin? First of all, I haven't met a person that is as crazy for physics as Tom. Fortunately it's the good crazy, the passionate and enthusiastic way. I learned a lot about statistics and beam physics and yes, I should have listened to him long time ago and written my own Monte-Carlo code. It's on top of the list, I promise. Tom is the most entertaining distraction one could imagine, and if he doesn't blow himself up with his Czech fireworks he will inspire students like no one else can for some more years.

Speaking of students, when I started, the group was just established and there were only three more grad students, Alex, Karl and Thomas. Shortly after, Josefine and Markus joined the gang, and this team not only worked in the same group but became good friends. You guys were there fixing the laser, running my car in a speed-trap, helping me move a couple times. Our ski-trips, the "PhD"-expeditions and everything that involved Alex in the kitchen belong to my best memories in the recent years.

Thank you Alex, not only for sharing your wisdom when it comes to deli food, but also when it came to the magic of numerical computing, mathematica or all the other things you do with ease. Sorry for bugging you so often, and thank you for always listening to it anyway.

I haven't addressed the most important ones yet. Without them, this thesis would have been impossible, Arie and Jurjen. The spirit within "Team Electron" and the never fading drive towards first light of PHOENIX were amazing and I am honored having been a part of it.

Not a single experiment would be conducted without the technical support from the workshop, engineers (especially Manfred Sobiella and Simon Banowski), the IT department or our administration such as Petra Neumann and Katrin Thiele. My special thanks go to you.

I'd like to express my greatest respect to the teams that operate the DRACO laser as well as the ELBE accelerator. I know how complicated these machines are and still you make it look easy.

I want to thank my parents for their encouragement at all times, for providing logistical and organizational help and in general their backup in this and so many other endeavors before.

Finally I'd like to thank Almut Reichelt for putting up with me and her unconditional support and love.

Thank you!

PS. Thanks to my proof-readers Jeff and Bill as well as Pat for teaching me to keep my head up steady.

EIDESSTATTLICHE ERKLÄRUNG

Hiermit versichere ich, Axel Jochmann, geboren am 11.08.1981 in Reichenbach, im Rahmen meines Promotionsverfahrens an der Fakultät Mathematik und Naturwissenschaften der Technischen Universität Dresden und an Eides statt, dass

1. ich die vorliegende Arbeit ohne unzulässige Hilfe Dritter und ohne Benutzung anderer als der angegebenen Hilfsmittel angefertigt habe; die aus fremden Quellen direkt oder indirekt übernommenen Gedanken sind als solche kenntlich gemacht. Die Arbeit wurde bisher weder im Inland noch im Ausland in gleicher oder ähnlicher Form einer anderen Prüfungsbehörde vorgelegt.
2. ich die vorliegende Arbeit am Helmholtz-Zentrum Dresden-Rossendorf am Institut für Strahlenphysik unter der wissenschaftlichen Betreuung von Prof. Roland Sauerbrey angefertigt habe.
3. mir die geltende Promotionsordnung (Stand 23.02.2011, Fakultät Mathematik und Naturwissenschaften der TU Dresden) bekannt ist und ich diese anerkenne.

Dresden, 24.06.2014